Spring 2020

Hydrokinetic turbine composite blades and sandwich structures: Damage evaluation and numerical simulation

Mokhtar Fal

Department: Mechanical and Aerospace Engineering

HYDROKINETIC TURBINE COMPOSITE BLADES AND SANDWICH STRUCTURES: DAMAGE EVALUATION AND NUMERICAL SIMULATION

by

MOKHTAR FAL

A DISSERTATION

Presented to the Faculty of the Graduate School of the

MISSOURI UNIVERSITY OF SCIENCE AND TECHNOLOGY

In Partial Fulfillment of the Requirements for the Degree

DOCTOR OF PHILOSOPHY

in

MECHANICAL ENGINEERING

2020

Approved by:

K. Chandrashekhara, Advisor
Anthony Okafor
Cheng Wang
Kelly Homan
Jonathan W. Kimball

PUBLICATION DISSERTATION OPTION

This dissertation has been prepared in the form of three papers for publication as follows:

Paper I: Pages 8-43 have been submitted to the Journal of Ocean Engineering.

Paper II: Pages 44-75 have been submitted to the Journal of Renewable and Sustainable Energy.

Paper III: Pages 76-99 are intended for submission to the Journal of Sandwich Structures.

ABSTRACT

Composite materials are gaining interest due to their high strength to weight ratio. This study deals with both experimental and numerical approaches to cover the aspects of the failure of composite materials in hydrokinetic turbine applications. In Part I, the location and magnitude of failure in the horizontal axis water turbine carbon fiber-reinforced polymer (CFRP) composite blades with different laminate stacking sequences were investigated. Two lay-up orientations were adopted for this work ($[0^o]_4$ and $[0^o/90^o]_{2S}$). A finite element analysis model was generated to examine the stresses along the blade. Five angles were introduced to study the effect of pitch angle on the CFRP blades. The numerical results showed very good agreement with the experimental results. In Part II, an experimental setup was developed to test the delamination progression in CFRP blades under hydrodynamic loads in a water tunnel. Thermography analysis was employed to scrutinize the propagation of delamination. In addition, a computational fluid dynamics and one-way fluid-structure interaction were developed to predict the stresses along the blade. The unidirectional ($[0^o]_4$) blades showed the best performance while the cross-ply blades ($[0^o/90^o]_{2S}$) are prone to delamination. In Part III, the effect of increasing the contact area between the core and facesheet was studied. Two tests (impact and flat-wise tension) were carried out to examine the integrity of the structure. A finite element model was developed to study the damage due to localized load, such as impact load. The results obtained from both the tests (impact and flatwise tension) showed that increasing surface area had improved the structural integrity in regards to damage resistance due to impact, and delamination resistance between the facesheet and the core due to tension.

ACKNOWLEDGMENTS

I want to express my heartfelt gratitude to my advisor, Dr. K. Chandrashekhara, for his valuable guidance, assistance, and encouragement during my graduate study at Missouri University of Science and Technology. I thank him for his generous support and for providing an excellent working environment and teamwork. It has been a great pleasure and honor working with him.

I also want to express my genuine appreciation to my advisory committee members, Dr. Anthony Okafor, Dr. Kelly Homan, Dr. Jonathan W. Kimball, and Dr. Cheng Wang, for their valuable time and advice in the review of this dissertation.

I also wish to thank my fellow colleagues—Dr. A. Abutunis, Dr. R. Hussein, Dr. G. Dhaliwal, and Mr. O. Fashanu—for their assistance during this research. My gratitude is extended to my other fellow members in the research group for their help and advice.

I cannot forget to thank my parents, my siblings, especially my brother —Mr. Fadel—, my kids—Ms. Reem, Ms. Hoda, Ms. Fatima, and Mr. Anas— for their love, company, understanding, and encouragement.

Finally, I wish to express my deepest and most genuine gratitude to my lovely wife— Selma Ahmed— for her unconditional support. Without her, I would not be able to accomplish and fulfill my goals.

TABLE OF CONTENTS

Page

LIST OF ILLUSTRATIONS

SECTION Page

PAPER II

LIST OF TABLES

SECTION

1. INTRODUCTION

1.1. BACKGROUND ON COMPOSITE MATERIALS

Composite materials can be defined as a combination of two or more materials joined together to form a new material. Typically, the produced material has different characteristics and, commonly, better properties than the original constituent materials individually. In composite materials, the stronger constituent is commonly referred to as reinforcement, whereas the weaker constituent is normally referred to as the matrix. The reinforced material is providing the strength to the structure. The matrix is maintaining the orientation and position of the reinforced part. By holding the reinforcement in place, the matrix is forming the shape of the structure. Figure 1.1 gives a glance at some layup orientations. The orientation is commonly referred to as the laminate stacking sequence.

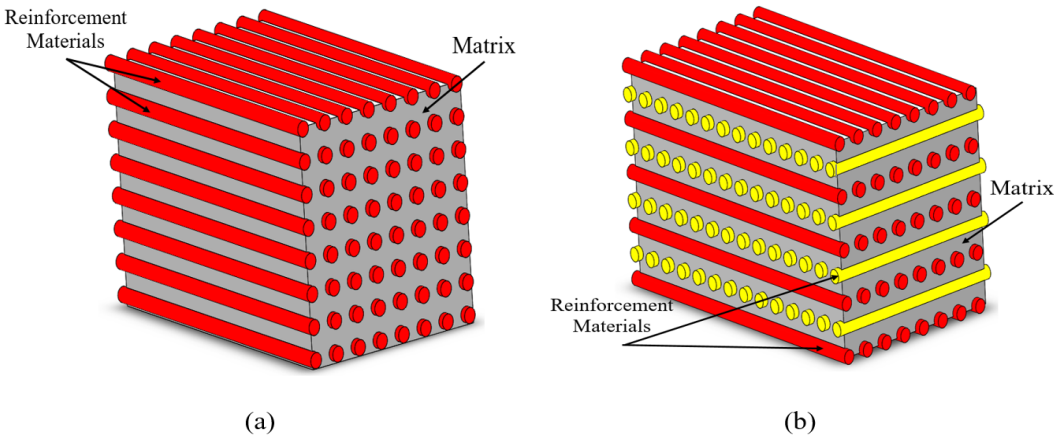

Figure 1.1 Examples of laminate stacking sequences where (a) unidirectional laminate and (b) cross-ply laminate

The concept of using fiber-reinforcement is as old as ancient Egypt [1]. The shield of Achilles is an example of a composite laminate structure. However, the use of resin as a reinforcement member was introduced in the last century.

Nowadays, composite materials can be found in almost every application. Some applications use composites more than others. For instance, in commercial aircraft, Airbus had a head start by using composite materials in the A300/A310 airplanes in 1983 [2, 3].

1.2. CLASSIFICATION OF COMPOSITE MATERIALS

Composite materials can be classified based on matrix or reinforcement type. There are three types of matrices: (a) polymer-matrix composites, (b) ceramic-matrix composites, and (c) metal-matrix composites. Polymer-matrix composites are classified into two groups: (a) thermoplastic polymer composites and (b) thermoset polymer composites. The primary difference between the two groups is that thermoplastic polymer composites can be recycled by going under heat to be melted down to become liquid and then reshaped. Thermosets, on the other hand, will always remain in a solid-state. Composite materials can be classified based on reinforcement. There are three main types of reinforcement: (a) fiber-reinforced composites, (b) particulate composites, and (c) structural composites. The latter is divided into two groups: (a) sandwich composite structures and (b) laminated composite structures.

1.3. HYDROKINETIC TURBINES

Hydrokinetic energy is gaining more popularity due to its advantages over other renewable resources. For instance, hydrokinetic turbines can operate at zero hydraulic head, which eliminates the necessity of building infrastructures to elevate water. Another advantage of the hydrokinetic energy is the power generated by a hydrokinetic turbine may

reach four times as much power per the swept area as that of a similar size wind turbine [4]. Turbines can be classified based on their axis of rotation relative to the flow direction. Vertical axis turbines, for example, have their axis perpendicular to the flow streamlines. Whereas, horizontal axis turbines are operating in the same direction as the flow. Turbines can also be classified based on the medium they work in. Accordingly, there are two types of turbines: (a) wind turbines and (b) water turbines. Both classifications mentioned earlier can be linked together to give a more specific classification of the turbines. In this study, all turbines were horizontal axis water turbines (HAWT). The number of blades is a very important detail to be mentioned as it plays a very important role in determining the performance of the turbine.

Hydrokinetic turbines generate energy by converting the kinetic energy from the rivers, tides, streams, into mechanical energy in the form of rotations. Then, generators can be used to convert mechanical energy into electrical power. In fact, this working principle is similar for both wind and water turbines.

1.4. COMPOSITE HYDROKINETIC TURBINE BLADES

For hydrokinetic turbines, composite materials are still in the early phase as the majority of the turbines are made of metals. This shortage of composite material in this field can be attributed to the lack of comprehensive knowledge of the behavior of composite turbine blades under different hydrodynamic loads. However, with every published study, more knowledge is gained, and more adaptation of composite materials can be noticed due to the increased confidence. The factors that affect the performance of HAWT are numerous. For instance, the number of blades, solidity, angle of attack, pitch angle, blockage, and flow characteristics are considered essential in determining the

performance of the HAWT. In addition, there are factors that affect the performance of composite materials such as laminate stacking sequence, reinforcement material, manufacturing process, kind of load, and the number of layers. Thus, when implementing composite material in water turbines, all these factors should be taken into consideration to be able to predict the behavior of the composite turbine blades.

1.5. SANDWICH STRUCTURES

Composite structures have been extensively employed in diverse applications such as housing, automobile, and aerospace. This was due to their high strength-to-weight ratio and design flexibility. Sandwich structures can save materials by decreasing the amount used to manufacture any structure. Composite materials are relatively expensive. Therefore, composite laminates and sandwich structures are making a perfect combination where composite materials can be used to the minimum. One of the most common sandwich structures configurations is the structure with a honeycomb core. Two thin layers of composite materials can be attached to a honeycomb core using two adhesive layers at each face to create a composite honeycomb sandwich structure. Figure 1.2 illustrates a schematic of a honeycomb sandwich structure. This specific configuration is very popular and used in aerospace structures because they exhibit better resistance to bending and out-of-plane loading compared to traditional composite laminates.

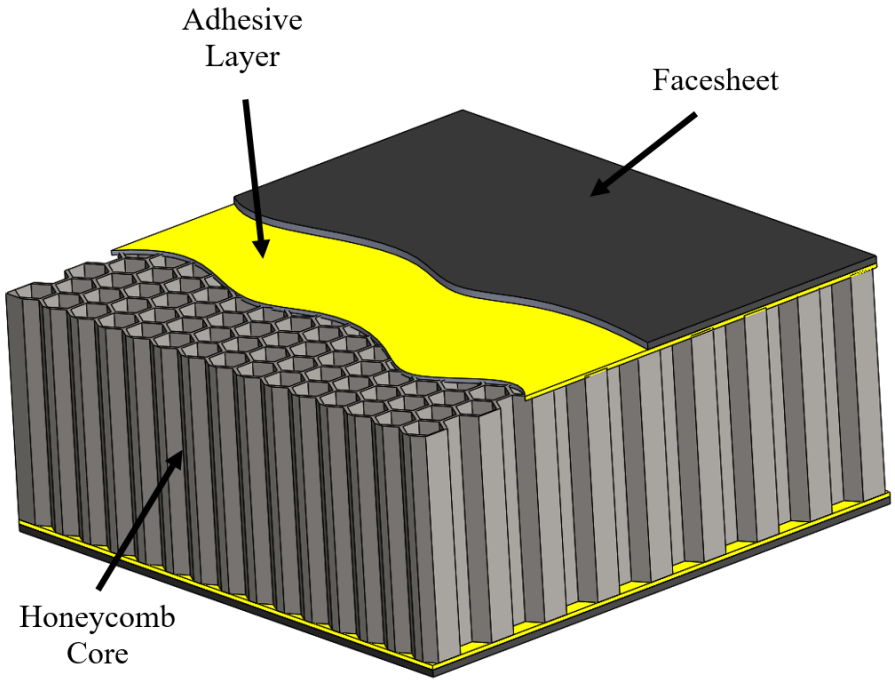

Figure 1.2 Schematic illustration of a honeycomb sandwich structure

2. SCOPE AND OBJECTIVES

This dissertation is comprised of three papers. The first paper is titled "Experimental and Numerical Failure Analysis of Horizontal Axis Water Turbine Carbon Fiber-Reinforced Composite Blade." In this paper, Carbon fiber-reinforced composite blades were manufactured using out-of-autoclave (OOA). Two laminate stacking sequences were adopted in this study. The first fiber layup orientation was unidirectional laminate ($[0^o]_4$), and the second orientation was cross-ply laminate ($[0^o/90^o]_S$). The purpose of this study was to study the behavior of both layup orientations under mechanical and hydrodynamic loads. All samples were tested to failure using a flexural bending test. In addition, a finite element model was created to study the fibers and matrix failure under each load. For the hydrodynamic loads, a modified blade element momentum theory model and an XFoil-MATLAB model were developed to accurately predict the lift coefficient and the drag coefficient along the span of the blade.

The second paper is titled "Investigation of Laminate Debonding in Horizontal Axis Water Turbine Composite Blades." In this study, a carbon fiber-reinforced polymer three-blade HAWT was manufactured. Each blade had a different laminate stacking sequence. The first blade was built using unidirectional laminate ($[0^o]_4$). The second blade was manufactured using a cross-ply laminate stacking sequence ($[0^o/90^o]_S$). The third blade was built using angle-ply layup orientation ($[+45^o/-45^o]_S$). During the manufacturing phase, a separation between the plies was created in two locations along the blade in order to study the delamination growth for each laminate stacking sequence. All blades were attached to one hub to create a three-blade rotor. The rotor was placed in a water tunnel to simulate the flow of a river. The three-blade horizontal axis water turbine was tested for three million

revolutions while operating at the optimum operational characteristics. Additionally, a one-way fluid-structure interaction model was created to calculate the hydrodynamic loads on the turbine blades. The thermography analysis approach was used to measure the interlaminar debonding inside the blades.

The third paper is titled “Evaluating Properties of Increased Contact Area of Additively Manufactured Core for Sandwich Composites.” In this paper, an additively manufactured core was sandwiched between two CFRP facesheets. The core was manufactured with two different honeycomb configurations. The first configuration had a larger area at the two faces of the core. The second configuration had no modifications on either face of the core. The weight of both configurations was maintained constant by decreasing the thickness of the walls in the modified honeycomb core. The objective was to study the effect of increasing the contact area between the facesheet and the core on the mechanical performance of the sandwich structure. To that end, two ASTM standard tests were carried out: (a) ASTM D7766 for the impact test and (b) ASTM C297 for the flatwise tension test. The second objective of this study was to develop a finite element model that can predict the behavior of this kind of sandwich structures under impact loads. All the objectives of this study have been achieved, and the finite element model showed a remarkable agreement with the experimental results.

PAPER

I. EXPERIMENTAL AND NUMERICAL FAILURE ANALYSIS OF HORIZONTAL AXIS WATER TURBINE CARBON FIBER-REINFORCED COMPOSITE BLADE

Mokhtar Fal, Abdulaziz Abutunis, Rafid Hussein, and K. Chandrashekhara

Department of Mechanical and Aerospace Engineering

Missouri University of Science and Technology, Rolla, MO 65409, USA

ABSTRACT

High-performance composites are used in many applications due to their design flexibility, corrosion resistance, high strength-to-weight ratio, and many other excellent mechanical properties. In this study, the location of failure initiation and magnitude in horizontal axis water turbine carbon fiber reinforced polymer (CFRP) blades with different lay-up orientations were investigated. Unidirectional [0o]4 and cross-ply [0o/90o]S layups were selected to study the effect of the buildup direction on the failure of the composite water turbine blade. A finite element analysis (FEA) model was generated to examine the stresses along the blade for both mechanical and hydrodynamic loads. Flexural destructive tests were conducted to validate the results obtained from the numerical simulations. In addition, a blade element momentum theory model was created to calculate the hydrodynamic forces acting along the span to determine the maximum loading radial location, which was used for the fixture design and FEA simulation input. Both unidirectional and cross-ply composite blades were tested for failure. There was a general agreement between the experiments and the simulations, which validated the results. Moreover, FEA simulations were performed to apply the load to the samples with different

pitch angles (-10o, -5o, 0o, 5o, 10o). At a 0o pitch angle, the unidirectional CFRP composite blades showed higher strength compared to the cross-ply blades. However, when the load was applied with any pitch angle other than 0o, a significant drop in strength was noticed for the unidirectional blades while the cross-ply blades were less responsive to the change in the pitch angle.

1. INTRODUCTION

As non-renewable resources are damaging the environment, the economy, and causing harmful impact on human health as well as animals, the world will depend, eventually, on renewable energy to be the primary source of power [1]. There are many sources of renewable energy such as solar, wind, hydropower, and geothermal energy. The energy generated by water turbines through converting kinetic and potential energy into mechanical work is called hydropower energy [2]. Hydropower is one of the most promising renewable energies available. It can be harnessed from waves, tides, rivers, streams, and the open ocean. Due to the many similar operational principles between water and wind turbine technologies, a large amount of knowledge can be transferred from wind applications to water applications and vice-versa. However, there are a few substantial differences between the two technologies. These differences are important to consider when selecting material, designing the blades, and selecting the application.

Worldwide, hydropower energy contributes to 20% of the total generated power and in some countries, it is the exclusive resource to generate power [3]. In the United States alone, hydropower energy generation represents about 75% of the total renewable energy harvesting and this hydropower generation is expected to go up to 23,000 MW by

2025 [4]. In the process of hydropower generation, the most vital part is the turbine, more specifically, the blades [5]. This is due to their high tendency to fail under high loads fatigue [6]. Therefore, it is extremely important to engineer a reliable blade that will lead to the maximum energy extraction and longer life expectancy for the specific application it served. Many factors play substantial roles in controlling the performance of the water/wind turbine [6, 7]. This work focuses on studying the performance of a CFRP composite blade that works in horizontal axis water turbine applications.

There are some differences between water and wind turbines. For instance, the velocity of the water is relatively slow, compared to wind velocity. However, the harnessed energy per square unit of rotor swept area from HAWTs is higher than that from wind turbines [8]. In some cases, the power generated by a HAWT may reach four times the power generated by a similarly rated wind turbine [9]. This is because water is approximately 800 times denser than the air, which results in higher kinetic energy conversion per unit area. One essential factor that plays a major role in the performance of any turbine is material selection. Different materials with different properties will affect the rendering of the turbine significantly. Unlike wind energy, generating hydropower energy can only be achieved by submerging the turbine into water. This leads to known issues such as erosion, corrosion, fatigue, and water absorption. Due to its predominant mechanical properties, composite materials can overcome most of the common issues that occur when using other traditional materials. For instance, composite materials are known for their corrosion resistance, durability, design flexibility, chemical resistance, lighter weight, rigidity, high flexural modulus, low petrochemical ingredients, and exceptional electrical insulation [10]. These properties and many others make composite materials the

best option for water turbine blades. Water turbine blades operate in rivers and marine currents which result in an extremely harsh operational environment [11]. The thrust, tangential, and torsional loadings caused by the high kinetic energy flux are tremendous. Consequently, the intense bending moment at the root and large amount of deflection at the tip are serious design constraints [12]. A reliable turbine blade design will increase the cost-effectiveness of the turbine system. Creating this design requires a comprehensive understanding of the different loading behaviors of the blade and its structural response. The most commonly used composite materials are the glass- and carbon fiber reinforced polymer. In general, composite blades are superior to their traditional counterparts [13]. In this study, CFRP is used as the primary material to manufacture the composite blades. The failure location and magnitude of the composite blades with different lay-up orientations and different pitch angle were investigated.

2. BLADE DESIGN AND MANUFACTURING

2.1. BLADE PROFILE SELECTION

The first step to design and fabricate any turbine blade is the airfoil/hydrofoil selection. The blade hydrofoil (profile) is one of the most important factors because it plays a significant role in controlling lift-drag ratio [14, 15]. Many blade profiles are available to choose from, but only a few can serve the purpose of this work. As the current research concerns mainly about the effect of both laminate stacking sequence and the angle of which the load is applied as well as the interaction between them, untwisted blade profiles with high lift-drag ratio will give a direct indication of the relevance of these two factors to the performance of the hydrokinetic water turbine. Adding more factors to the process of the

blade profile selection will increase the uncertainty of the results. Therefore, after a long investigation, while taking into consideration the static and dynamic loads, Eppler 395 was selected to be the blade profile for this study. This blade profile provides a high ratio of lift to drag (C_L/C_D) as shown in Figure 1. This figure was generated in MATLAB using XFoil [16], for a range of operational Reynolds numbers (Re).

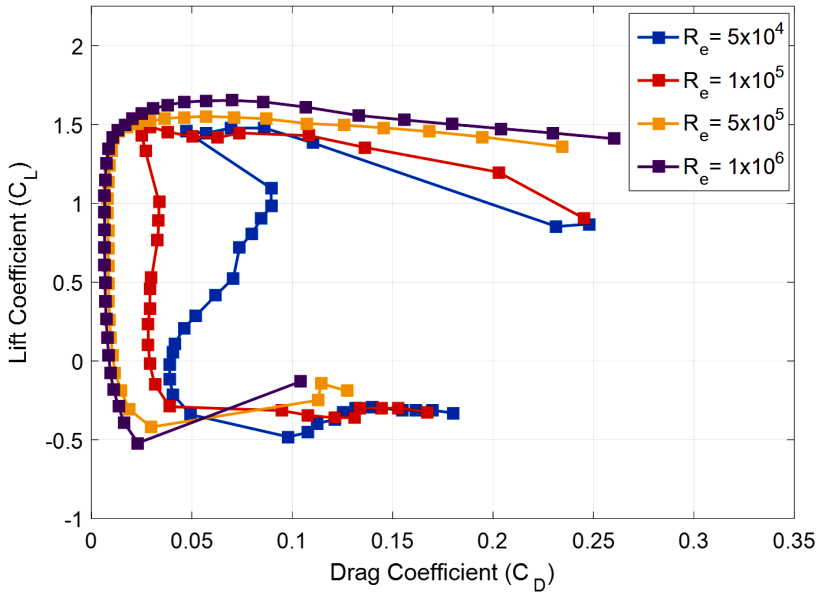

Figure 1. Lift coefficient vs. drag coefficient for Eppler 395 airfoil at different Reynolds numbers

2.2. MATERIALS AND PLY ORIENTATION

Being submerged into water, hydrokinetic turbines, unlike wind turbines, will face more challenges such as rapid corrosion and biofouling. In addition, the hydrodynamic load oscillates based on the velocity of the water. This creates hard working environments that can cause failure due to fatigue. Turbine blades that are made of composite materials are known for their high strength to weight ratio. The high modulus of elasticity makes

them an excellent candidate for this study. IM7/Cycom 5320-1 carbon/epoxy prepreg was selected as the core material of the turbine blade. Two laminate stacking sequences of [0º/90º/90º/0º] and [0º/0º/0º/0º] were chosen to study the effect of the layup orientation on the blade performance

2.3. MOLD FABRICATION

Ultem 9085 molds were manufactured using fused deposition modeling (FDM) process in Fortus 400mc machine (Stratasys, USA) at Missouri University of Science and Technology. The FDM process has three stages: (1) Pre-processing stage where a three-dimensional CAD models were created. The model was then exported to the Fortus 400mc machine as a Stereo Lithography (STL). (2) Manufacturing stage where Stratasys machine started to fabricate the FDM parts using Ultem 9085 filament. (3) Post-processing stage where all the support materials were detached from the FDM parts. The upper and lower halves of the mold are shown in Figure 2.

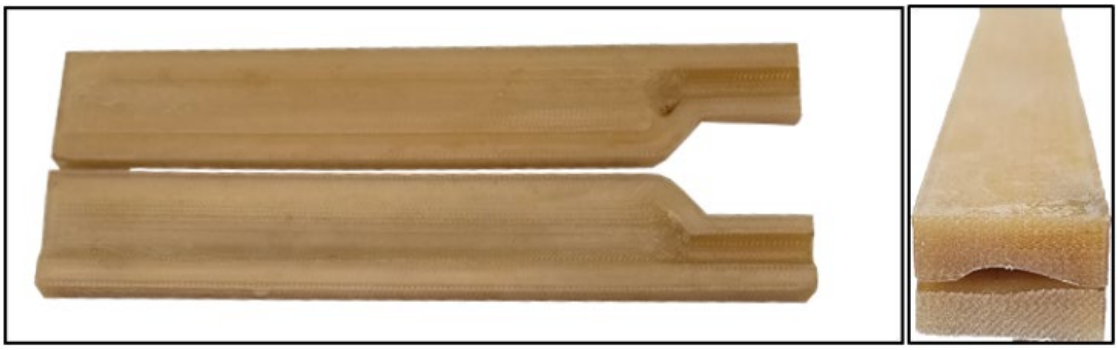

Figure 2. The additively manufactured molds of the hydrofoil Eppler 395 using ULTEM 9085

After the molds were removed from the additive manufacturing machine, they went through a polishing process to make the surface as smooth as possible while maintaining

the Eppler 395 hydrofoil shape and size to eliminate additional factors that might affect the results. The polishing process was completed after reaching an ISO surface roughness grade of N10, which is equivalent to about 12.5μm.

2.4. BLADE MANUFACTURING PROCESS

The composite blades were built using an OOA technique. Due to its high C_L/C_D ratio, an Eppler 395 hydrofoil was selected to be the primary profile for this study. The process of making the composite blades starts with placing the two halves of the mold on an aluminum plate. Then, four layers of carbon/epoxy prepreg were placed over each mold. As described previously, two laminate stacking sequences were utilized to further study the outcome from having different layup orientation on the general performance of the CFRP composite blades. To stack the plies in the desired orientation, the unidirectional layup blades were obtained by placing all four plies in the same direction (along the span). Whereas, the cross-ply blades were made by starting with placing a 0^o ply then two 90^o plies before finishing with a 0^o ply. Next, a Teflon sheet was placed between the molds and the fiber to prevent the composite from sticking to the mold during the curing. After that, a breather was placed over the blades to allow air to be removed to achieve the desired vacuum while retaining an appropriate matching between the molds and the composite layers as shown in Figure 3. After sealing the aluminum plate with a transparent vacuum bag, all the trapped air was removed by applying a vacuum of 760 mm of Hg. The whole setup was then placed inside an oven for 8 hours. The IM7/Cycom 5320-1 carbon/epoxy prepreg manufacturer recommended curing, and post-curing cycles were followed. Next, the molds were separated from the composite blades. The two cured composite blade halves were mated and adhered together using a high impact resistant, water resistant, and

shrink free epoxy. Finally, the blade's span length was cut down to 140 mm. The edges of the blades were trimmed and sanded down to the foil chord width of 16.76 mm.

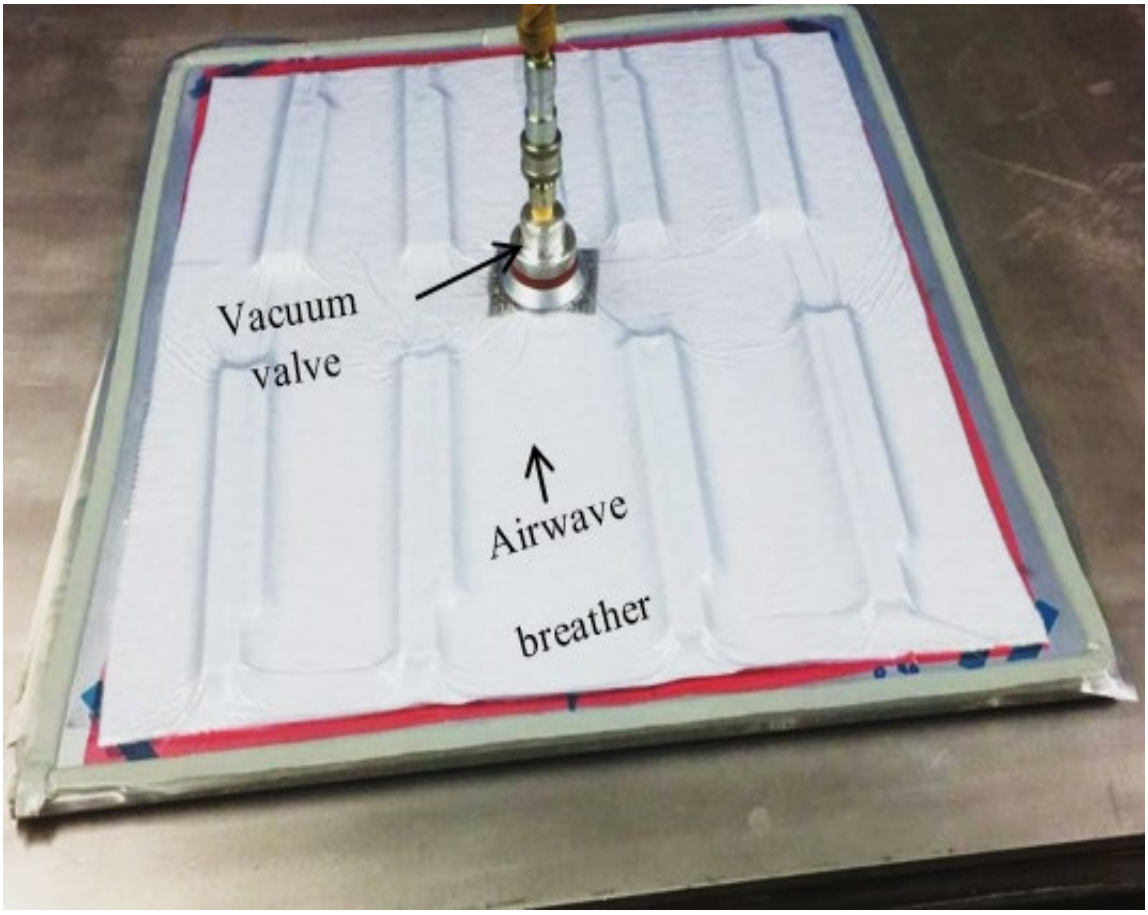

Figure 3. The blade manufacturing setup under vacuum

3. EXPERIMENTAL METHODOLOGY

The layup orientation can significantly control the strength of the composite materials. Many studies have shown the relationship between the applied load, the layup orientation, and the stress distribution [17-20]. However, due to the unique shape of

hydropower turbine blades, it is very important to further study the resultant stress due to the bending of the blade. In this case, the blades were manufactured with two different laminate stacking sequences and were tested for bending strength. The testing process is discussed in this section.

3.1. EXPERIMENTAL SETUP

An Instron 5985 Universal Testing System machine was used to carry out the flexural tests. In order to hold the blades firmly in the appropriate position while the load was applied, a special fixture was designed and manufactured. In the experiments, the load was applied to the samples with 0^o degree pitch angle; while in simulation part, the effect of introducing the pitch angle was comprehensively investigated. The pitch angle is defined as the angle between the foil chord line and the load pin axis. The strain rate was selected to be 25.4 mm/min. Due to the shape of the hydrofoil, the leading edge will touch the loading cell before the trailing edge even with 0^o pitch angle. Even though the focus of the testing is on bending strength, the moment and shear forces must also be considered. The gap between the blade and the loading cell is shown in Figure 4.

3.2. DETERMINATION OF THE LOCATION FOR THE APPLIED LOAD

In order to determine the proper location to apply the load, a blade element momentum theory (BEMT) model was created. Section 4.2 explains, in detail, the procedure of generating the BEMT model. When the turbine was operated at optimum efficiency, the BEMT results revealed that the highest thrust force was located at about r/R=0.71, where R is the rotor radius and r is the radial distance from the rotor center.

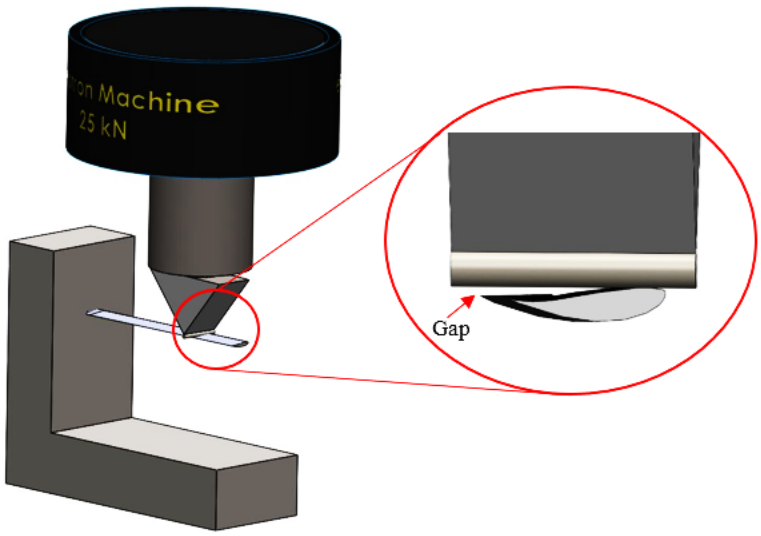

Figure 4. A gap between the trailing edge of the composite blade and the loading cell

The BEMT results are shown in Figure 5. Therefore, the point of contact between the blade and the load cell was set to be at 71% of the blade span.

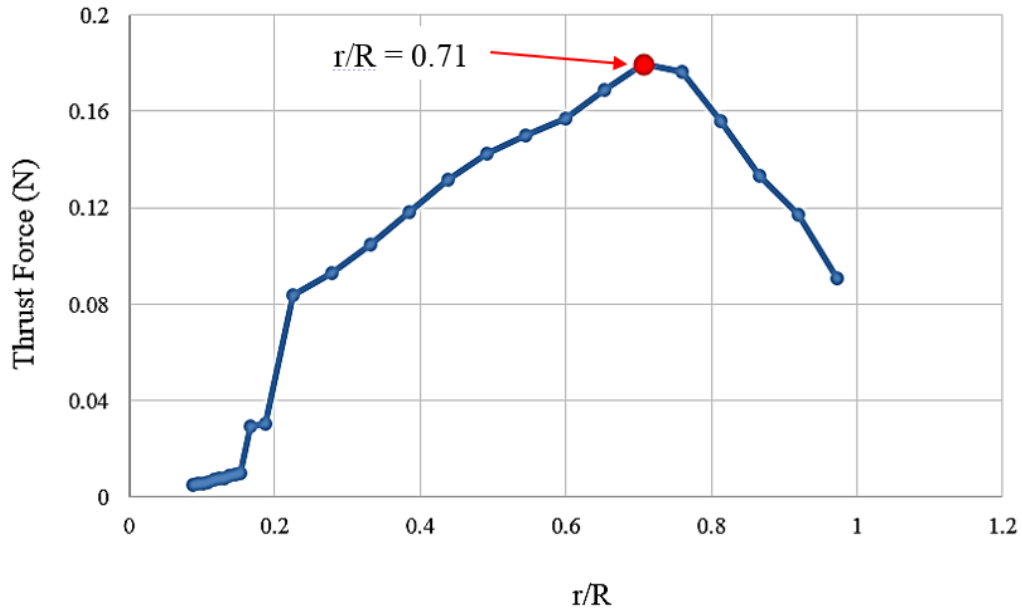

Figure 5. Thrust force vs. normalized radial distance at optimum operational conditions

3.3. BENDING TEST

The bending fixture holds the blade by placing the elongated root between the two clamps and uses bolts to tighten the root and prevent any movement. Next, a constant strain rate was applied by the means of the load cell. Figures 6a, 6b, and 6c show the intact root, the blade under the load, and the location of the failure, respectively. For this experiment, no pitch angle has been applied to the blades, i.e. all the blades were tested with 0^{o} pitch angle.

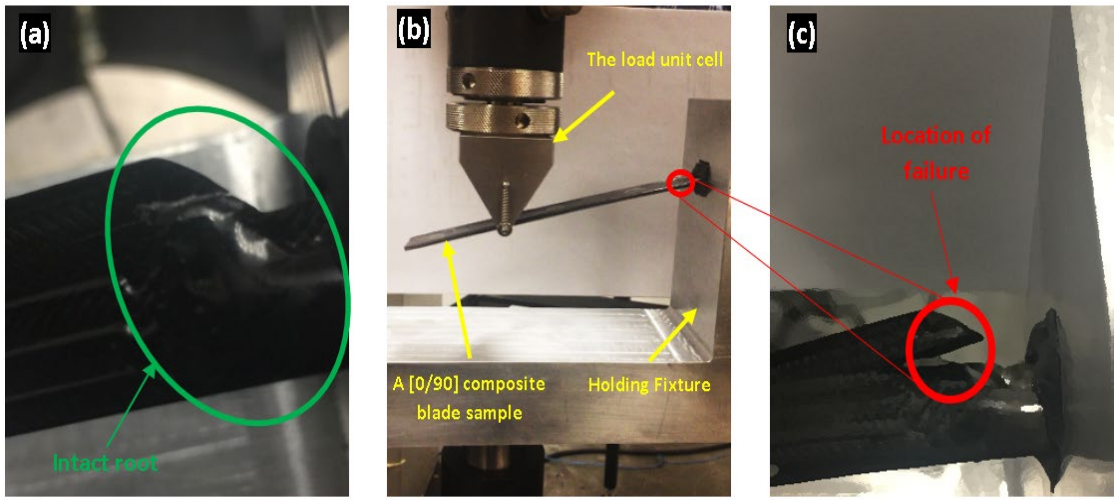

Figure 6. (a) The root of the blade pre applying the load, (b) the blade attached to the fixture and going under load, and (c) the location of the crack initiation at the blade root

4. NUMERICAL SIMULATION

4.1. FINITE ELEMENT ANALYSIS

The finite element method (FEM) is a numerical technique for finding approximate solutions. It is also referred to as finite element analysis (FEA). It is the process of solving partial differential equations to find approximate solutions to boundary value problems. In

this work, a finite element model was created for the CFRP composite blades. The blades were designed via a 3D CAD software. Then, the designed CAD model was exported the commercial FEA software of ABAQUS CAE. The goal from creating the FEA model was to investigate the stresses and the prospective failure modes under both hydrodynamic forces and flexural loads. The load cell on the Instron 5985 Universal Testing System machine was represented by a pin. The load pin was a cylindrical rigid part having an equal length to the blade's chord, which was used only for bending test simulation, as shown in Figure 7. The composite blade was discretized with 4-node shell elements (S4R) using two mesh sizes to check for the mesh sensitivity. The two meshes were generated using an approximate global size of 0.002 m and 0.001 m. The layup orientation was assigned to the top and bottom surfaces of the blade where the 0º orientation is in the span-wise direction and 90° orientation is in the chord-wise direction. The load pin was meshed with 3D elements (C3D8R) and constrained as a rigid body.

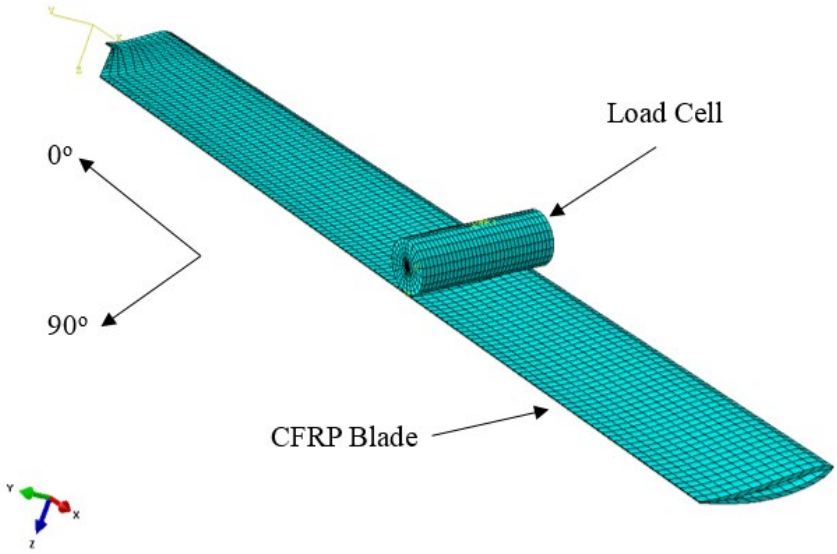

Figure 7. The mesh domain of the CFRP composite blade and the load cell

The boundary condition of the rigid pin was assigned a displacement of 80 mm in the y-direction. The step procedure was selected to be a static-general step. As for the root of the blade, a built-in boundary condition was assigned to it. The selected boundary condition is called “ENCASTRE” where U1=U2=U3=UR1=UR2=UR3= zero. The U1, U2, U3, UR1, UR2, and UR3 are the displacement on X-axis, displacement on Y-axis, displacement on Z-axis, moment in X-axis, moment in Y-axis, and moment in Z-axis, respectively. Damage initiation was modeled using Hashin’s criterion in ABAQUS CAE. The Hashin’s damage model is primarily intended for use with fiber-reinforced composite materials. In addition, it has the ability to consider four different failure modes: fiber tension, fiber compression, matrix tension, and matrix compression, which are governed by Equations 1, 2, 3, and 4, respectively [21, 22].

$$(\hat{\sigma}_{11} \geq 0)\text{: } F_f^t = \left(\frac{\hat{\sigma}_{11}}{X^T}\right)^2 + \beta\left(\frac{\hat{\tau}_{12}}{S^T}\right)^2 \tag{1}$$

$$(\hat{\sigma}_{11} < 0)\text{: } F_f^c = \left(\frac{\hat{\sigma}_{11}}{X^C}\right)^2 \tag{2}$$

$$(\hat{\sigma}_{22} \geq 0)\text{: } F_m^t = \left(\frac{\hat{\sigma}_{22}}{Y^T}\right)^2 + \left(\frac{\hat{\tau}_{12}}{S^L}\right)^2 \tag{3}$$

$$(\hat{\sigma}_{22} < 0)\text{: } F_m^c = \left(\frac{\hat{\sigma}_{22}}{2S^T}\right)^2 + \left[\left(\frac{Y^C}{2S^T}\right)^2 - 1\right]\frac{\hat{\sigma}_{22}}{Y^C} + \left(\frac{\hat{\tau}_{12}}{S^L}\right)^2 \tag{4}$$

where $\hat{\sigma}_{11}, \hat{\sigma}_{22}$, and $\hat{\tau}_{12}$ are the components of the effective stress tensor that is used to evaluate the initiation criteria. X^T, X^C, Y^T, Y^C, S^L, and S^T are longitudinal tensile strength, longitudinal compressive strength, transverse tensile strength, transverse compressive strength, longitudinal shear strength, and transverse shear strength, respectively. β is a

coefficient that determines the contribution of the shear stress to the fiber tensile initiation criterion.

The contact between the pin and the blade was assumed frictionless in the tangential behavior and rigid in the normal behavior. All cases were solved using the explicit solver with minimum and maximum time increments of 1×10^{-12} and 0.1 sec respectively. The elastic and strength properties are listed in Table 1 [23]. The transverse shear modulus (G_{23}) was assumed equal to the G_{13}.

Table 1. Material properties of the IM7/Cycom 5320-1 carbon/epoxy prepreg

Property	Symbol	Value
Longitudinal tensile modulus	E_{11}	$156x10^9$ Pa
Transverse tensile modulus	E_{22}	$9.3x10^9$ Pa
Longitudinal Poisson's ratio	ν_{12}	0.3
In-plane shear modulus	G_{12}	$5.5x10^9$ Pa
Transverse shear moduli	G_{13}, G_{23}	$5.5x10^9$ Pa
Longitudinal tensile strength	X_T	$2.503x10^9$ Pa
Longitudinal compressive strength	X_C	$2.078x10^9$ Pa
Transverse tensile strength	Y_T	$75.9x10^7$ Pa
Transverse Compressive strength	Y_C	$165x10^6$ Pa
Longitudinal shear strength	S_L	$73x10^6$ Pa
Transverse shear strength	S_T	$73x10^6$ Pa

For accurate assessment of the damage initiation in fiber-reinforced materials, additional information regarding the fracture energy constants is needed. Damage evolution fracture energy constants for IM7/Cycom 5320-1 carbon/epoxy prepreg laminate were taken from literature and they are shown in Table 2 [24]. In addition, the damage stabilization as viscosity coefficients for longitudinal tensile strength, longitudinal compressive strength, transverse tensile strength, and transverse compressive strength were assumed to be 1×10^{-4} to improve the accuracy of the calculations [25, 26].

Table 2. Damage evolution fracture energy constants of the IM7/Cycom 5320-1

Property	Symbol	Value
Longitudinal tensile fracture energy	F^{LT}	81.5×10^3 J/m^2
Longitudinal compressive fracture energy	F^{LC}	106.5×10^3 J/m^2
Transverse tensile fracture energy	F^{TT}	0.277×10^3 J/m^2
Transverse compressive fracture energy	F^{TC}	5.62×10^3 J/m^2

If the sample is fixed at a 0^o pitch angle with respect to the axial plane of the load cell (no rotation) as shown in Figure 4, the load cell will start touching the leading edge of the blade and push it down before touching the trailing edge. This action will cause a moment as well as shear on the CFRP composite blades.

4.2. BLADE ELEMENT MOMENTUM THEORY

The combination of blade element theory and momentum theory morph into the classical blade element momentum theory (BEMT) to solve for rotor plane flow properties.

BEMT balances the axial (linear) and angular momentums of an annular element of flow volume to hydrodynamic loads acting on a corresponding blade element (strip). The calculated hydrodynamic forces from BEMT at specific operational tip speed ratio (TSR) were considered for the structural analysis.

$$dT = 4\pi r\rho V^2 a(1-a)dr \tag{5}$$

$$dM = 4\pi r^3 \rho V \Omega (1-a)a' dr \tag{6}$$

where $\rho, V, \Omega, r,$ and dr are water density, upstream velocity, blade angular velocity, radial distance to the rotor center, and the span-wise width of the annular element, respectively. The variables a' and a are the tangential and axial induction factors, respectively. These induction factors account for the change in flow speed at the rotor plane and are the seeking solution of the BEMT.

The blade element theory, on the other hand, proposes dT and dM based on the calculated normal force coefficient (C_n) and tangential force coefficient (C_t) acting on a blade element.

$$dT = \sigma\pi r\rho \frac{V^2(1-a)^2}{sin^2\phi} C_n dr \tag{7}$$

$$dM = \sigma\pi r^3 \rho \frac{V\Omega(1-a)(1+a')}{sin\phi cos\phi} C_t dr. \tag{8}$$

σ is the sectional local solidity at radial distance r, which is given by $\sigma = \frac{Nc}{2\pi r}$, here, N is the number of blades, and c is the chord length of hydrofoil at this radial location.

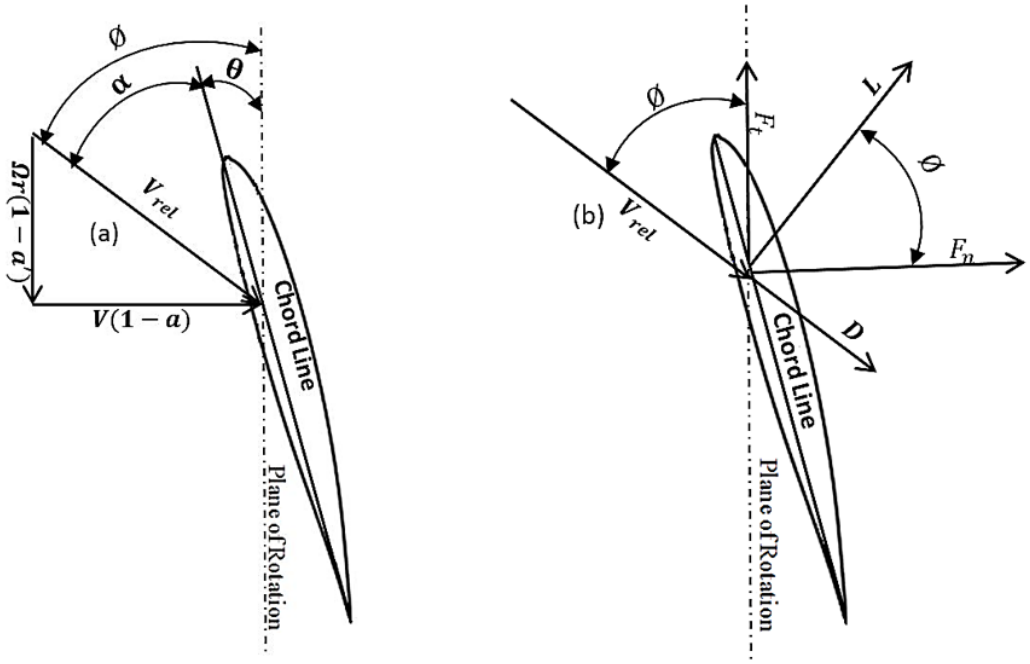

(a) (b)

Figure 8. Illustration of (a) velocity diagram and (b) force diagram at a blade section

The variable ϕ is the local inflow angle and calculated as $\phi = \arctan\frac{(1-a)V}{(1+a')\Omega.r}$. The normal and tangential force coefficients are obtained as follows:

$$C_n = \mathrm{C_L}\cos\phi + C_D \sin\phi \tag{9}$$

$$C_t = C_L\sin\phi - C_D \cos\phi \tag{10}$$

C_L and C_D are the lift and drag coefficients, respectively, and they are given by the following two equations $C_L = \frac{L}{\frac{1}{2}\rho V_{rel}^2 c_r}$ and $C_D = \frac{D}{\frac{1}{2}\rho V_{rel}^2 c_r}$, here, L and D are the lift and drag forces acting on the blade element.

The hydrodynamic foil characteristics (C_L and C_D) were originally generated at different operational condition, by the mean of a 2D panel code, XFoil. The XFoil can reasonably predict the pressure distribution and lift but underestimates the drag. Therefore, the drag coefficient was corrected during BEMT iteration. The rotational effect was accounted for through correcting the XFoil output lift by a model suggested by Du and Selig [27] and XFoil output drag by Eggers et al [28]. The corrected data was then saved to a look-up 3D data sheet which contained the lift and drag coefficients over a wide range of angles of attack ($-180\ ^o \leq \alpha \leq 180^o$). extrapolation of the lift and drag over this wide range of angles of attack was achieved by the use Viterna model [29]. In addition, it also enables the extrapolation of a wide range of operational R_e that is based on the local relative velocity V_{rel}, which varies radially. The look-up sheet can then be used by BEMT. Figure 9 and 10 show lift and drag coefficients at two different operational and geometrical conditions.

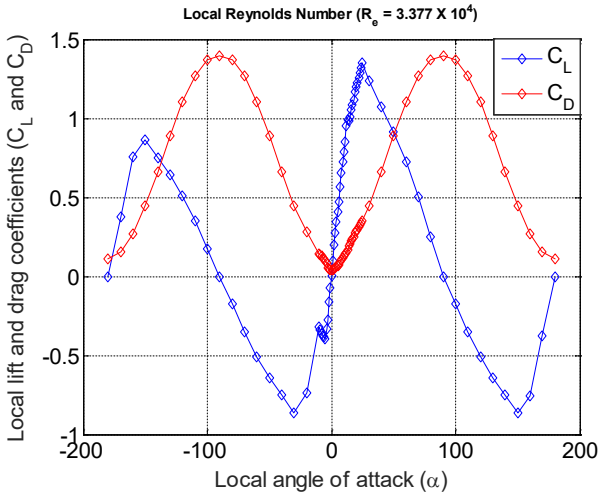

Figure 9. C_L and C_D at a rotational speed of 100 RPM, velocity of 0.979 m/s and r/R of 0.9565

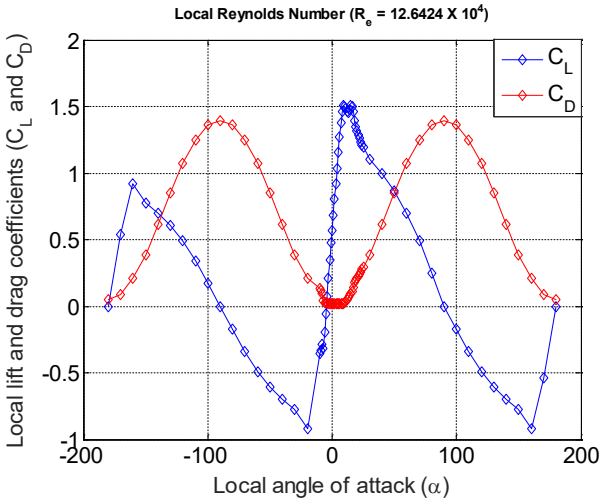

Figure 10. C_L and C_D at a rotational speed of 500 RPM, velocity of 0.8996 m/s and r/R of 0.177

Equating the thrust from Equations 5 and 7, the torque from Equations 6 and 8, incorporating the tip and hub losses correction, and solving for the axial induction factor (a) and the tangential induction factor (a') will yield:

$$a = \frac{1}{\frac{4Fsin^2\phi}{\sigma C_n} + 1} \tag{11}$$

$$a' = \frac{1}{\frac{4Fsin\phi\cos\phi}{\sigma C_t} - 1} \tag{12}$$

F is the total loss factor that results from the product of tip and hub loss factors. The tested rotor that was used for validation has a diameter of 12 in. (304.8 mm) which created a blockage ratio (ratio of rotor to tunnel cross section) of 0.3968 in the water tunnel. The relatively high blockage further accelerated the flow and increased the generated power and hydrodynamic loads on the rotor compared to the unconfined rotor. Therefore, further

correction for the axial induction factor was required to account for this confinement effect. A blockage correction method was integrated into the BEMT. After the convergence of the induction factors was achieved, the flow velocity components and flow angles were obtained. Finally, the sectional normal force F_n and tangential force F_t were calculated as:

$$F_n = \frac{1}{2}\rho V_{rel}^2 c C_n \tag{13}$$

$$F_t = \frac{1}{2}\rho V_{rel}^2 c C_t \tag{14}$$

After the hydrodynamic forces per unit length were obtained at several blade radial locations (r), forces were integrated over their corresponding blade elements with an assumption of a linear variation between neighboring sections. The results of the integrations then were considered as concentrated forces that act at the center of the elements.

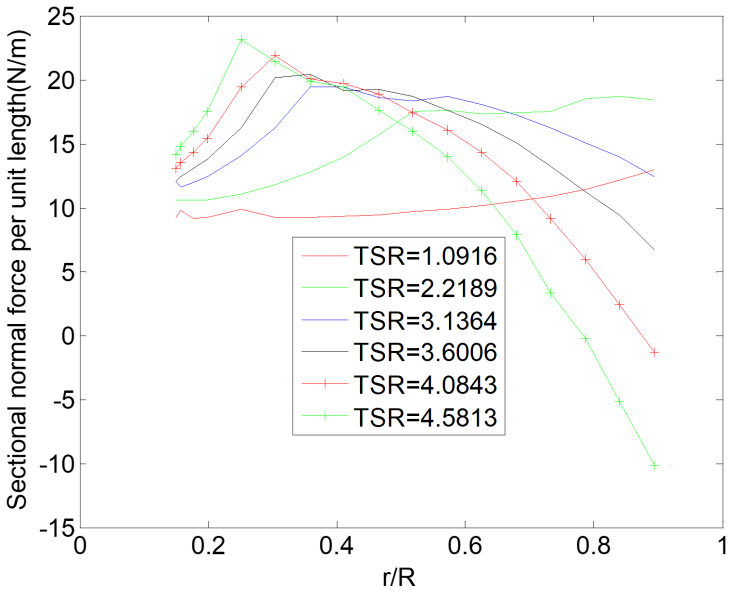

Figure 11. The normal force distribution along the blade of 3-blade rotor at different tip speed ratios

To examine the BEMT accuracy, the rotor torque was calculated by integrating the sectional moments over the blade span and then the power was obtained as

$$P = M \times \Omega \tag{15}$$

M is the applied torque magnitude $(N.m)$ and Ω is the rotational speed (rad/sec). The predicted power was validated against experimental measurement and presented in Figure 14 in Section 5.2.

5. RESULTS AND DISCUSSION

5.1. EXPERIMENTAL RESULTS

A total number of 10 blades were manufactured for each lay-up orientation using CFRP composites via the OOA process. All samples were then tested for failure and the results are shown in Table 3. It was noticed that the highest load was carried out by the unidirectional blades.

Table 3. The results summary of the bending tests for the unidirectional blades and the cross-ply blades

Sample #	Lay-up Direction	Load at Failure (N)	Avg. Load at Failure (N)
1		84.2689	
2		91.285	
3	$[0^o]_4$	89.7628	85.37 ± 2.001
4		81.8328	
5		79.70244	
6	$[0^o/90^o]_S$	45.6232	45.84 ± 0.456

Sample #	Lay-up Direction	Load at Failure (N)	Avg. Load at Failure (N)
7		47.1028	
8		46.9243	
9		45.0715	
10		44.49635	

The average load vs. strain curves for the lay-ups $[0^o]_4$ and $[0^o/90^o]_S$ are shown in Figure 12 and Figure 13, respectively. In addition to the previous observation, it was also observed that the unidirectional samples failed sooner than the cross-ply samples, which indicates that a relatively larger amount of yielding was achieved by the latter.

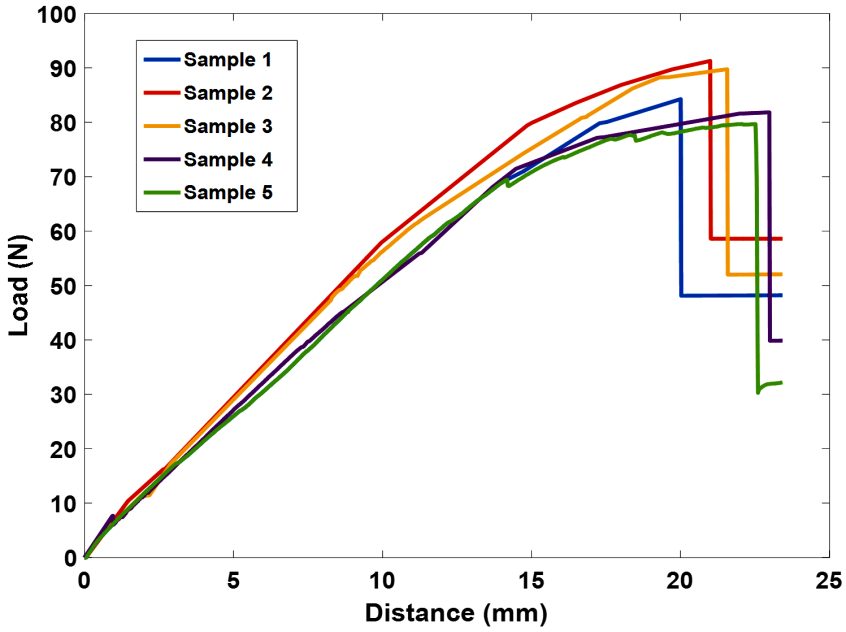

Figure 12. The load vs. displacement curve of the unidirectional blades ($[0^o]_4$)

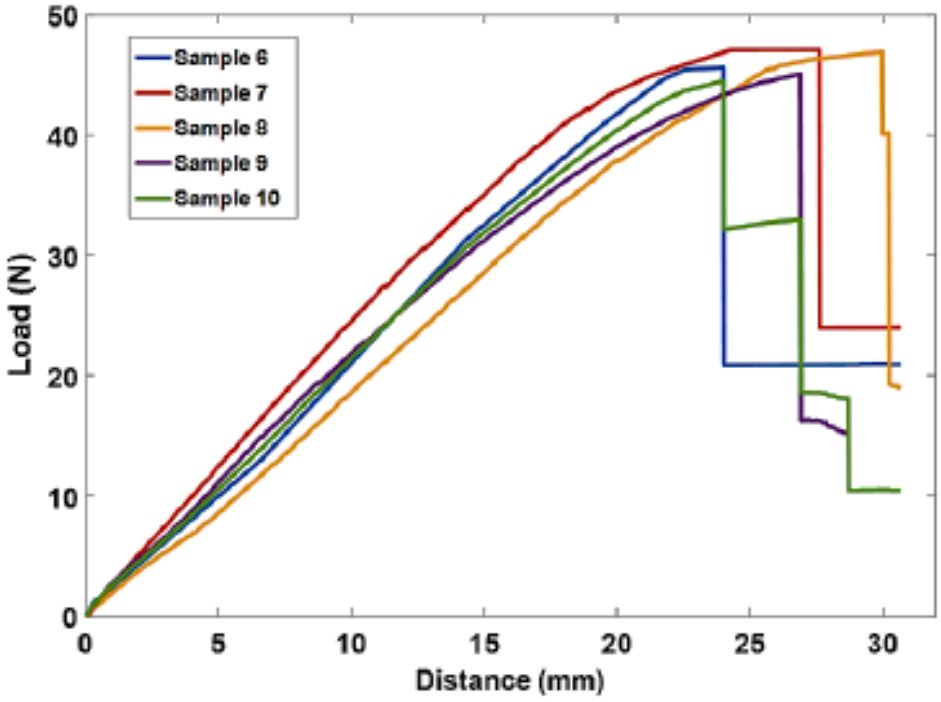

Figure 13. The load vs. displacement curve of the cross-ply blades ($[0^o/90^o]_S$)

5.2. BEMT VALIDATION

The power coefficient for the three- blade rotor against the TSR curves produced by the water tunnel test and BEMT is shown for validation in Figure 14. The results were reasonably consistent. As the rotational speed decreased, the thrust forces increased, leading to higher system friction losses, especially in the bevel gears even though the thrust bearings were mounted on the front and back ends of the horizontal shaft. The left side of the power curve was not completed due to the delay in the stall, which is a well-known phenomenon [27, 30, 31].

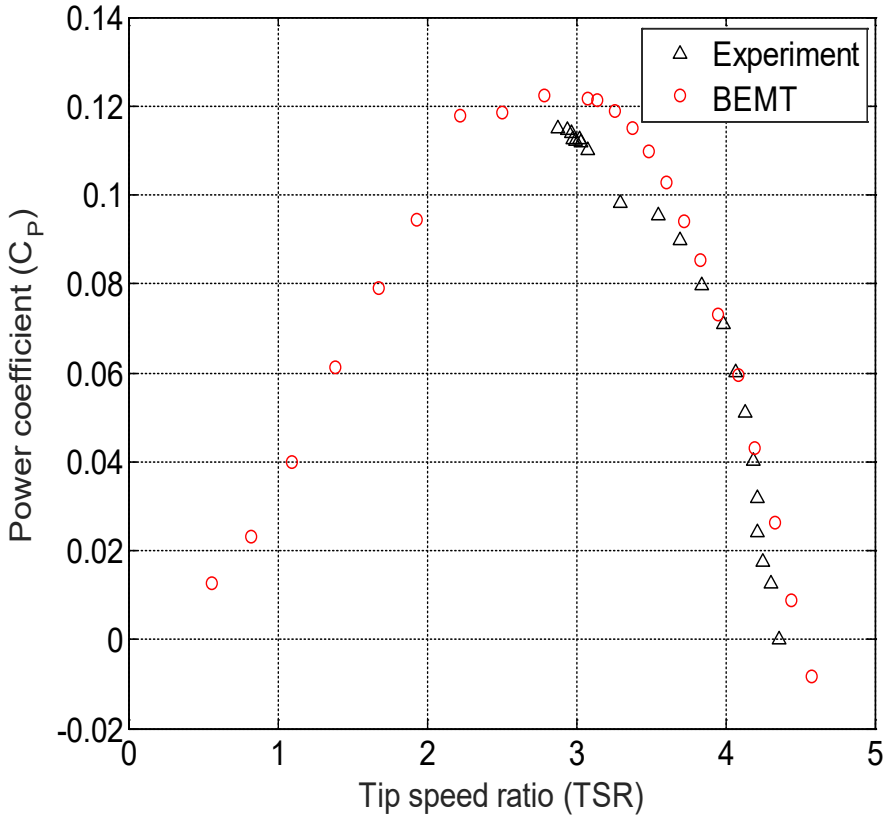

Figure 14. Power coefficient vs TSR at flow speed of 0.8161 m/s for three-blade turbine

5.3. FINITE ELEMENT MODEL

5.3.1. Blade Under Mechanical Load. The forces acting upon the blade during the experimental stage is required for the finite element model. In the experiments, the CFRP blades are subject to many forces. These forces have played a significant role in the performance of the blades. For instance, as the blade were slightly rotated to produce an angle between the surface of the blade and the loading cell during the bending tests, the performance of the unidirectional blades decreased significantly. On the other hand, the cross-ply blades ($[0^o/90^o]_S$) showed a consistent performance. The explanation of this difference in reaction to the rotation factor between both lay-up orientations is very simple.

During the process of applying the load, the load cell will touch the leading edge first which will create a moment. This load will try to break the fibers along the axial and radial directions. If the blade shape were as simple as a cantilever beam, then the fibers along the span direction would do a good job holding the structure together against the bending force. The fibers across the direction of the span will only hold the structure against the radial loads and any other torsional loads. However, the blade profile does not have a flat cantilever shape and therefore the hydrofoil of the blade is playing a major role in determining the forces acting upon it as well as how the blade will react to these forces.

There are three forces acting on the blade simultaneously. The first force is the moment caused by applying the load to one edge before the other, which will create a twist in the blade. The second force is the bending load, which is caused by pushing down the blade via the load cell. The third force is the shear force formed between the upper and the lower halves of the blade. All these forces were considered during the finite element modeling stage. The software used to study the failure analysis of the CFRP composite blades was ABAQUS CAE. For the sake of comparison and validation, the cross-ply blades were considered. The slope of the experimental curves for the cross-ply blades, which represents the bending modulus, was 1.09 N/mm calculated as the average slope of all samples. The slope of the simulation curve was 1.18 N/mm. Figure 15 shows the load vs. displacement curves of the simulation and experiments for the cross-ply blades. The average maximum load for experiments and simulation was 45.04 N and 47.10 N, respectively.

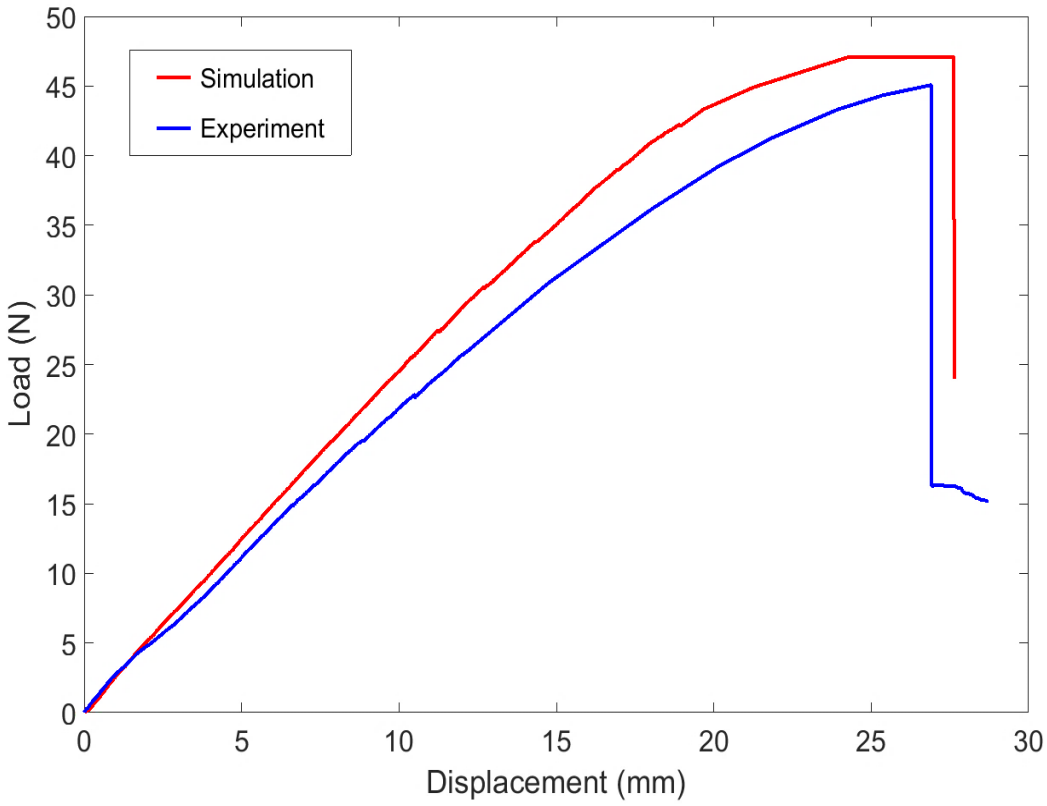

Figure 15. The load vs. displacement curve for the simulation results and the experimental results of the cross-ply CFRP composite blades

There was a discrepancy of 2.14 N between the experimental and simulated maximum loads. This can be attributed to an assumption that was made during the simulation. It was assumed that the interaction between the two halves of the blade is a "Tie" which means the two halves are perfectly bonded. This assumption was made due to the lack of the comprehensive information about the mechanical proprieties of the commercial adhesive that was used to join the two halves together. For maximum accuracy, it is recommended to perform mechanical tests on the adhesive material to obtain the exact values. Then, instead of selecting a "Tie" for the interaction between the two halves of the blade, a "Cohesive Behavior" should be selected and all the mechanical properties of the

adhesive material should be entered. By doing so, the difference between the simulation and experiments can be overcome.

In general, the maximum load, displacement, and slope were satisfactorily matched. The effect of introducing the pitch angle on the performance of CFRP blade with a different laminate stacking sequence was also investigated. The examined pitch angles that were selected to be tested are -10°, -5°, 0°, +5°, and +10° as shown in Figure 16. All of the angles are relative to the surface of the load cell.

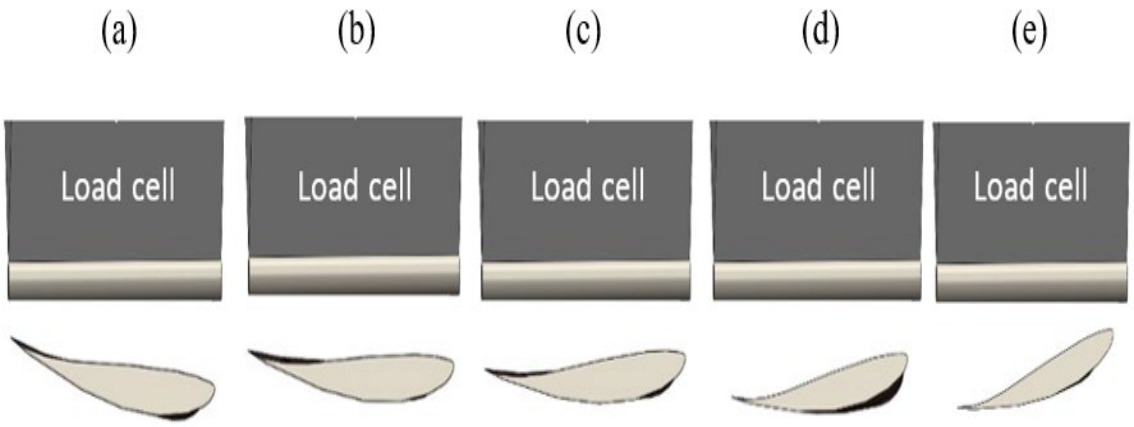

Figure 16. (a) CFRP blade with -10° pitch angle, (b) CFRP blade with -5° pitch angle, (c) CFRP blade with 0° pitch angle, (d) CFRP blade with +5° pitch angle, and (e) CFRP blade with +10° pitch angle

A dramatic decrease in the performance of the unidirectional composite blades was noticed when these angles were introduced as shown in Figure 17. The maximum load dropped by approximately 33.5% as the pitch angle changed from 0° to ±10°.

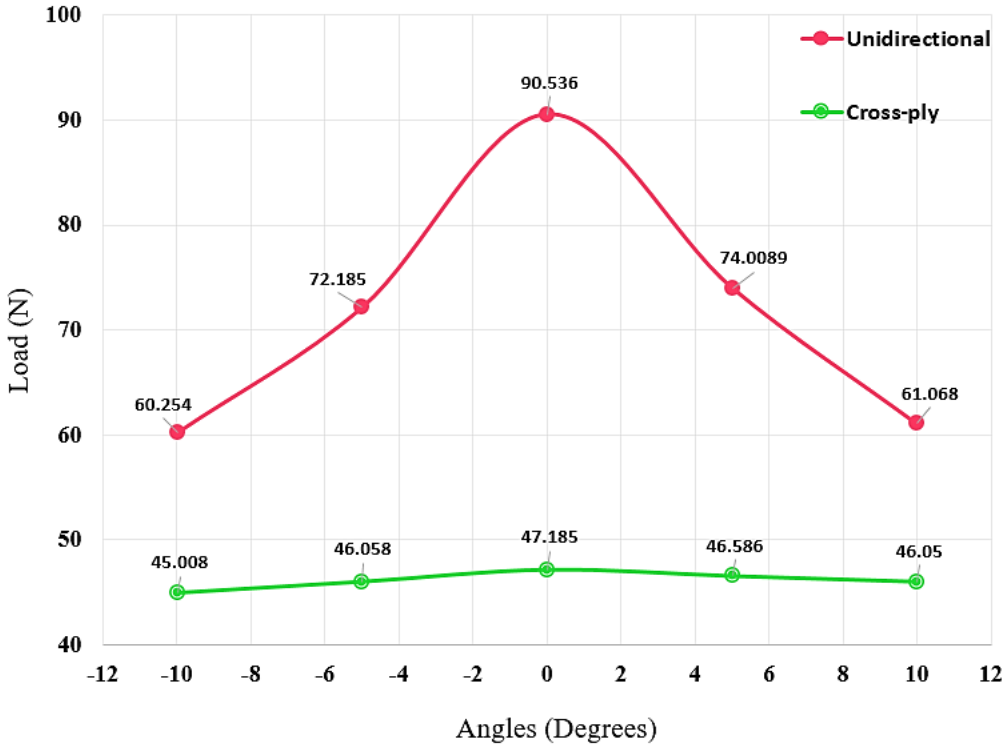

Figure 17. The maximum load of the CFRP composite blade with $[0^o]_4$ and $[0^o/90^o]_S$ laminate stacking sequences vs. the pitching angle

The curve followed a Gaussian distribution where the rate of performance degradation decreased as pitch angle deviated from zero. The performance of the cross-ply blades was barely affected within the tested range of pitch angles. The maximum load only decreased by 3.57% as the pitch angel altered form 0^o to $\pm 10^o$. The small decrease in the maximum load in the cross-ply blades was attributed to the fact that these blades are comprised of fibers that are oriented both along and across the blade span. These fibers will hold the bending and torsional loads and made these blades less responsive to the loading angle.

In Hashin's damage model, a value of more than unity represents a failure/damage initiation in the matrix that attains a complete damage at a value of unity. Figures 18 and 19 show the damage state of the matrix due to tension (DAMAGEMT) and shear (DAMAGEMSHR) for cross-ply blades, respectively. The DAMAGEMT and DAMAGEMSHR were the critical damage mechanisms compared to fiber/matrix compression, which was insignificant. The critical location of failure was at the root of the blade where stresses were concentrated due to the geometric shape, the boundary conditions, and the applied loading. This also was verified with the failure location of the experimental outcomes.

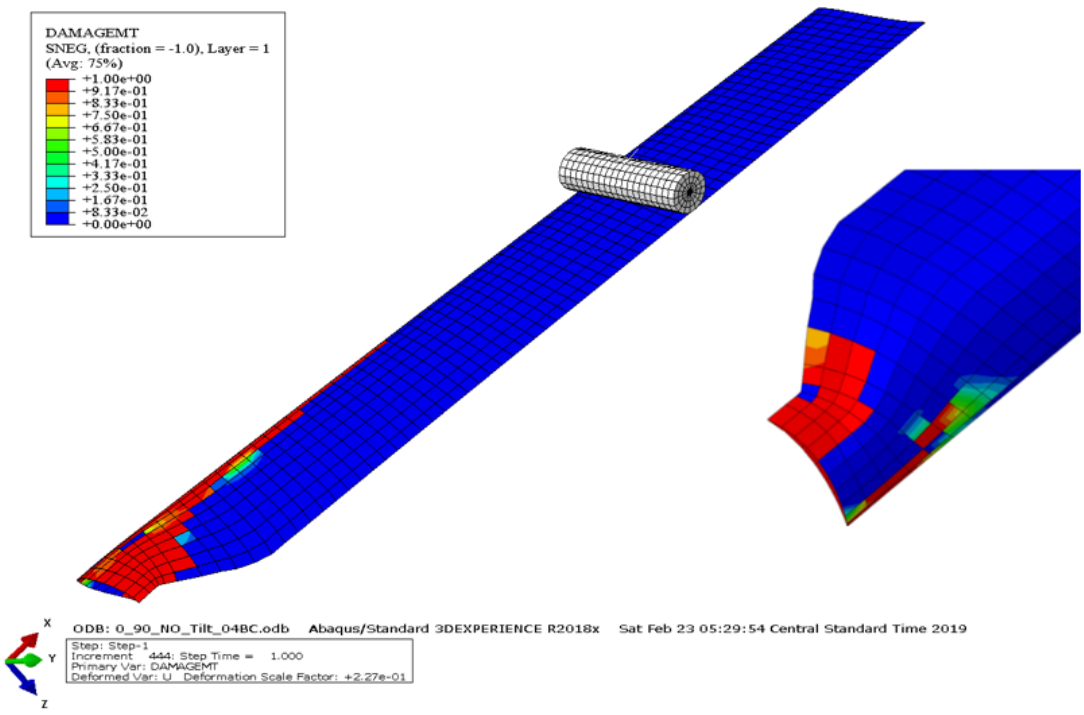

Figure 18. Damage state of the matrix due to tension (DAMAGEMT) for cross-ply blades ([0º/90º]s)

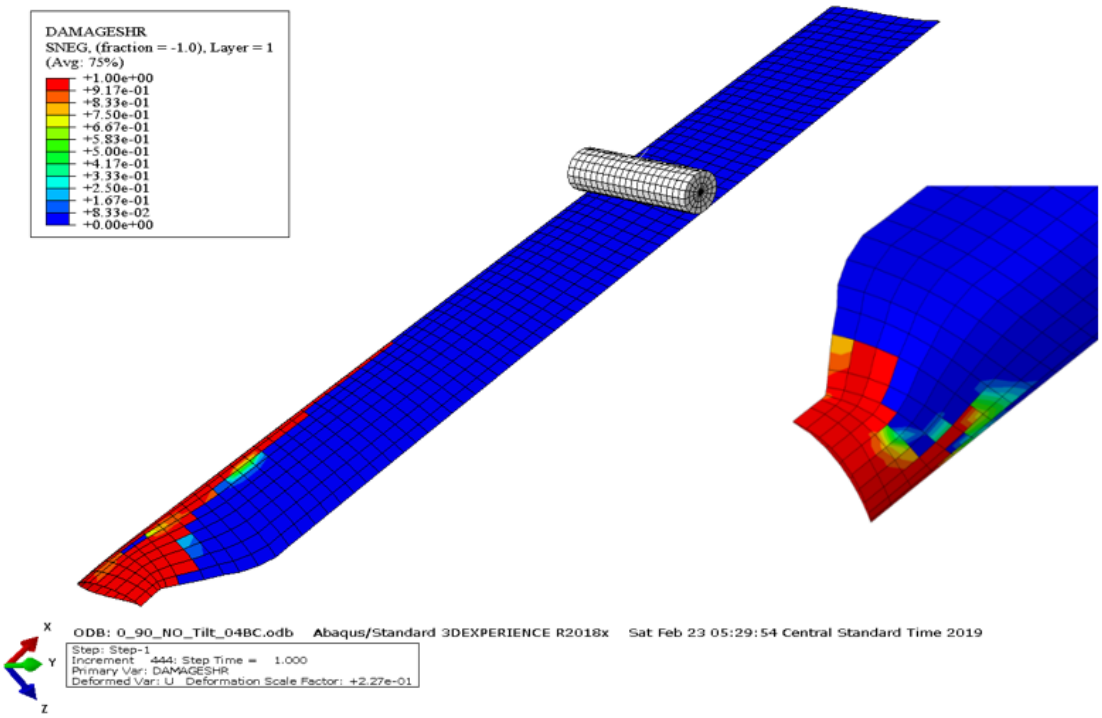

Figure 19. Damage state of the matrix due to shear (DAMAGEMSHR) for cross-ply blades ($[0^o/90^o]_S$)

5.3.2. Blade Under Hydrodynamic Load. The hydrodynamic forces due to the operation of the blade in a water tunnel under the velocity of 0.816 m/s were calculated using the BEMT. The forces were integrated over the blade elements and an average of the elemental pressure was calculated along the blade. The pressure was decomposed into normal (Pn) and tangential (Pt) tractions and then applied to the bottom surface of the composite blade. A second-degree polynomial was used to build the pressure analytical fields in ABAQUS CAE by considering the variation of the pressure in x-direction and y-direction of the blade. However, the applied pressure/traction was relatively small with the maximum values of normal pressure (Pn) = 1.3 kN/m^2 and tangential pressure (Pt) = 0.504

kN/m^2 which were located near the tip of the blade. The blade root was assigned a built-in boundary condition similar to the bending test simulation. Figure 20 and 21 show the maximum value of the matrix tensile initiation criterion experienced during the analysis for the unidirectional and the cross-ply blades respectively.

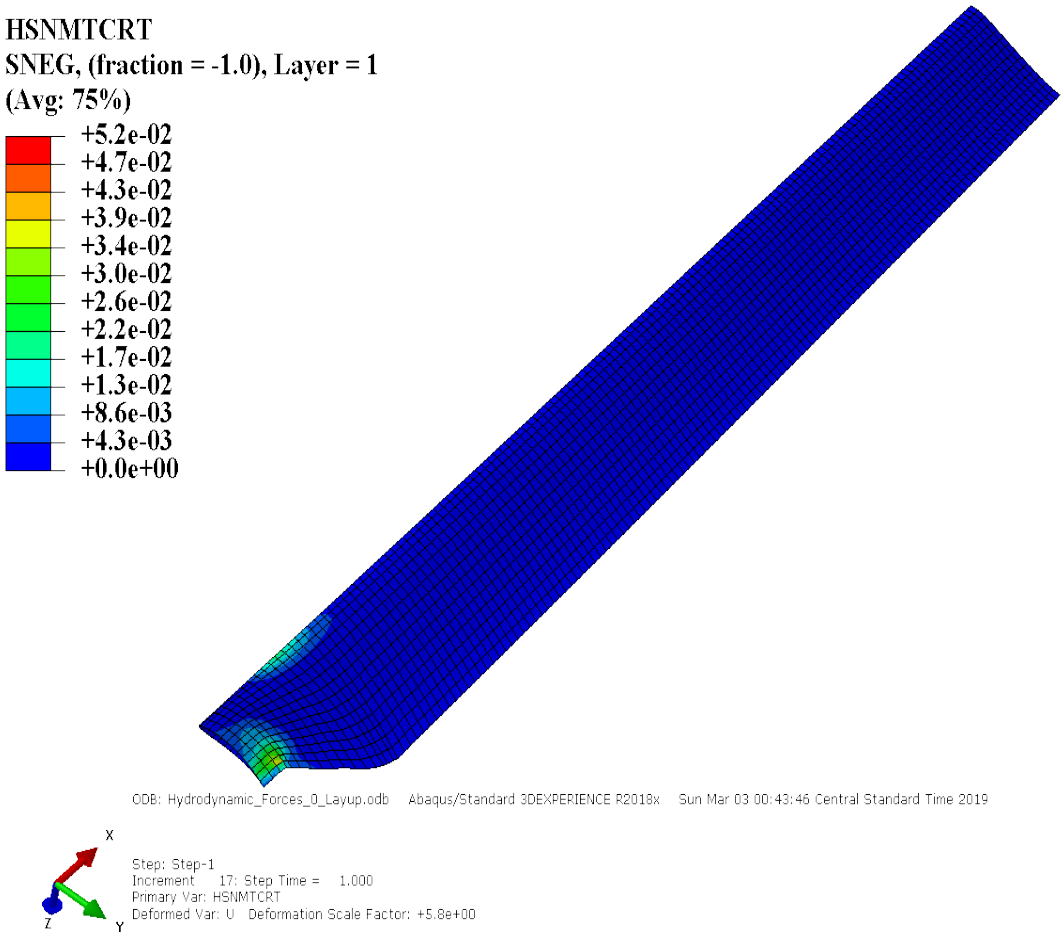

Figure 20. Hashin's failure criterion of the matrix due to tension (HSNMTCRT) for unidirectional blades

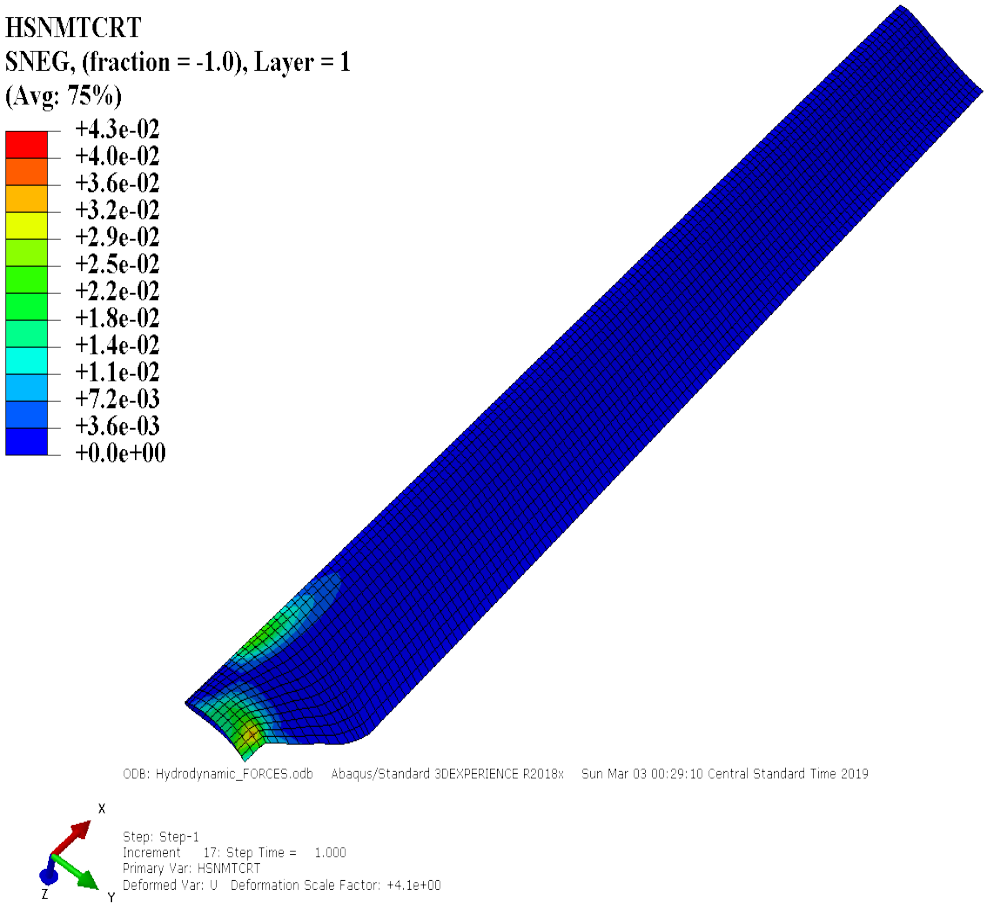

Figure 21. Hashin's failure criterion of the matrix due to tension (HSNMTCRT) for cross-ply blades

The critical location for all failure criteria was located at the root. However, the values of the criteria were in the order of 10^{-2}, which means the failure was not significant. It is important to note that, the periodic application of the small load/traction may induce failure due to fatigue, which was beyond the scope of the current work. The maximum principal stress due to the hydrodynamic forces was around 0.060 GPa which, as mentioned earlier, was located at the root of the blade.

6. CONCLUSION

Composite blades with different lay-ups were manufactured using the OOA process. The blades' mechanical performance was analyzed using flexural bending tests to investigate the behavior of the samples with different laminate stacking sequence. A FEA study was conducted to investigate the critical failure modes and locations under the operational loads and flexural bending loads. In both composite lay-ups, $[0^o/90^o]_S$ and $[0^o]_4$, the critical location of the failure was found to be near the root. The effect of rotating the CFRP blades during the bending tests was studied. The cross-ply CFRP blades showed a steady performance while the unidirectional blades performance dropped significantly. However, the unidirectional blades were noticed to withstand higher loads than the cross-ply even after being rotated 10^o in both directions (positive and negative). A Hashin's damage criterion was adopted to investigate the failure between the fibers and the matrix of the CFRP composite blades. Another finite element model was generated to further examine the interaction between the stress value/location and the layup orientation of the fibers in the blades. Under an operational condition of 0.816 m/s, a typical tidal current flow speed, the value of the failure was found to be insignificant for this blade size and configuration. However, hydrodynamic loads are periodic loads. Thus, a failure due to fatigue might accrue. This issue was beyond the scope of this study. In conclusion, unidirectional CFRP composite blades have proven they can withstand higher loads than conventional blade types, and therefore are able to have a longer service life compared to other layup orientations.

REFERENCES

[1] A. Akella, R. Saini, and M. P. Sharma, "Social, economical and environmental impacts of renewable energy systems," *Renewable Energy,* vol. 34, no. 2, pp. 390-396, 2009.

[2] J. Wang, J. Piechna, and N. Müller, "A novel design of composite water turbine using CFD," *Journal of Hydrodynamics, Ser. B,* vol. 24, no. 1, pp. 11-16, 2012.

[3] I. Yüksel, "Hydropower in Turkey for a clean and sustainable energy future," *Renewable and Sustainable Energy Reviews,* vol. 12, no. 6, pp. 1622-1640, 2008.

[4] L. C. Ciocci, "Keeping water in the US mix," *IEEE Power and Energy Magazine,* vol. 6, no. 4, pp. 36-39, 2008.

[5] D. Le Gourieres, *Wind power plants: theory and design*. Elsevier, 2014.

[6] N. Dalili, A. Edrisy, and R. Carriveau, "A review of surface engineering issues critical to wind turbine performance," *Renewable and Sustainable energy reviews,* vol. 13, no. 2, pp. 428-438, 2009.

[7] I. S. Hwang, Y. H. Lee, and S. J. Kim, "Optimization of cycloidal water turbine and the performance improvement by individual blade control," *Applied Energy,* vol. 86, no. 9, pp. 1532-1540, 2009.

[8] L. I. Lago, F. L. Ponta, and L. Chen, "Advances and trends in hydrokinetic turbine systems," *Energy for Sustainable Development,* vol. 14, no. 4, pp. 287-296, 2010.

[9] A. Bahaj and L. Myers, "Fundamentals applicable to the utilisation of marine current turbines for energy production," *Renewable Energy,* vol. 28, no. 14, pp. 2205-2211, 2003.

[10] P. Brøndsted, H. Lilholt, and A. Lystrup, "Composite materials for wind power turbine blades," *Annu. Rev. Mater. Res.,* vol. 35, pp. 505-538, 2005.

[11] U. Dorji and R. Ghomashchi, "Hydro turbine failure mechanisms: An overview," *Engineering Failure Analysis,* vol. 44, pp. 136-147, 2014.

[12] E. De Jaeger, N. Janssens, B. Malfliet, and F. Van De Meulebroeke, "Hydro turbine model for system dynamic studies," *IEEE Transactions on Power Systems,* vol. 9, no. 4, pp. 1709-1715, 1994.

[13] G. S. Bir, M. J. Lawson, and Y. Li, "Structural design of a horizontal-axis tidal current turbine composite blade," *ASME 2011 30th International Conference on Ocean, Offshore and Arctic Engineering,* pp. 797-808, 2011.

[14] P. Lissaman, "Low-Reynolds-number airfoils," *Annual review of fluid mechanics,* vol. 15, no. 1, pp. 223-239, 1983.

[15] B. L. Storms and C. S. Jang, "Lift enhancement of an airfoil using a Gurney flap and vortex generators," *Journal of Aircraft,* vol. 31, no. 3, pp. 542-547, 1994.

[16] M. Drela, "XFOIL: An analysis and design system for low Reynolds number airfoils," in *Low Reynolds number aerodynamics*: Springer, 1989, pp. 1-12.

[17] A. S. Yaghoubi and B. Liaw, "Effect of lay-up orientation on ballistic impact behaviors of GLARE 5 FML beams," *International Journal of Impact Engineering,* vol. 54, pp. 138-148, 2013.

[18] C. Kong, J. Bang, and Y. Sugiyama, "Structural investigation of composite wind turbine blade considering various load cases and fatigue life," *Energy,* vol. 30, no. 11–12, pp. 2101-2114, 2005.

[19] E. Fuoss, P. V. Straznicky, and C. Poon, "Effects of stacking sequence on the impact resistance in composite laminates—Part 1: parametric study," *Composite Structures,* vol. 41, no. 1, pp. 67-77, 1998.

[20] T. Kant and K. Swaminathan, "Estimation of transverse/interlaminar stresses in laminated composites–a selective review and survey of current developments," *Composite Structures,* vol. 49, no. 1, pp. 65-75, 2000.

[21] Z. Hashin, "Failure criteria for unidirectional fiber composites," *Journal of Applied Mechanics,* vol. 47, no. 2, pp. 329-334, 1980.

[22] Z. Hashin and A. Rotem, "A fatigue failure criterion for fiber reinforced materials," *Journal of Composite Materials,* vol. 7, no. 4, pp. 448-464, 1973.

[23] S. Anandan, G. Dhaliwal, Z. Huo, K. Chandrashekhara, N. Apetre, and N. Iyyer, "Curing of thick thermoset composite laminates: multiphysics modeling and experiments," *Applied Composite Materials,* vol. 25, no. 5, pp. 1155-1168, 2018.

[24] H. Koerber and P. P. Camanho, "Simulation of progressive damage in bolted composite joints," presented at the 13th European conference on composite materials, Stockholm, Sweden, 2008.

[25] A. Demir, H. Ozturk, K. Edip, M. Stojmanovska, and A. Bogdanovic, "Effect of Viscosity Paramter on The Numerical Simulation of Reinforced Concrete Deep Beam Behavior," *The Online Journal of Science and Technology,* vol. 8, no. 3, pp. 50-56, 2018.

[26] A. Demir, H. Ozturk, and G. Dok, "3D numerical modeling of RC deep beam behavior by nonlinear finite element analysis," *Disaster Science and Engineering,* vol. 2, no. 1, pp. 13-18, 2016.

[27] Z. Du and M. S. Selig, "A 3-D stall-delay model for horizontal axis wind turbine performance prediction," presented at the ASME Wind Energy Symposium, Reno, NV, Jan. 12-15, 1998.

[28] A. Eggers, K. Chaney, and R. Digumarthi, "An assessment of approximate modeling of aerodynamic loads on the UAE rotor," *ASME 2003 Wind Energy Symposium,* pp. 283-292, 2003.

[29] L. A. Viterna and R. D. Corrigan, "Fixed Pitch Rotor Performance of Large Horizontal Axis Wind Turbines," *NASA Lewis Research Center,* pp. 69-85, 1982.

[30] D. Hu, O. Hua, and Z. Du, "A study on stall-delay for horizontal axis wind turbine," *Renewable Energy,* vol. 31, no. 6, pp. 821-836, 2006.

[31] J. L. Tangler, "Insight into wind turbine stall and post-stall aerodynamics," *Wind Energy,* vol. 7, no. 3, pp. 247-260, 2004.

II. INVESTIGATION OF LAMINATE DEBONDING IN HORIZONTAL AXIS WATER TURBINE COMPOSITE BLADES

Mokhtar Fal, Abdulaziz Abutunis, and K. Chandrashekhara*

Department of Mechanical and Aerospace Engineering, Missouri University of Science and Technology, Rolla, MO 65409

Gurjot S. Dhaliwal

Intertribal Research and Resource Center, United Tribes Technical College, Bismarck, ND 58504

ABSTRACT

Carbon fiber reinforced polymer (CFRP) composites are becoming popular due to their superior strength to weight ratio and stiffness properties. This study highlights the interlaminar debonding growth, which is considered one of the most frequent problems with composite materials. A three-blade horizontal axis water turbine (HAWT) was manufactured using IM7/Cycom5320-1 carbon/epoxy prepreg. During the process of manufacturing, a specific number of Teflon sheets were placed between the composite layers in two locations to create a separation between the layers and to investigate the delamination growth. Three different laminate stacking sequences were selected to be tested: $[0^o]_4$, $[0^o/90^o]_S$, and $[45^o/-45^o]_S$. The composite blades were placed in a water tunnel and run for 3 million revolutions. A thermography analysis was carried out to evaluate the propagation and growth of the delamination. A one-way fluid-structure interaction (FSI) model was created and implemented to obtain the stress values along the blade. The results showed the influence of the composite layup orientation on the growth of the delamination. The unidirectional blades ($[0^o]_4$) showed the lowest amount of propagation while the cross-

ply ($[0^o/90^o]_S$) showed the most delamination growth. The bottom location (near the root) showed the maximum delamination. Both sides of the blades showed significant delamination growth. However, the backside showed more interlaminar debonding growth than the front side. After three million revolutions, the percentage of debonding growth for the bottom/backside of the blades was 6.58%, 36.25%, and 27.63% for the $[0^o]_4$, $[0^o/90^o]_S$, and $[45^o/-45^o]_S$, respectively.

1. INTRODUCTION

Global warming caused by using non-renewable energy is forcing scientists to find alternative ways to generate power. One of the most promising sources of clean energy is hydrokinetic energy. Hydrokinetic energy can be generated when the natural movement of water (oceans, streams, currents, etc.) forces a submerged turbine to rotate, which is connected to a power generator. There are numerous advantages of adopting such a resource of renewable energy. First, it is renewable, meaning that it is harvested from a source that does not deplete within a human's lifetime. In addition, about 33% of the human population does not have access to electricity but does have access to a source of continuous moving water [1]. Another advantage of using hydrokinetic energy over other sources of renewable energy is the consistency of power generation [2]. Solar energy generation, for example, is limited by the amount of direct sunlight. Cloudy, dusty, foggy, or rainy days are not the ideal days to extract energy via solar panels. In addition, there is a possible danger that comes from the excessive heat that might burn up the wires and causes a disaster such as the famous incident on December 4, 2017, of California forest fires [3, 4].

Alternatively, the hydropower energy can be continuously generated via the unending movement of rivers, streams, and ocean waves [5]. However, there are challenges to generate power from hydrokinetic water turbines. The most obvious challenge to overcome is the harsh environment that the turbines operate in. To overcome this challenge, good design and strong components are needed. The water turbine blades undergo about 800 times the amount of force that wind turbine blades go through [6]. Therefore, it is essential to study and improve the blade structure to attain the best performance.

In recent years, composite materials have become extremely popular due to their superior specific strength, stiffness, and other mechanical properties [7-9]. Marine applications are no exception, as many marine structures are now made fully, or in part, from composite materials [10]. Structures that have direct contact with water must have high corrosion resistance, high specific, and low water/moisture absorption [11]. Composite materials are a combination of two or more materials that form a new material that has better properties than each constituent by itself [12]. Composite materials give the best qualities of each component, but in many cases, they give new qualities that neither of its components possesses. There are many classifications of composite materials[13]. Carbon fiber reinforced composites are very popular due to their superior mechanical performance [14, 15]; however, they are not invulnerable against failure.

Unlike metals where the stresses on a crack can be defined analytically at the crack tip [16], composite materials have a damage zone that may include fiber pullout, fiber microbuckling, fiber fracture, matrix cracking, delamination, laminate debonding, or any combination of these failure mechanisms. Debonding growth is a common failure that tends to occur within composite materials. Debonding tends to propagate between the

laminates when load is applied [17-22]. In 1980, Zvi Hashin [23] proposed a finite element model that can predict the interlaminar failure in fiber-reinforced composite materials. However, due to the complexity of the calculations and the time it requires to include the plane orientation in the model, Hashin excluded it from the calculations [24]. Over a decade later, Hashine's model was extended to account for three interlaminar failure modes: (I) a tensile matrix failure, (II) a compressive shear matrix failure, and (III) a complex failure mode in which the plane of the fracture rotates about an axis to form a tapered section which can cause a fiber failure in the adjacent layers. However, different applications will utilize composite structures differently. Thus, it is impossible to perform failure analysis for fiber-reinforced composite materials that are valid for predicting all kinds of failure. Therefore, further investigation is needed to extend the existing finite element models for each specific application. The focus of this study is to investigate the behavior of delamination growth in horizontal axis water turbine CFRP blades undergoing working conditions. Many forces are applied on the turbine blade during the process of generating power. The delamination might react differently under these forces and propagate differently.

The phenomenon of interlaminar debonding in composite materials is influenced by many factors. However, the lack of perfect bonding between the laminates during the curing/post-curing process is considered the most common reason [25-27]. This interlaminar debonding creates poor in-plane properties and decreases the impact of resistance [28-30]. The reduction of the structural integrity of the laminates will negatively affect the mechanical performance and will rapidly increase the rate of deterioration of the composite structure [31]. Many studies have been done to investigate the delamination

behavior in various applications. However, no significant work has been done on composite hydrokinetic turbine systems in terms of blade structural design, failure analysis, experimental evaluation, and performance assessment. This work fills this gap and provides a comprehensive study on how the debonding between the laminates with different lay-up orientation will behave in marine applications where different loads (static/dynamic pressures, and axial/angular momentums) are applied.

2. COMPOSITE TURBINE BLADE

2.1. HYDROFOIL SELECTION

The first step in manufacturing the carbon fiber reinforced polymer (CFRP) composite blade is the selection of the hydrofoil. The hydrofoil can be defined as the shape and curvature of the blade. This step is essential to the proper design of the turbine blade because different hydrofoils create different lift and drag forces. The lift and drag, along with other factors, are important to determine the amount of power generated by any horizontal axis water turbine (HAWT) [32]. As a rule of thumb, it is desirable to use a hydrofoil that will provide a high lift-to-drag ratio. All twisted hydrofoils have been eliminated from the selection process because they introduce an extra factor that will affect the delamination growth. Therefore, only untwisted hydrofoils were considered for this study. Eppler 395 was selected to be the hydrofoil and the molds needed to fabricate the blades were additively manufactured. Figure 1 presents the lift-to-drag ratio for Eppler 395 at different Reynolds numbers.

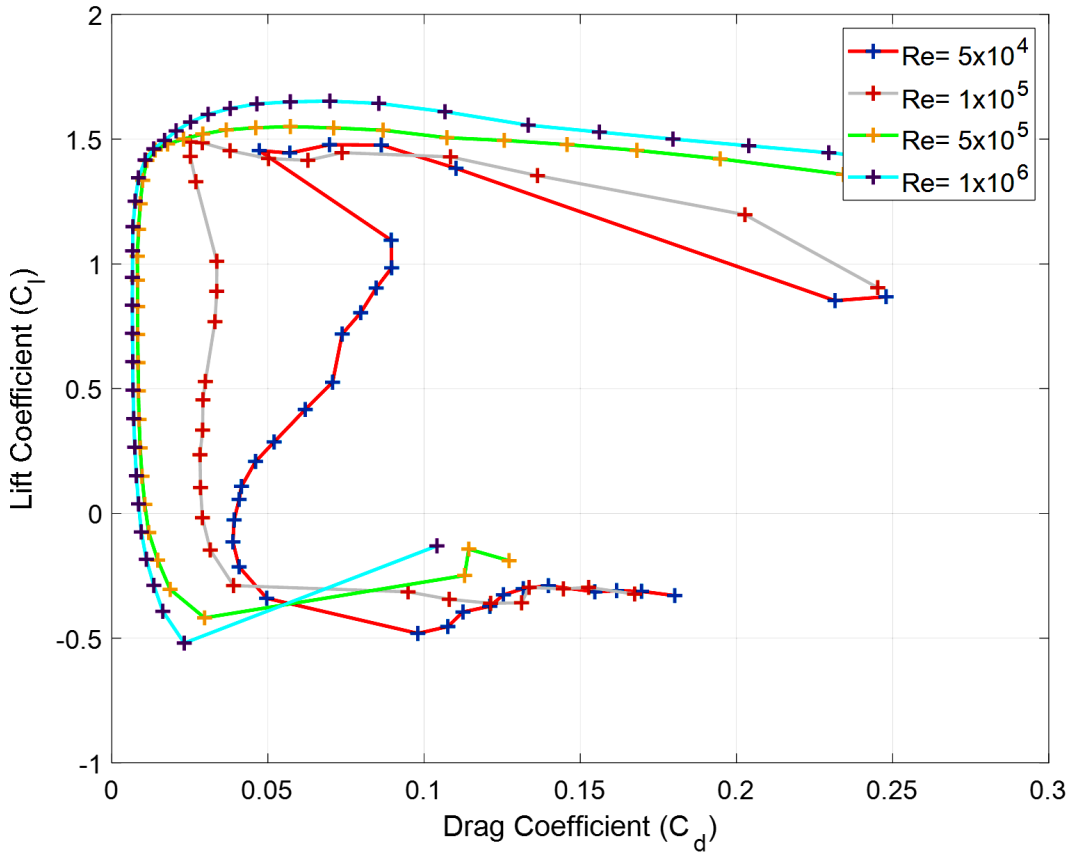

Figure 1. The lift coefficient (C_l) vs. drag coefficient (C_d) for the hydrofoil Eppler 395 at different Reynolds numbers

2.2. ADDITIVELY MANUFACTURED MOLDS

Molds can be manufactured via many different techniques. Recently, additive manufacturing (AM), also known as rapid prototyping and three-dimensional (3-D) printing, has become very popular because it offers several advantages over traditional techniques. AM for non-mass production is fast, convenient, autonomous, cheap, and can produce high-quality complex shapes [33]. In this study, AM was used to manufacture the complex shape of the Eppler 395 mold for the turbine blades. ULTEM 9085 molds were manufactured using the fused deposition modeling (FDM) process using Fortus 400mc

(Stratasys, USA) machine at Missouri University of Science and Technology. There were four main stages during the manufacturing process. The first stage started with generating a three-dimensional CAD model for the mold before saving it as a Stereo Lithography (STL) file. After that, the model was exported to the Fortus 400mc machine. In the second stage, the machine began the fabrication process using ULTEM 9085 filament. Next, the FDM parts were detached from the support materials. This process was repeated twice to manufacture both the upper and the lower halves of the Eppler 395 molds. In the final stage, the molds went through a finishing process. The aim was to meet the ISO 1302 surface roughness grade of N10. This ISO number is equivalent to 12.5µm.

3. EXPERIMENTAL PROCEDURE

3.1. MATERIALS AND LAY-UP ORIENTATIONS

Material selection is a crucial stage in any engineering design process. In this study, IM7/Cycom 5320-1 carbon/epoxy prepreg (manufactured by Cytec Materials Inc.) was selected to be the primary material to manufacture the CFRP blades for the HAWT. It was specially designed for the out-of-autoclave (OOA) manufacturing processes. It has the ability to cure at relatively low temperatures, which allows it to be suitable for prototyping where thermoplastic-based tooling can be used [34]. Although Cycom 5320-1 is designed for the OOA manufacturing process, it can produce high-quality samples with low porosity [35, 36]. Elastic and strength properties of the IM7/Cycom 5320-1 carbon/epoxy prepreg are listed in Table 1 [36].

Table 1. Material properties of the IM7/Cycom 5320-1 carbon/epoxy prepreg

Property	Symbol	Value
Longitudinal tensile modulus	E_{11}	156 GPa
Transverse tensile modulus	E_{22}	9.3 GPa
Longitudinal Poisson's ratio	ν12	0.3
Longitudinal shear modulus	G12	5.5 GPa
Transverse shear modulus	G23	5.4 GPa
Longitudinal tensile strength	XT	2.503 GPa
Longitudinal compressive strength	XC	2.078 GPa
Transverse tensile strength	YT	759 MPa
Transverse Compressive strength	YC	165 MPa
Longitudinal and Transfer shear strength	SL and ST	73 MPa

To study the effect of the lay-up orientation, three different laminate stacking sequences were selected: (a) $[0^o]_4$, (b) $[0^o/90^o]_S$, and (c) $[+45^o/-45^o]_S$. All CFRP blades with these lay-up orientations were manufactured using the OOA procedure.

3.2. MANUFACTURING OF LAMINATES WITH DEBONDING

This study investigates the effect of lay-up orientation on interlaminar debonding within HAWT blades; therefore, interlaminar defects with known dimensions were implemented. The separation between the layers was created by placing non-stick Teflon sheets in two different locations along the blade span. Locations were selected to be near the root of the blade and in the middle of the blade. The exact locations of the Teflon sheets,

as well as the dimensions, are shown in Figure 2. Each blade was made using eight plies of IM7/Cycom 5320-1 carbon/epoxy prepreg. Four plies were used for the upper half of the blade (mold), and the remaining four were used to create the bottom half of the CFRP blade. The Teflon sheets were placed in the middle of each stack, which is between ply number 2 and ply number 3 in both halves of the blade. After curing the CFRP blades, the Teflon sheets were able to create the desired interlaminar separation. Thermography images were taken to confirm the separation. Finally, three blades with the three different lay-up orientations were manufactured and attached to a hub and tested in the water tunnel.

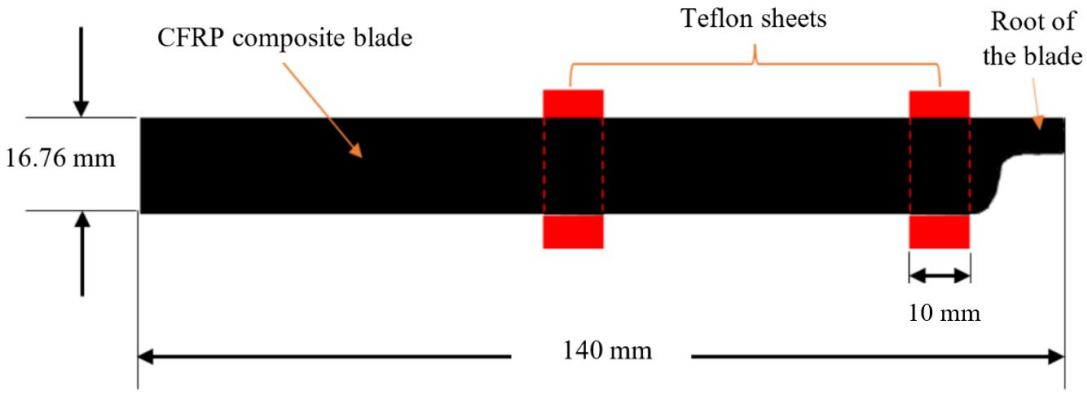

Figure 2. The two selected locations of Teflon sheets to induce debonding between the laminates

3.3. WATER TUNNEL TEST

A 1520-HK research water tunnel (Figure 3) located at Missouri S&T was utilized to measure the power generated by a three-blade CFRP composite water turbine. The water tunnel test section has length, width, and depth of 60 inches (152.4 cm), 15 inches (38.1 cm), and 20 inches (50.8 cm), respectively, and a maximum water velocity of 3.28 ft/second

(1 m/second). It has an overall capacity of 1,000 gallons (3,785.4 liters). To withstand the pressure of the water, the tempered glass in the test section is 0.375 inches (9.52 mm) thick on the sidewalls and 0.2 inches (5.08 mm) thick on the bottom. This water tunnel uses a LM16234 motor with 10 HP, 230 VAC, and 33 amps. This was desirable because the pump was configured as a direct drive unit (no pulley gearing).

Figure 3. The 1520-HK research water tunnel located at Missouri S&T

The torque and rotational speed required to calculate the power were attained using a 0.353 N.m FUTEK reaction torque sensor and a time-average RPM sensor. By using the trial and error approach, the optimum pitch angle of the blade with the Eppler 395 hydrofoil was found to be around 5°. However, to avoid operating under extreme hydrodynamic

loadings and thus the possibility of rapid failure of the blades during the experiments, the blades were pitched to 20^o while the flow speed was set to 0.816 m/s. The power coefficient (C_P) versus tip speed ratio (TSR) curve was generated by applying incremental load on the turbine system output shaft by the mean of 0.226 N.m magnetic particle clutch. The experiment setup is illustrated in Figure 4. Increasing the applied load will raise the torque and reduce TSR. The optimum TSR (the TSR at the maximum power) was found to be approximately 2.87 from the experiment results. The 3-blade CFRP composite turbine was operated in the water tunnel at the optimum TSR for 1 million, 2 million, and 3 million revolutions to investigate the blades interlaminar debonding behavior.

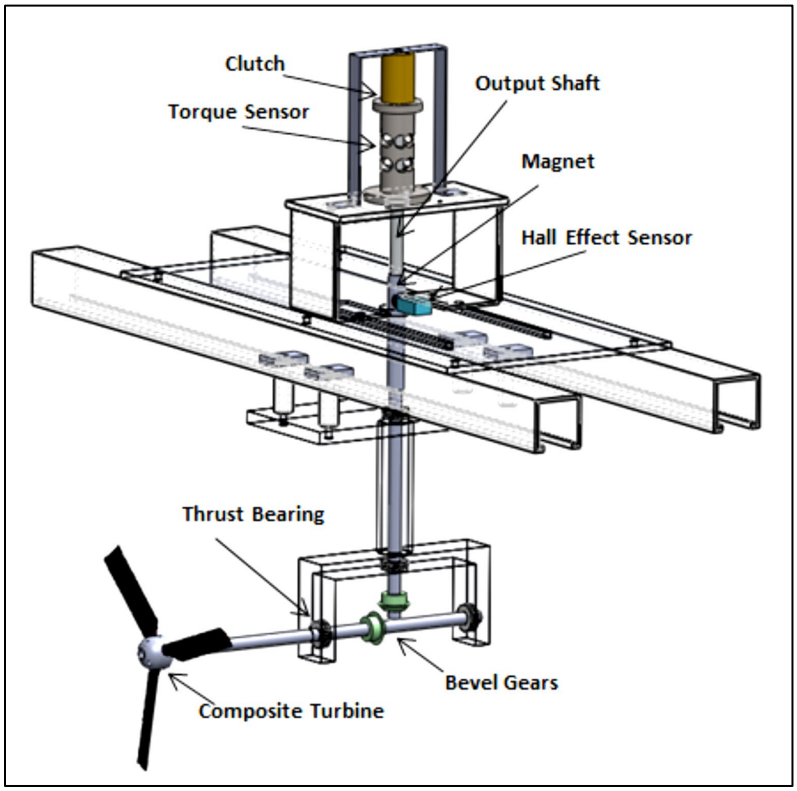

Figure 4. The complete setup for testing the 3-blade CFRP composite turbine in the 1520-HK research water tunnel

3.4. THERMOGRAPHY ANALYSIS

Thermography analysis is a non-destructive test in which images are taken for an object under investigation to show the energy leaving a surface as radiant heat[37]. Every object radiates energy that is transported in the form of electromagnetic waves[38]. In this study, measuring the quantity of the energy leaving the body was not the primary goal. Instead, the energy distribution along the span of the blade as a form of heat was the core objective. The heat distribution shows the locations of the interlaminar defects based on the color distribution. The thermography images showed the area of the interlaminar defect before the blades start operating in the water tunnel, after 1 million revolutions, 2 million revolutions, and 3 million revolutions. In every iteration, blades were taken out of the water tunnel, and the area of delamination was measured based on the images provided by the infrared camera. A FLIR camera was used to capture the thermal images, and the samples were heated using two 2.5 kW halogen lamps. The prepared samples were placed at a distance that would show both locations clearly. The distance ranged from 10 to 12 inches (25.4 – 50.8 cm) from the camera. A simple thermography analysis testing setup is shown in Figure 5. For thermographic evaluation, the samples were heated for 180 seconds and allowed to cool down. The thermal camera recorded the temperature profile during the entire heating and cooling process. The recorded images were analyzed using ImageJ software to measure the area after each iteration. The captured images were evaluated to investigate the development of delamination growth after each iteration.

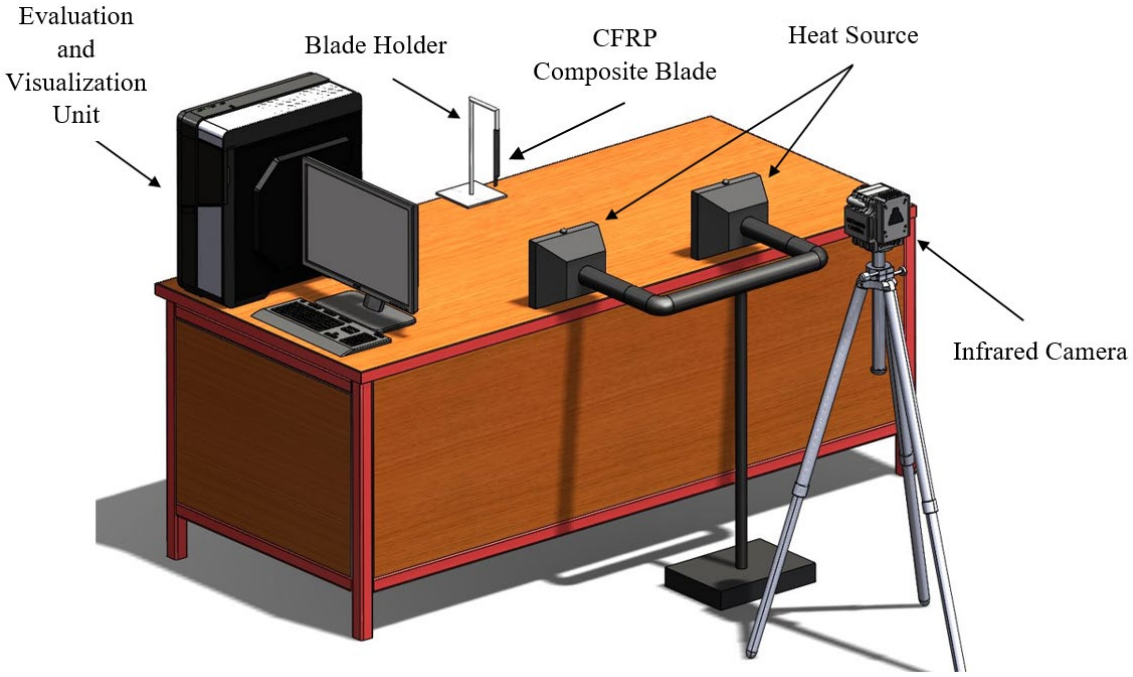

Figure 5. Thermography analysis testing setup

4. FLUID-STRUCTURE INTERACTION

A high fidelity one-way FSI was reported to provide satisfactory solutions while involving lower computational effort compared to a two-way FSI [39]. The one-way FSI simulation was performed to obtain hydrodynamic loads and structural response of the turbine blades. The FSI results are then used to characterize the delamination at the Teflon regions. The CFD and FEA approaches were used to find the deflections and stresses on the blades, as shown in the flowchart in Figure 6.

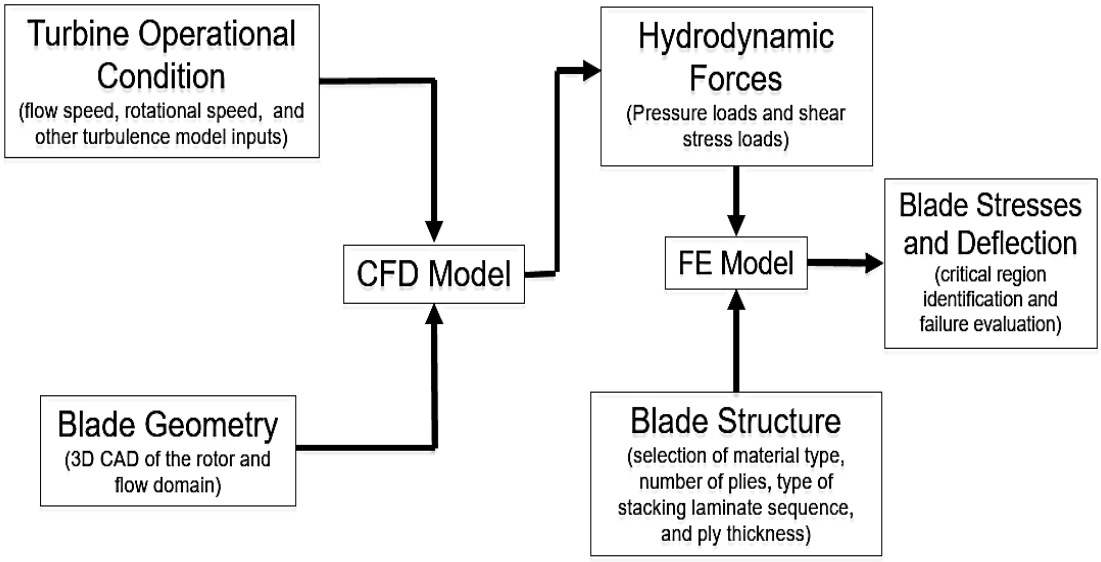

Figure 6. Flow chart for the one-way FSI analysis procedure

4.1. COMPUTATIONAL FLUID DYNAMIC MODEL

A CFD simulation was employed to calculate the hydrodynamic loads on the turbine blades using the commercial software of ANSYS 18.2/Fluent. The mesh, turbulence model, used solver, and employed boundary conditions (BCs) are discussed below:

4.1.1. Geometry and Meshing. The used rotor is a three-blade rotor. The blades were untwisted, had a fixed chord length of 0.66 inches (1.67 cm), and a span length of 5.5 inches (13.97 cm). The hub had a diameter of 1.25 inches (3.17 cm). The water tunnel was given a cross-section of 15 inches × 20 inches (38.1 cm × 50.8 cm). All these dimensions were identical to those used in the experiment. The water tunnel stream-wise dimension was designed such that the rotor upstream and downstream lengths were 10x the diameter of the rotor and 25x the diameter of the rotor, respectively. The rotor and the water tunnel were meshed separately using ANSYS 18.2/ICEM. The rotor blades were meshed

separately. Each blade was surrounded by the flow domain that represented one-third of a cylinder (Figure 7a). The water tunnel was assigned a mesh size of 3.55 million with a finer grid towards the rotor domain (Figure 7b). The rotor domain was subtracted from the tunnel domain (the domains were integrated afterword as unstructured meshes in Fluent). All common surfaces between blades domains and between the blades domains and water tunnel domain were defined as interfaces, and the corresponding interfaces were linked. This was to allow the later incorporation of a moving reference frame (MRF) technique used by the turbulence model to accelerate the calculation. Because the water tunnel domains were stationary, and rotor domains were moving, the generated interfaces were non-conformal (had non-matched nodes). These interfaces transferred velocity and velocity gradient from one mesh to another when the MRF approach was utilized.

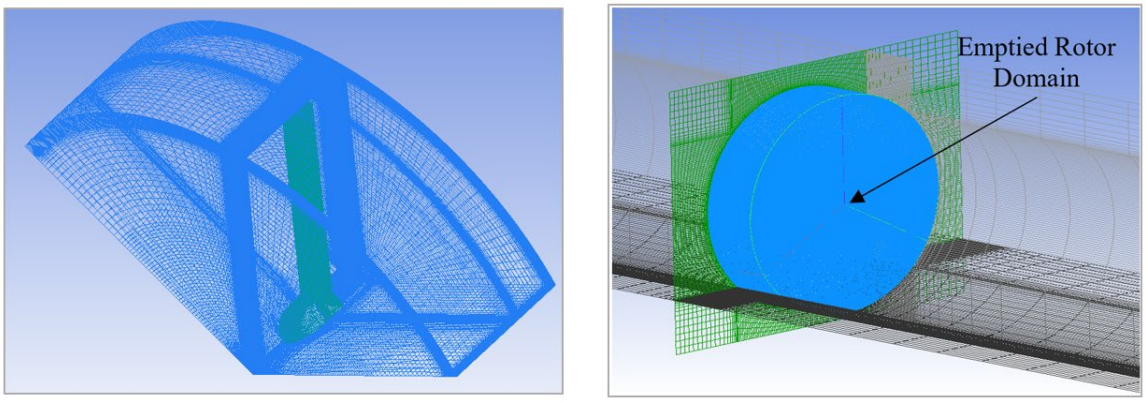

(a) (b)

Figure 7. The structured mesh of (a) one-third of the rotor and (b) rotor domain in the water tunnel (scan planes were used to illustrate the water tunnel mesh distribution)

A mesh sensitivity study was conducted to determine the appropriate mesh size that yields a solution independent of the mesh size. Table 2 shows the operational conditions

and the resulted moment coefficient (C_M) and its relative error (ε) calculated with respect to the finest mesh. The mesh size of 1.91 million was considered. This mesh size yielded a relative error that is less than 5% and allowed a faster-converged solution compared to the larger mesh sizes.

Table 2. The moment coefficient (C_M) and the relative error (ε) based on different operational conditions

Pitch angle (degree)	Velocity (m/s)	Rotational speed (RPM)	Mesh size per blade domain in millions	Grids along the foil	CM	ε (%)
20	0.911	375	1.46	109	0.001755	40.69
			1.91	165	0.002364	4.42
			2.76	226	0.002373	4.01
			3.06	250	0.002413	2.31
			4.24	339	0.002469	0

4.1.2. Turbulence Model. The selected turbulence model was Shear Stress Transport ($SST\ k-\omega$) [40]. The $SST\ k-\omega$ model was chosen due to its capability of predicting adverse pressure gradient flows, which occurs in water turbines [41, 42]. The turbulence model was considered steady, and a multiple moving reference frames (MRF) approach was incorporated. In MRF, the flow within the rotor domain is steady with respect to the rotating blades, which further simplifies and accelerates solving the turbulence model. The governing equations utilized by the moving reference frame in steady turbulence model are as below [43]:

$$\frac{\partial \rho}{\partial t} + \vec{\nabla} \cdot \vec{U}_r = 0 \quad (1)$$

$$\frac{\partial}{\partial t}\left(\rho \vec{U}_r\right) + \vec{\nabla} \cdot \left(\rho \vec{U}_r \vec{U}_r\right) + \rho\left(2\vec{\Omega} \times \vec{U}_r + \vec{\Omega} \times \vec{\Omega} \times \vec{r}\right) = -\vec{\nabla} p + \vec{\nabla} \cdot \bar{\bar{\tau}}_r + \vec{F} \quad (2)$$

where, $\vec{U}_r$ is the relative velocity and is defined as $\vec{U}_r = \vec{U} - \vec{\Omega} \times \vec{r}$, where $\vec{U}$ is flow velocity. The Coriolis and centripetal forces are introduced in the MRF momentum equation through the terms $\rho\left(2\vec{\Omega} \times \vec{U}_r\right)$ and $\rho(\vec{\Omega} \times \vec{\Omega} \times \vec{r})$ respectively, where $\vec{\Omega}$ is the angular velocity, $\vec{\nabla} p$ is the pressure gradient through the rotor, $\bar{\bar{\tau}}_r$ is the viscous shear stress tensor, and $\vec{F}$ is the external force. For the current steady-state simulation of the turbine, the first term in Equation 1 ($\frac{\partial \rho}{\partial t}$) and the last term in Equation 2 ($\vec{F}$) are eliminated.

4.1.3. Solver and Boundary Conditions. The computational domain and applied boundary are denoted in Figure 8. One sidewall of the water tunnel and one-third of the rotor interfaces were hidden in Figure 8 to allow for the demonstration of components. The model was considered steady, incompressible, and was solved in ANSYS 18.2/Fluent. The solver type was set to a pressure-based coupled algorithm. This solver simultaneously solves the momentum equations (expressed using absolute velocity formulation) and the pressure-based continuity equation. The inlet was given a uniform velocity of 0.911 m/s, a turbulent intensity of 1%, and a turbulence length scale (l) of 0.00117348. The turbulence length scale was calculated using the imperial relation $l = 0.07 \times$ chord length. At the outlet, the relative pressure was set to zero, and the same inlet value of the turbulence length scale was assigned. The flow domains around the blades were set to the rotational frame of motion and were given the value of operational rotational speed, whereas the water tunnel domain was given a stationary frame of motion. Second-order up-winding discretization

schemes were selected for solving all the flow equations. Convergence criteria have been set such that the residuals for continuity equation, x-momentum, y-momentum, z-momentum, k, and ω were less than 10^{-4}.

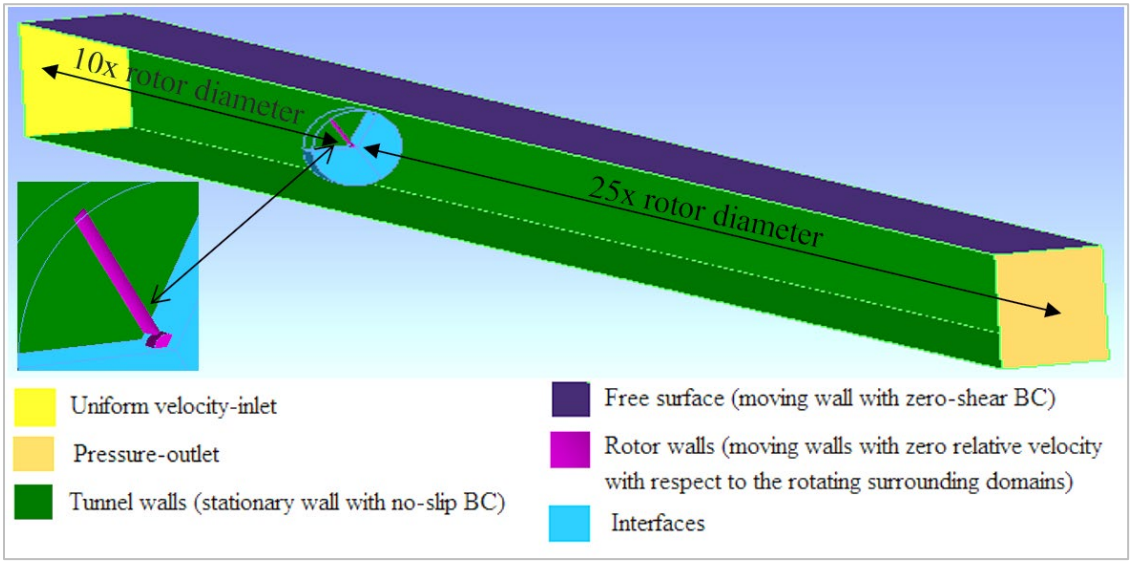

Figure 8. The water tunnel dimensions and boundary conditions (walls and free surface are hidden)

4.1.4. Experimental Validation. The results generated from CFD were validated before importing loads to the FEA model. The CFD input operational conditions are listed in Table 3. The listed values of RPM were within the range between the optimum rotational speed (210 RPM) in the water tunnel power experiment and the used rotational speed in the delamination investigation experiment (245 RPM). The predicted power coefficient (C_P), in Figure 9a, was in a good agreement with the experiment results. However, as shown in Figure 9b, the CFD model underestimated the thrust coefficient (C_T). The predicted C_T was noticed to deviated farther as TSR increased.

Table 3. CFD input operational conditions

Pitch angle (degree)	Velocity (m/s)	Rotational speed (RPM)
20	0.911	210
		235
		245

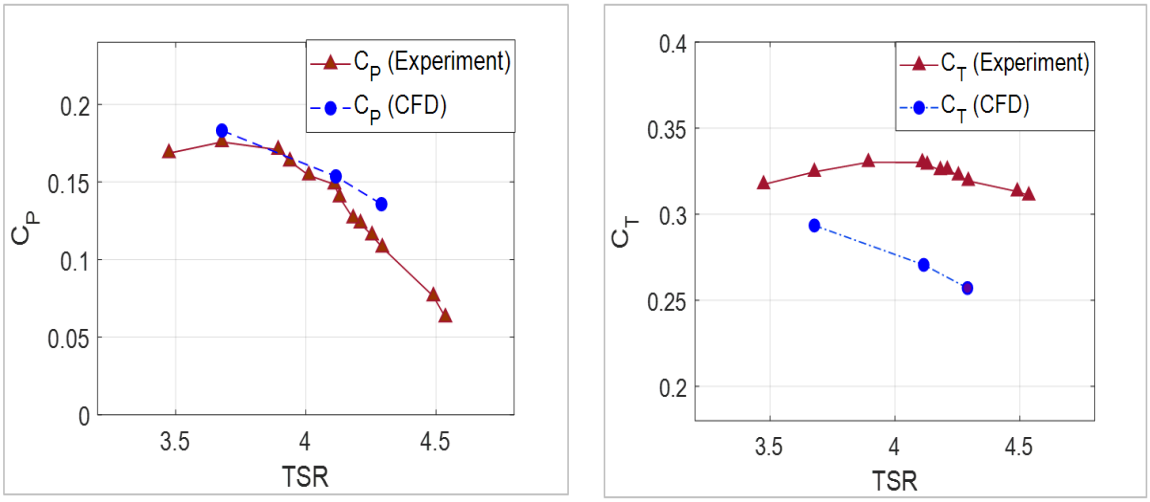

(a) (b)

Figure 9. Predicted (a) power coefficient and (b) thrust coefficient validated against the corresponding experimental measurements

4.2. FINITE ELEMENT ANALYSIS

The finite element method was used to analyze the blade structural response using the commercial software of ABAQUS/CAE 2018. The pressure loads obtained from the CFD model was imported to the finite element model. Figure 10a shows the pressure distribution on the blade surfaces using CFD. Figure 10b shows the same pressure loads

mapped onto the finite element model using ABAQUS/CAE 2018. More details about the geometry and model setup are discussed in this section.

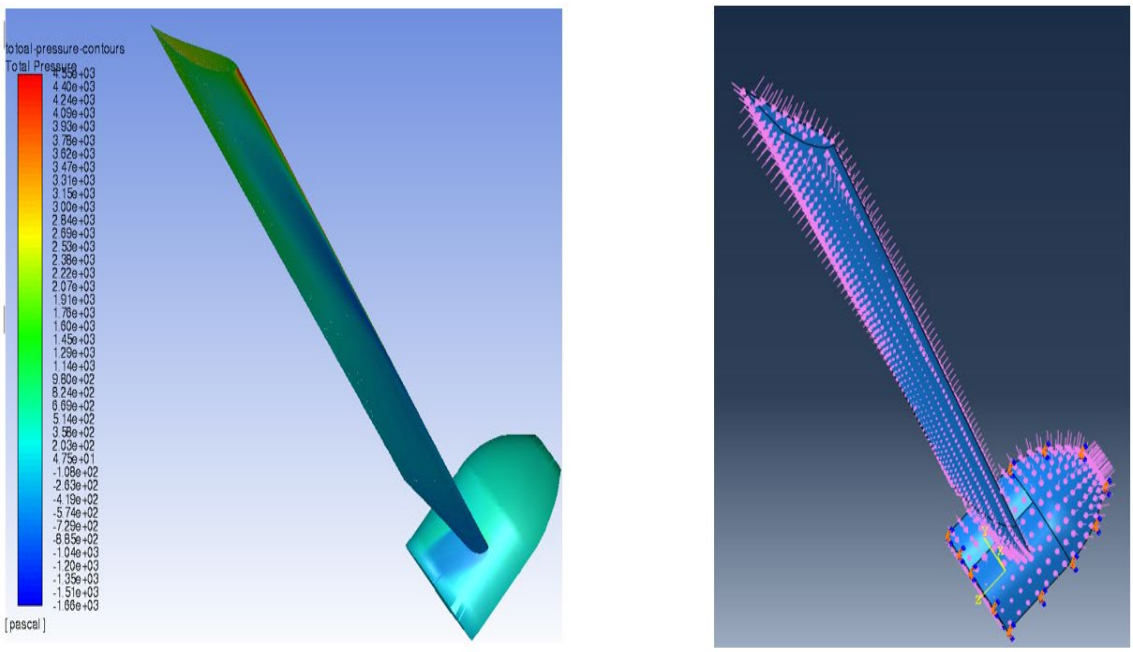

Figure 10. (a) Total pressure distribution obtained in ANSYS Fluent and (b) total pressure imported to ABAQUS/CAE 2018 using the analytical mapped fields

4.3. BLADE GEOMETRY

The blade used in the finite element simulation was similar to that used in both the experiment and the CFD simulation; however, the blade layers were individually modeled as solid bodies as shown in Figure 11. The Teflon sheets were represented inside the blade body by subtracting Teflon volume form the composite materials between the second and the third layers at the upper and the lower halves of the blade. These Teflon locations were similar to that in the fabricated and tested blades. The blade layers were modeled using

MATLAB and CAD software. The MATLAB code was developed to split the hydrofoils into upper and lower curves and then offset these curves by multiple of the layer thickness (0.3175 mm); thus, all layers curves are generated.

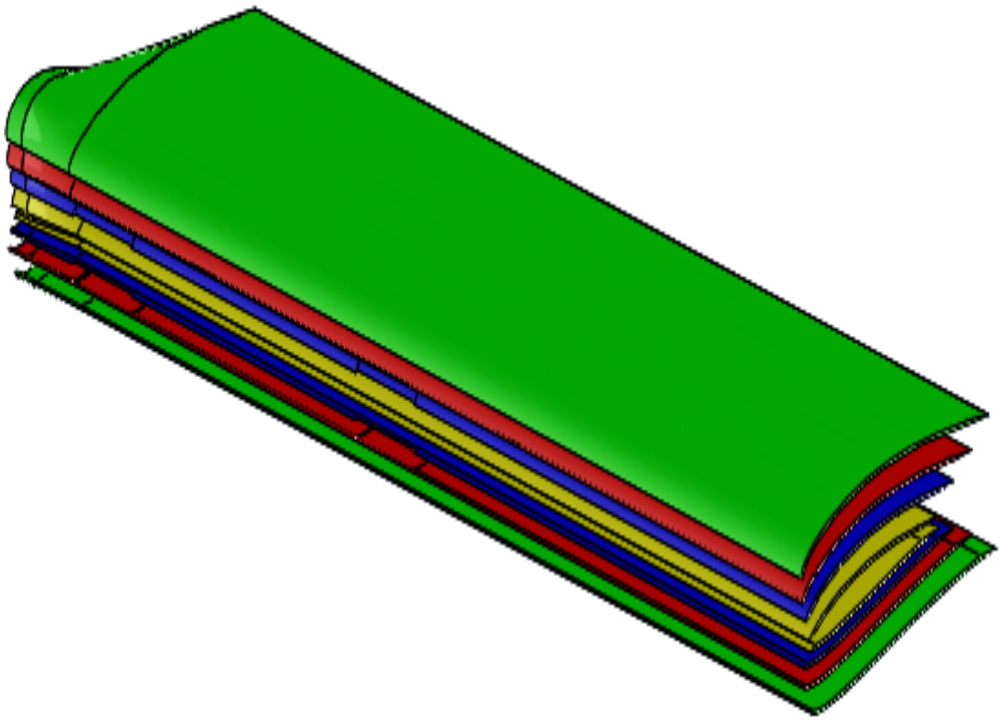

Figure 11. An illustration of the 8 CFRP laminates used to model the blade

5. RESULTS AND DISCUSSION

The samples were thermographically imaged after every million resolutions. The infrared images were analyzed to measure the area of delamination after each run. Figure 12 shows an example of the taken thermography images for all three layup orientations.

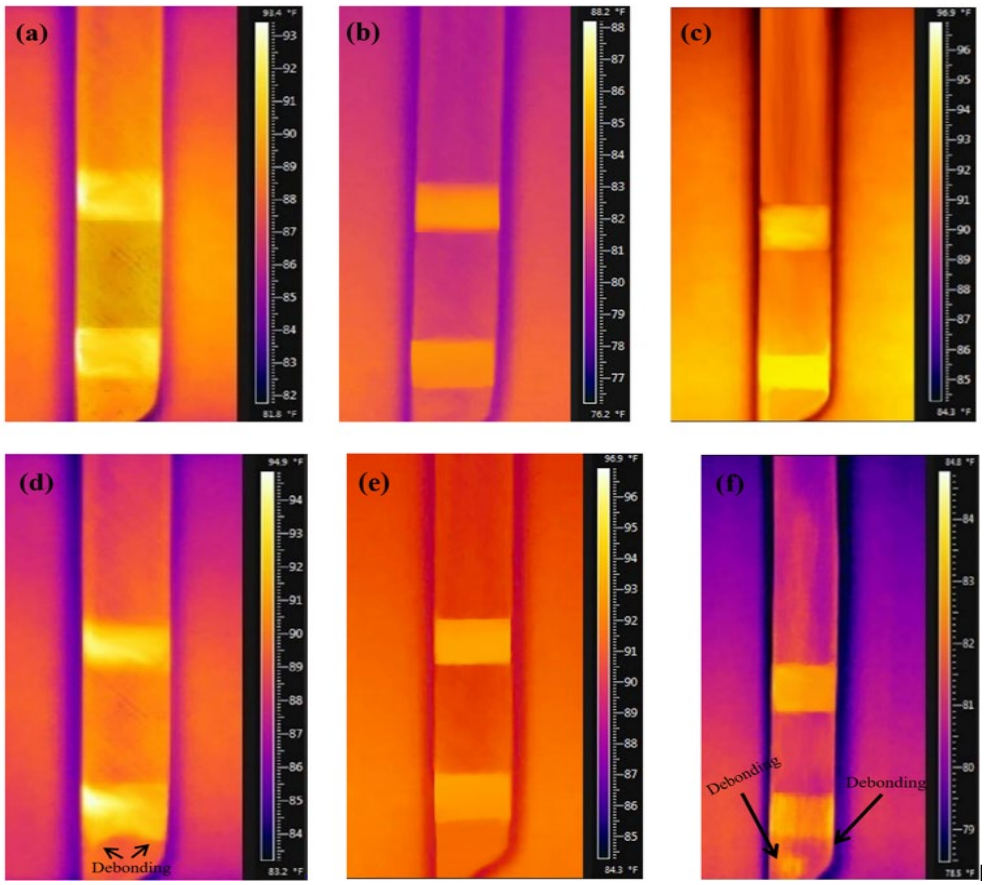

Figure 12. Thermography images of (a) $[45^o/-45^o]_S$ back side before operation, (b) $[0^o]_4$ back side before operation, (c) $[0^o/90^o]_S$ back side after operation, (d) $[45^o/-45^o]_S$ back side after 3M revolutions, (e) $[0^o]_4$ back side after 3M revolutions, and (f) $[0^o/90^o]_S$ back side after 3M revolutions

A MATLAB code was generated to process the images and pinpoint the pixels that are gradually changing in color from fully debonded layers to intact layers. Once the pixels were determined, ImageJ software (developed by NIH, Bethesda, MD) was used to measure the area based on the number of pixels and the size of each pixel. The images were converted into 8-bit to create a grayscale image before setting up the scale size and create a threshold that will generate a color contrast for each pixel or group of pixels that have the same intensity. A total of 24 images were analyzed. Table 4 shows the area of

delamination for each blade before the operation, after 1 million revolutions, 2 million revolutions, and 3 million revolutions. To reduce the noise, the pixels with a size less than 0.03 inch^2 (20 mm^2) were excluded, which will result in having only two highlighted areas in each image (middle and bottom debonding locations), as shown in figure 13.

Table 4. The area measurements of all blades

Laminate stacking sequence	Number of revolutions in millions	Middle Back (mm^2)	Middle Front (mm^2)	Bottom Back (mm^2)	Bottom Front (mm^2)
[0º/90º]	0	167.771	168.222	167.603	169.778
[0º/90º]	1	169.487	170.051	224.931	217.775
[0º/90º]	2	170.008	170.408	227.134	220.015
[0º/90º]	3	170.257	170.597	229.566	222.947
[0º]	0	169.431	168.055	170.727	168.215
[0º]	1	169.917	169.643	180.623	175.009
[0º]	2	170.099	169.882	181.913	176.184
[0º]	3	170.155	169.959	182.056	176.468
[45º/-45º]	0	167.915	168.123	170.845	167.991
[45º/-45º]	1	169.004	171.357	214.036	184.641
[45º/-45º]	2	169.399	172.701	217.451	188.041
[45º/-45º]	3	169.529	173.765	219.093	190.586

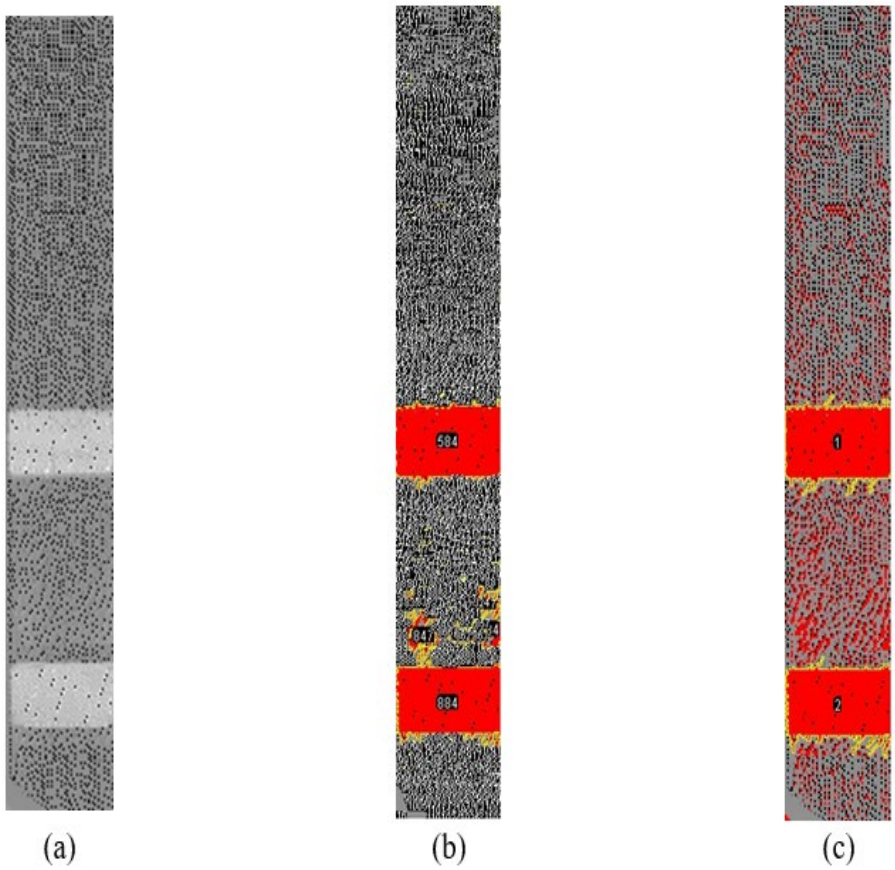

Figure 13. The process of eliminating the noise and calculating the area where(a) the image after being converted to 8-bit, (b) the image before creating a threshold and it shows 1026 readings, and (c) the final image after eliminating the noise and it shows only the two debonded areas

A finite element model was created using ABAQUS/CAE 2018 to visualize the stress distribution along the blade up to the point of failure. Figure 14 shows the exerted stresses on both sides of the $[0^o/90^o]_S$ blade. The backside showed a higher magnitude of stress compared to the front side, which supports the findings of this study.

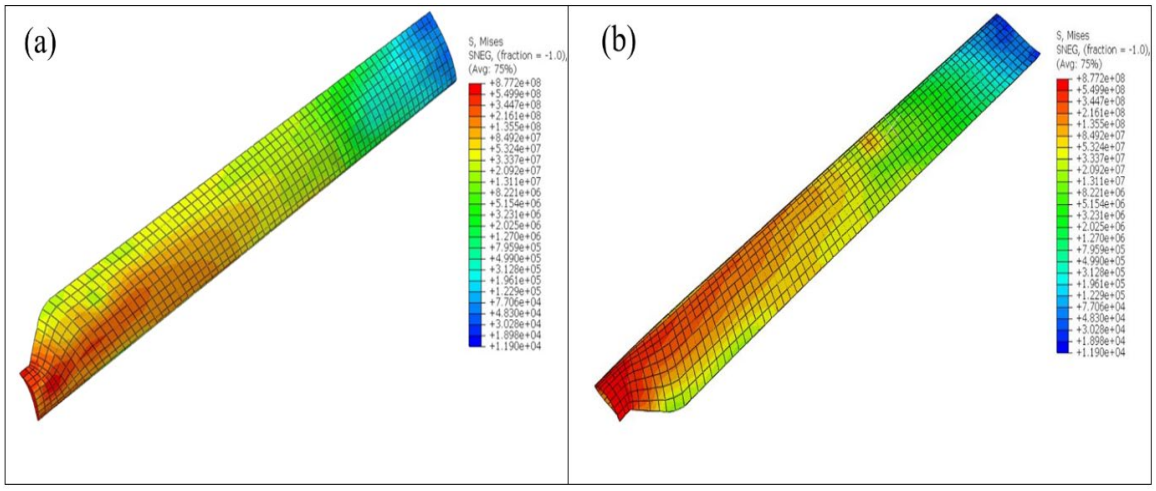

Figure 14. The von Mises stress distribution on (a) front side of the blade and (b) backside of the blade

The $[0^o]_4$ blades showed the least stresses resulted from the hydrodynamic loads. On the other hand, the $[0^o/90^o]_S$ showed the maximum stresses. Accordingly, the results from the thermography analysis showed significant debonding growth in the $[0^o/90^o]_S$ blade compared with the other two lay-up orientations. The least growth was noticed in the unidirectional blade ($[0^o]_4$). In addition, there was a direct relationship between the radial location of the damaged area and the rate of delamination growth. At the middle debonding location, all blades showed relatively very little delamination. On the other hand, the bottom location showed a clear delamination growth after each iteration. It was noticed that the backside had more delamination than the front side. This can be attributed to the fact that there are higher stresses near the root of the blade on the backside compared to the front side. Figures 15 and 16 showed the change in interlaminar debonding areas in the middle and the bottom of the blade, respectively.

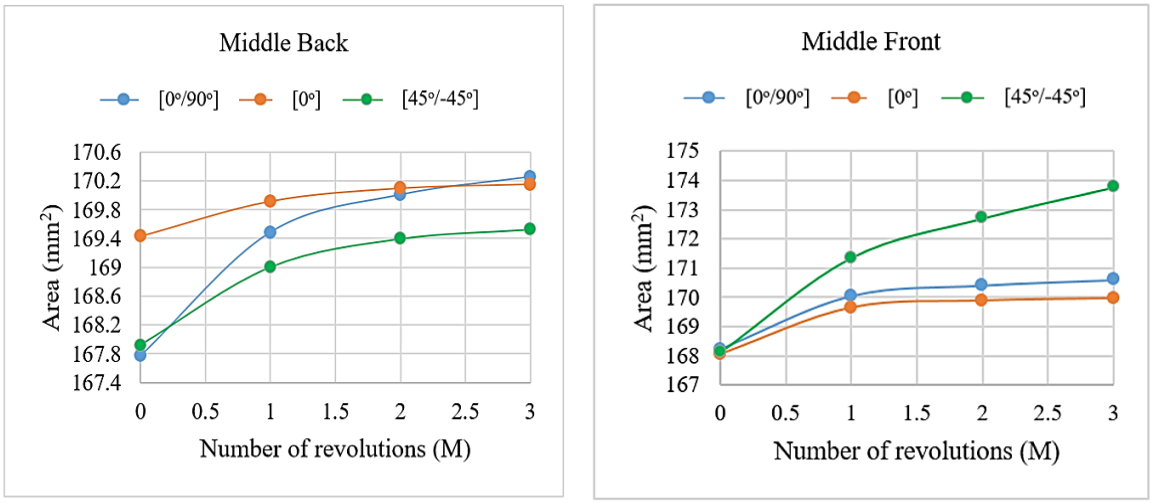

(a) (b)

Figure 15. The growth in the debonding area of the three laminate stacking sequences at (a) middle back, (b) a middle front

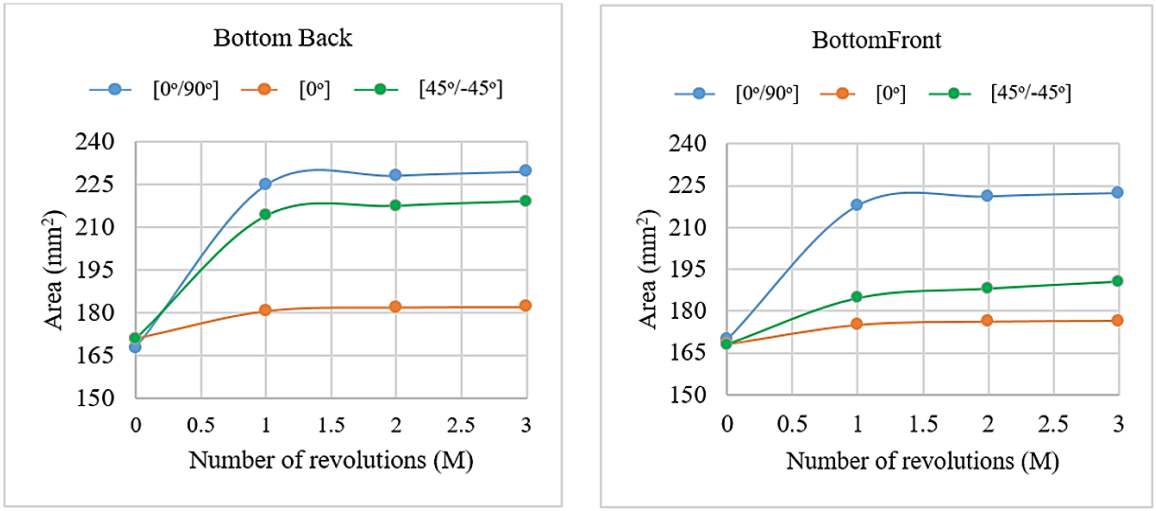

(a) (b)

Figure 16. The growth in the debonding area of the three laminate stacking sequences at (a) bottom back, (b) bottom front

The mismatch in the stiffness between the adjacent layers has directly contributed to the delamination growth. Since the axial stresses dominated the loading, therefore, the

$[0^o]_4$ blade has shown the best performance with the least propagation. The percentage of delamination growth at the bottom location of the backside after the first million revolution for the $[0^o]_4$, $[0^o/90^o]_S$, and $[45^o/-45^o]_S$ lay-ups were 5.79%, 34.2%, and 25.28% respectively. After two million revolutions, the percentage of growth dropped significantly to become 0.71%, 1.42%, and 1.59%, respectively. After three million revolutions, the debonding growth was 0.07%, 0.62%, and 0.75% respectively. The experiments ended after three million revolutions due to the stability of the blade to resist the interlaminar debonding growth.

6. CONCLUSION

Analysis and experiments on the interlaminar debonding growth with respect to the orientation of the laminate in a CFRP water turbine blade was presented. Unidirectional ($[0^o]_4$), cross-ply ($[0^o/90^o]_S$), and angle-ply ($[45^o/-45^o]_S$) laminate stacking sequences were selected for this study. CFRP composite blades were manufactured using the OOA technique. During the manufacturing process, two defects were introduced at two locations (middle and bottom of the blade). These defects were created on both sides of the blade (front and back). Infrared images were taken on four stages: (1) before placing in the water tunnel, (2) after running in water tunnel for one million revolutions, (3) after two million revolutions, and (4) after three million revolutions. A finite element model was created to predict the stress distribution on both sides of the blade. The bottom debonding location showed higher growth in delamination compared to the middle location. The observations obtained from this study are in complete agreement with the stress distribution analysis that showed the maximum stresses being located near the root of the blade. The

unidirectional laminates showed the least debonding growth compared to the other two angle-ply laminates. This higher resistance of interlaminar debonding growth was contributed to the fact that the direction of the load is parallel to the fibers in the unidirectional blade. In conclusion, the unidirectional blades are recommended when manufacturing CFRP composite blades for horizontal axis water turbines because of their higher stiffness and higher delamination resistance.

REFERENCES

[1] H. J. Vermaak, K. Kusakana, and S. P. Koko, "Status of micro-hydrokinetic river technology in rural applications: a review of literature," *Renewable and Sustainable Energy Reviews,* vol. 29, pp. 625-633, 2014.

[2] C. Gopal, M. Mohanraj, P. Chandramohan, and P. Chandrasekar, "Renewable energy source water pumping systems—A literature review," *Renewable and Sustainable Energy Reviews,* vol. 25, pp. 351-370, 2013.

[3] T. Sarver, A. Al-Qaraghuli, and L. L. Kazmerski, "A comprehensive review of the impact of dust on the use of solar energy: History, investigations, results, literature, and mitigation approaches," *Renewable and sustainable energy Reviews,* vol. 22, pp. 698-733, 2013.

[4] N. A. Kelly and T. L. Gibson, "Improved photovoltaic energy output for cloudy conditions with a solar tracking system," *Solar Energy,* vol. 83, no. 11, pp. 2092-2102, 2009.

[5] H. Akimoto, K. Tanaka, and K. Uzawa, "A conceptual study of floating axis water current turbine for low-cost energy capturing from river, tide and ocean currents," *Renewable energy,* vol. 57, pp. 283-288, 2013.

[6] I. S. Hwang, Y. H. Lee, and S. J. Kim, "Optimization of cycloidal water turbine and the performance improvement by individual blade control," *Applied Energy,* vol. 86, no. 9, pp. 1532-1540, 2009.

[7] M. Patel, K. Saurabh, V. B. Prasad, and J. Subrahmanyam, "High temperature C/C–SiC composite by liquid silicon infiltration: a literature review," *Bulletin of Materials Science,* vol. 35, no. 1, pp. 63-73, 2012.

[8] J. W. Schmidt, A. Bennitz, B. Täljsten, P. Goltermann, and H. Pedersen, "Mechanical anchorage of FRP tendons–a literature review," *Construction and Building Materials,* vol. 32, pp. 110-121, 2012.

[9] M. Gholami, A. R. M. Sam, J. M. Yatim, and M. M. Tahir, "A review on steel/CFRP strengthening systems focusing environmental performance," *Construction and Building Materials,* vol. 47, pp. 301-310, 2013.

[10] C. Baley, P. Davies, Y. Grohens, and G. Dolto, "Application of interlaminar tests to marine composites. A literature review," *Applied composite materials,* vol. 11, no. 2, pp. 99-126, 2004.

[11] C. S. Smith, *Design of marine structures in composite materials*. Elsevier London, 1990.

[12] I. M. Daniel, O. Ishai, I. M. Daniel, and I. Daniel, *Engineering mechanics of composite materials*. Oxford university press New York, 1994.

[13] B. D. Agarwal, L. J. Broutman, and K. Chandrashekhara, *Analysis and performance of fiber composites*. John Wiley & Sons, 2018.

[14] S. T. Lau, M. a. Said, and M. Y. Yaakob, "On the effect of geometrical designs and failure modes in composite axial crushing: a literature review," *Composite structures,* vol. 94, no. 3, pp. 803-812, 2012.

[15] F. M. Mohee, A. Al-Mayah, and A. Plumtree, "Anchors for CFRP plates: State-of-the-art review and future potential," *Composites Part B: engineering,* vol. 90, pp. 432-442, 2016.

[16] C. Laird and G. Smith, "Crack propagation in high stress fatigue," *Philosophical Magazine,* vol. 7, no. 77, pp. 847-857, 1962.

[17] D. Shu and Y.-W. Mai, "Effect of stitching on interlaminar delamination extension in composite laminates," *Composites Science and Technology,* vol. 49, no. 2, pp. 165-171, 1993.

[18] A. J. Russell and K. N. Street, "Moisture and temperature effects on the mixed-mode delamination fracture of unidirectional graphite/epoxy," in *Delamination and debonding of materials*: ASTM International, 1985.

[19] D. J. Elder, R. S. Thomson, M. Q. Nguyen, and M. L. Scott, "Review of delamination predictive methods for low speed impact of composite laminates," *Composite Structures,* vol. 66, no. 1-4, pp. 677-683, 2004.

[20] A. Garg and O. Ishai, "Hygrothermal influence on delamination behavior of graphite/epoxy laminates," *Engineering Fracture Mechanics,* vol. 22, no. 3, pp. 413-427, 1985.

[21] F. X. de Charentenay, J. M. Harry, Y. J. Prel, and M. L. Benzeggagh, "Characterizing the effect of delamination defect by mode I delamination test," in *Effects of defects in Composite Materials*: ASTM International, 1984.

[22] R. Olsson, J. Thesken, F. Brandt, N. Jönsson, and S. Nilsson, "Investigations of delamination criticality and the transferability of growth criteria," *Composite Structures,* vol. 36, no. 3-4, pp. 221-247, 1996.

[23] Z. Hashin, "Failure criteria for unidirectional fiber composites," *Journal of Applied Mechanics,* vol. 47, no. 2, pp. 329-334, 1980.

[24] J. Wiegand, N. Petrinic, and B. Elliott, "An algorithm for determination of the fracture angle for the three-dimensional Puck matrix failure criterion for UD composites," *Composites Science and Technology,* vol. 68, no. 12, pp. 2511-2517, 2008.

[25] R. Sadeghian, S. Gangireddy, B. Minaie, and K.-T. Hsiao, "Manufacturing carbon nanofibers toughened polyester/glass fiber composites using vacuum assisted resin transfer molding for enhancing the mode-I delamination resistance," *Composites Part A: applied science and manufacturing,* vol. 37, no. 10, pp. 1787-1795, 2006.

[26] D. Wilkins, J. Eisenmann, R. Camin, W. Margolis, and R. Benson, "Characterizing delamination growth in graphite-epoxy," in *Damage in Composite Materials: Basic Mechanisms, Accumulation, Tolerance, and Characterization*: ASTM International, 1982.

[27] K. Dransfield, C. Baillie, and Y.-W. Mai, "Improving the delamination resistance of CFRP by stitching—a review," *Composites Science and Technology,* vol. 50, no. 3, pp. 305-317, 1994.

[28] W. J. Cantwell and J. Morton, "The Impact Resistance of Composite Materials—a review," *Composites,* vol. 22, no. 5, pp. 347-362, 1991.

[29] E. Fuoss, P. V. Straznicky, and C. Poon, "Effects of stacking sequence on the impact resistance in composite laminates—Part 1: parametric study," *Composite Structures,* vol. 41, no. 1, pp. 67-77, 1998.

[30] S. Abrate, "Impact on laminated composite materials," *Applied Mechanics Reviews,* vol. 44, no. 4, pp. 155-190, 1991.

[31] H. Ho-Cheng and C. Dharan, "Delamination during drilling in composite laminates," *Journal of Engineering for Industry,* vol. 112, no. 3, pp. 236-239, 1990.

[32] M. S. Selig and J. J. Guglielmo, "High-lift low Reynolds number airfoil design," *Journal of Aircraft,* vol. 34, no. 1, pp. 72-79, 1997.

[33] M. Attaran, "The rise of 3-D printing: The advantages of additive manufacturing over traditional manufacturing," *Business Horizons,* vol. 60, no. 5, pp. 677-688, 2017.

[34] J. Kratz, K. Hsiao, G. Fernlund, and P. Hubert, "Thermal models for MTM45-1 and Cycom 5320 out-of-autoclave prepreg resins," *Journal of Composite Materials,* vol. 47, no. 3, pp. 341-352, 2013.

[35] S. Anandan, G. Dhaliwal, S. Ganguly, and K. Chandrashekhara, "Investigation of sandwich composite failure under three-point bending: Simulation and experimental validation," *Journal of Sandwich Structures & Materials,* 2018.

[36] S. Anandan, G. Dhaliwal, Z. Huo, K. Chandrashekhara, N. Apetre, and N. Iyyer, "Curing of thick thermoset composite laminates: multiphysics modeling and experiments," *Applied Composite Materials,* vol. 25, no. 5, pp. 1155-1168, 2018.

[37] W. Minkina and S. Dudzik, *Infrared thermography: errors and uncertainties*. John Wiley & Sons, 2009.

[38] O. Breitenstein, W. Warta, M. C. Schubert, and M. Langenkamp, *Lock-in thermography: Basics and use for evaluating electronic devices and materials*. Springer, 2018.

[39] Y. Bazilevs, M. C. Hsu, J. Kiendl, and D. Benson, "A computational procedure for prebending of wind turbine blades," *International Journal for Numerical Methods in Engineering,* vol. 89, no. 3, pp. 323-336, 2012.

[40] F. R. Menter, "Two-equation eddy-viscosity turbulence models for engineering applications," *AIAA journal,* vol. 32, no. 8, pp. 1598-1605, 1994.

[41] N. Kolekar and A. Banerjee, "A coupled hydro-structural design optimization for hydrokinetic turbines," *Journal of Renewable and Sustainable Energy,* vol. 5, no. 5, p. 053146, 2013.

[42] M. Rahimian, J. Walker, and I. Penesis, "Performance of a horizontal axis marine current turbine–A comprehensive evaluation using experimental, numerical, and theoretical approaches," *Energy,* vol. 148, pp. 965-976, 2018.

[43] T. Javaherchi, S. Antheaume, and A. Aliseda, "Hierarchical methodology for the numerical simulation of the flow field around and in the wake of horizontal axis wind turbines: Rotating reference frame, blade element method and actuator disk model," *Wind Engineering,* vol. 38, no. 2, pp. 181-202, 2014.

III. IMPACT PERFORMANCE OF SANDWICH COMPOSITES WITH ADDITIVELY MANUFACTURED MODIFIED HONEYCOMB CORE

Mokhtar Fal, Okanmisope Fashanu, Robert Meinders, and K. Chandrashekhara*

Department of Mechanical and Aerospace Engineering

Missouri University of Science and Technology, Rolla, MO 65409

ABSTRACT

Due to its high strength to weight ratio, sandwich structures have become very popular in recent years. However, these structures are plagued with a weak core-to-facesheet bond strength. In this work, the effect of increasing the contact area between the composite facesheet and honeycomb core was studied. Sandwich panels were manufactured using two different honeycomb structures, a regular and a modified honeycomb, and their respective bond strengths were evaluated using the flatwise tension test. The modified honeycomb was designed to have a larger surface area while retaining the same relative density as the regular honeycomb. A finite element model was created to study the integrity of the sandwich structures subjected to localized impact damage. In order to validate the model, impact specimens were manufactured and tested for impact resistance. The facesheets were made out of carbon-fiber, while the core was additively manufactured using 304L stainless steel powder. The finite element model of the damage resistance due to impact showed a good agreement with the experimental results. Samples with increased contact area showed higher impact resistance. The average impact strength of the modified samples was 41.3% higher than the average impact strength of the regular

samples. Flatwise tension results showed that by increasing the contact area between the core and the facesheet the core-to-facesheet bond strength increased.

1. INTRODUCTION

Fiber-reinforced composite materials are made of high strength fibers, which are bonded to a matrix [1]. The fibers' contribution can be condensed down to load carrying, while the matrix is the member that holds the fibers together [2]. Sandwich structures incorporate a core that is sandwiched between two facesheets made from stiff materials [3]. Sandwich structures use a light weight core material to increase the thickness of the composite panels which increases the bending stiffness of the composite panels by increasing the bending moment [4]. Sandwich structures can also be flat or curved, as shown in Figure 1.

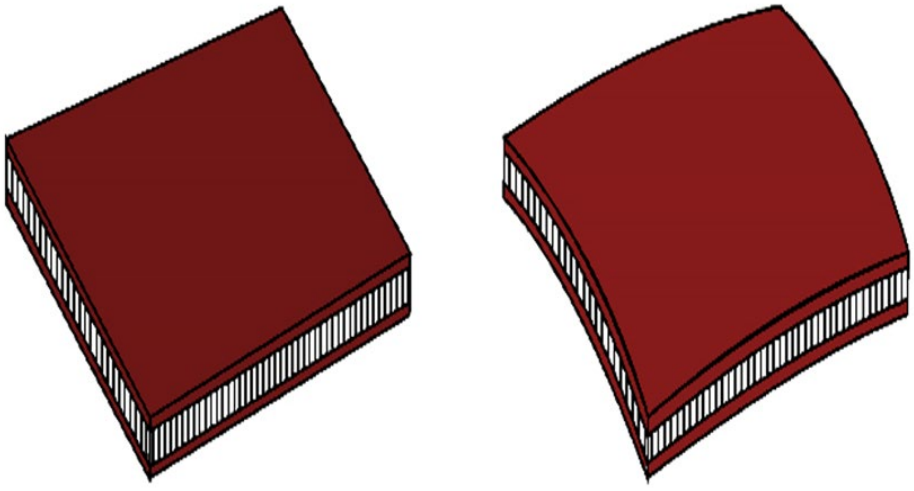

(a) (b)

Figure 1. (a) Flat sandwich structure and (b) curved sandwich structure

These facesheets support the structure against bending loads, while the core transfers shear force between the faces in a sandwich panel under load [5, 6]. The main reason for seeking to use honeycomb sandwich structures lies in their high stiffness to weight ratio. They can be light in weight and yet withstand relatively high loads. This property makes them preferable for applications where weight reduction is important. The configuration of the core differs based on the application. The honeycomb shape is a common core configuration in sandwich structures. Paik et al. [7] go as far as claiming that this configuration is the most popular one when constructing sandwich structures.

Due to its lightweight and reduced stiffness, the core is normally the weakest part of sandwich composites [8]. Although sandwich structures are desirable in a wide range of applications, they only see limited use in some applications such as large aircraft structures. This is due to their relatively poor resistance to localized impact loading from dropped tools to hail to debris encountered during operation [9]. Studies have been done to improve the performance of the sandwich structures. Leijten et al. [10] experimentally investigated the impact behavior of sandwich structures in aircraft. The aim was to reduce facing thickness and add an additional layer of fabric to improve the performance of the structure. However, it was concluded that both reducing the thickness of the facesheet and putting an additional layer of fabric did not have any significant impact on the performance.

For marine applications, Zenkert et al. [11] studied three localized damage cases on carbon fiber-reinforced polymer (CFRP) sandwich structures. It was found that any impact will significantly reduce the load-carrying capacity of the composite facesheet; however, the damage caused by localized transfer loads, which causes indentation on the composite facesheets, was found to less significant. Nevertheless, the accumulation of the onset of the

residual dent was found to causing an extreme loss of stiffness of the sandwich structure. Hull and Edgren [12] investigated the buckling, which resulted from low-velocity impacts in order to predict the residual strength of CFRP sandwich structures. Both thick and thin facesheet sandwich structure configurations were considered in the analytical study. The developed model was not able to predict the difference in residual strength between the thick and the thin laminates. These studies, along many other studies, may not have found the ultimate solution for all challenges that face sandwich structures; however, they are essential in understanding the behavior of sandwich structures under localized loads such as impacts. This work is focused on enhancing the performance of the honeycomb sandwich structure by increasing the contact area between the facesheet and the core while maintaining the weight of the whole sandwich structure.

2. MATERIALS

2.1. FACESHEETS

The facesheets of the sandwich panels were manufacture using IM7/Cycom 5320-1 carbon/epoxy prepreg by Cytec Engineering Materials Inc. This prepreg system is distinguished by its suitability to the out-of-autoclave (OOA) manufacturing process. The material properties of the IM7/Cycom 5320-1 prepreg system are shown in Table 1 [13].

Table 1. Material properties of IM7/Cycom 5320-1 carbon/epoxy prepreg

Property	Symbol	Value
Longitudinal tensile modulus	E_{11}	$156x10^9$ Pa
Transverse tensile modulus	E_{22}	$9.3x10^9$ Pa
Longitudinal Poisson's ratio	ν_{12}	0.3

Table 1. Material properties of IM7/Cycom 5320-1 carbon/epoxy prepreg (cont.)

Property	Symbol	Value
In-plane shear modulus	G_{12}	$5.5x10^9$ Pa
Transverse shear moduli	G_{13}, G_{23}	$5.5x10^9$ Pa
Longitudinal tensile strength	X^T	$2.503x10^9$ Pa
Longitudinal compressive strength	X^C	$2.078x10^9$ Pa
Transverse tensile strength	Y^T	$75.9x10^7$ Pa
Transverse Compressive strength	Y^C	$165x10^6$ Pa
Longitudinal shear strength	S^L	$73x10^6$ Pa
Transverse shear strength	S^T	$73x10^6$ Pa

Damage evolution fracture energy constants for IM7/Cycom 5320-1 carbon/epoxy prepreg laminate were taken from literature, and they are shown in Table 2 [14]. To improve the accuracy of the calculations, viscosity coefficients for longitudinal tensile strength, longitudinal compressive strength, transverse tensile strength, and transverse compressive strength were assumed to be 1×10^{-4} [15, 16].

Table 2. Damage evolution fracture energy constants of the IM7/Cycom 5320-1

Property	Symbol	Value
Longitudinal tensile fracture energy	F^{LT}	81.5×10^3 J/m^2
Longitudinal compressive fracture energy	F^{LC}	106.5×10^3 J/m^2
Transverse tensile fracture energy	F^{TT}	0.277×10^3 J/m^2
Transverse compressive fracture energy	F^{TC}	5.62×10^3 J/m^2

2.2. THE CORE

Argon gas atomized 304L stainless steel powder was used as the feed material for the core during this study. The size of the powder particles ranged between 15 µm to 63 µm. When 304L stainless steel is utilized in the selective laser melting (SLM) manufacturing process, it minimizes the need for solution annealing, due to its low carbon content [17].

3. MANUFACTURING AND ASSEMBLY

Two different honeycomb core configurations were manufactured. The first configuration was a normal hexagon shape honeycomb, as shown in Figure 2. For the sake of simplicity, this configuration will be called “regular.”

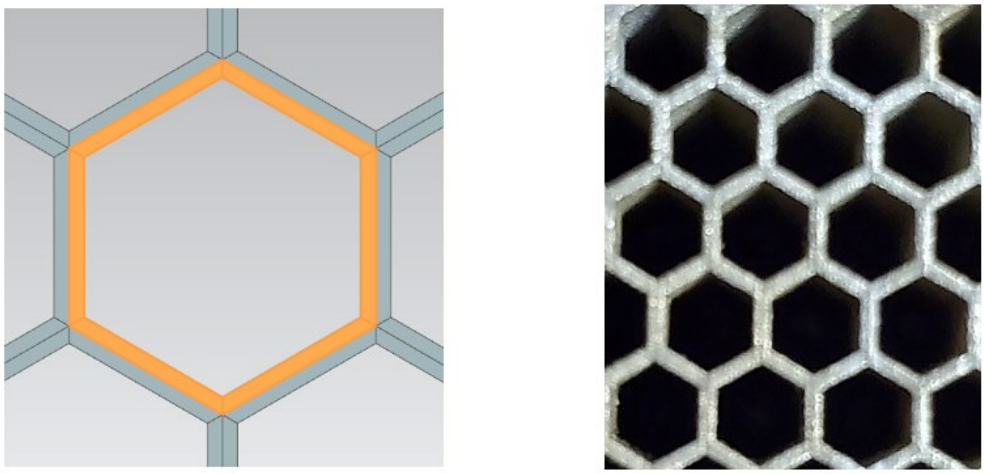

(a) (b)

Figure 2. (a) The designed configuration of the regular honeycomb core and (b) the additively manufactured regular honeycomb core

The second configuration is a hexagon honeycomb core with 238% more surface area at the top and bottom faces. This configuration will be referred to as the “modified”

honeycomb core. The modified honeycomb core is illustrated in Figure 3. In order to maintain the same weight for both configurations, the size of the walls for the modified honeycomb core was minimized from 0.15 mm (regular core) to 0.137 mm. This step was necessary to compensate for the increase in surface area. Both configurations had a height of 20 mm.

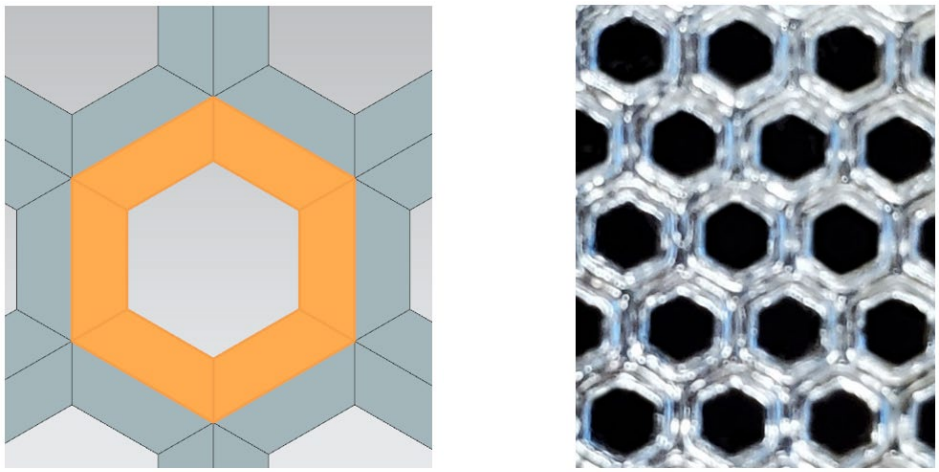

(a) (b)

Figure 3. (a) The designed configuration of the modified honeycomb core and (b) the additively manufactured modified honeycomb core

A Renishaw AM250SLM machine was used to manufacture the honeycomb samples by selective laser melting of the 304L stainless steel powder. The samples were cut into 50.8 mm X 50.8 mm X 20 mm. Each sample was weighed on an LBK12a Adam Weighing Scale with an accuracy of 0.45 gram (0.001 lb). The samples were found to be 88 grams (0.194 lb) with a 0.51% error. This corresponds to an area density of 34.1 kg/m^2.

The out-of-autoclave process was utilized to complete the fabrication of the facesheets. IM7/Cycom 5320-1 carbon/epoxy prepreg was selected to manufacture the

facesheets. The thickness of each sandwich facesheet was 1.27 mm. Afterward, the SLM 304L stainless steel honeycomb cores and the composite facesheets were bonded using MTA241/PK13 adhesive system, manufactured by ACG. MTA241/PK13 has a nominal density of 29 g/cm^2. The out-of-autoclave process was used to ensure a better bond between the facesheet and the core, as shown in Figure 4.

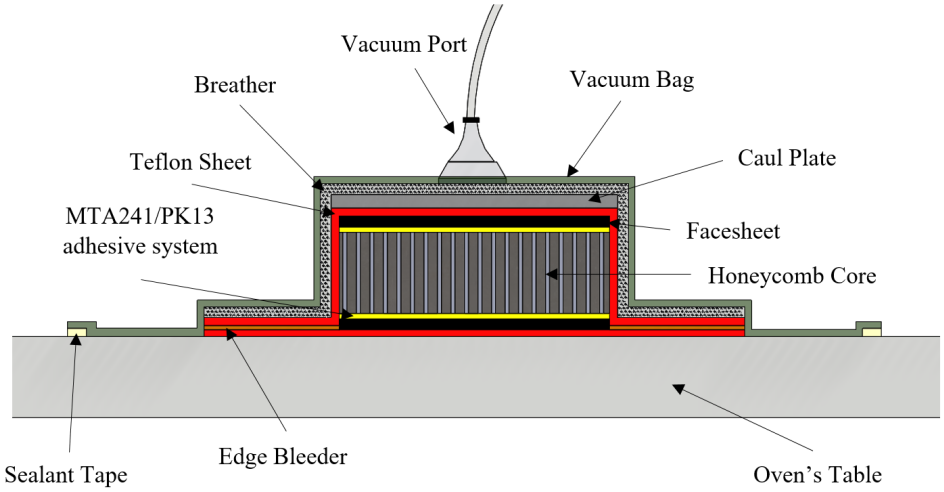

Figure 4. Out-of-autoclave process bagging assembly

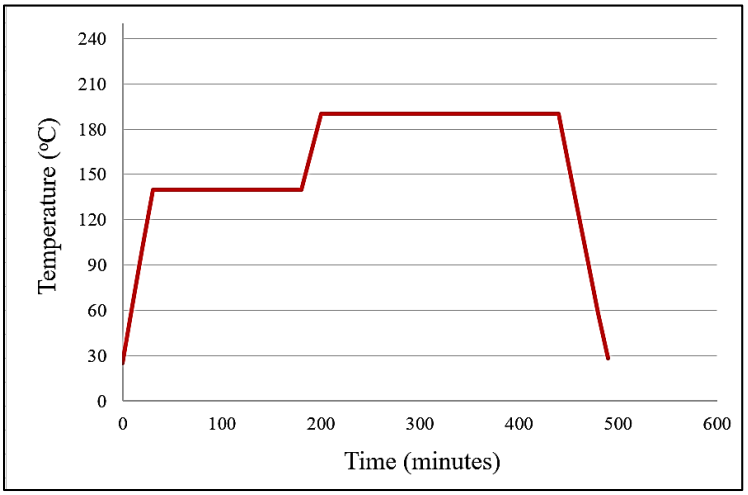

Figure 5. Manufacturer recommended cure cycle

4. EXPERIMENTS

4.1. IMPACT TEST

Instron Dynatup 9250 HV shock drop tower was utilized to carry out all impact tests, as shown in Figure 6. This machine is a gravity/spring falling weight type of tower, with the ability to electronically control the free-fall height, impact energy, or impact velocity. It has the capability of impacting samples at energies of up to 1603 J/m. It provides a high-speed precision data collection (up to 5 MHz). In this study, all samples were impacted with a 6.435 kg drop weight. The drop height was 0.0958 m for all samples to generate a 1 J/mm impact. Samples were secured during the impact tests by the mean of two clamping plates. The samples were impacted with a 12.7 mm diameter impactor pin with a rounded tip. Impulse software was used to display and store the impact data. The standard practice for damage resistance testing of sandwich constructions (ASTM D7766/D7766M-16) [18] was followed during the experiment preparation process.

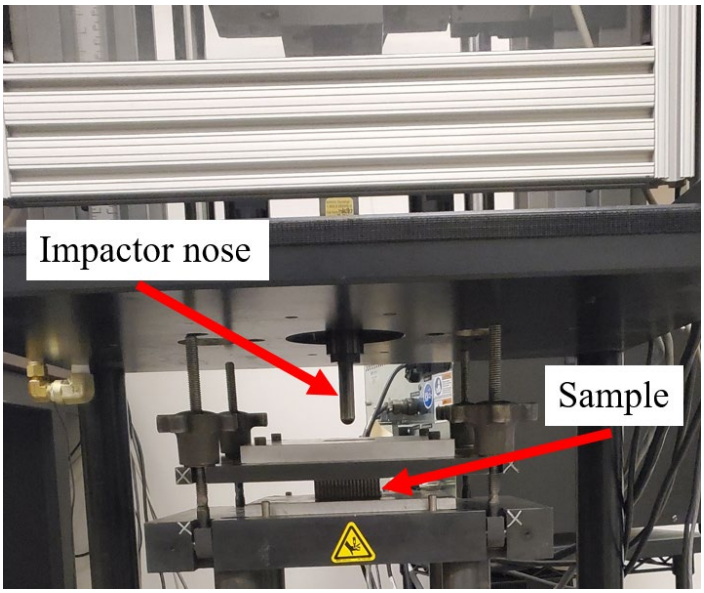

Figure 6. The impact test setup

Both Configurations, modified and regular, were tested for energy absorption. Samples were prepared to be 50.8 mm X 50.8 mm with a facesheet thickness of 1.27 mm. The height of the core was 20 mm, which makes the height of the whole sandwich structure from panel to panel is 23.1 mm ± 0.73 mm, including the adhesive layers between the facesheet and the core.

4.2. FLATWISE TENSION TEST

Flatwise tension testing was performed on the regular and modified samples using Instron 5985 test frame with a 250 kN load cell. Testing was based on ASTM C297-Standard Test Method for Flatwise Tensile Strength of Sandwich Constructions [19]. Aluminum loading blocks were attached to 50.8 mm x 50.8 mm samples using the MTA241/PK13 adhesive system. Samples were tested at ambient conditions with a 0.50 mm/min loading rate. Three samples were tested for each honeycomb core.

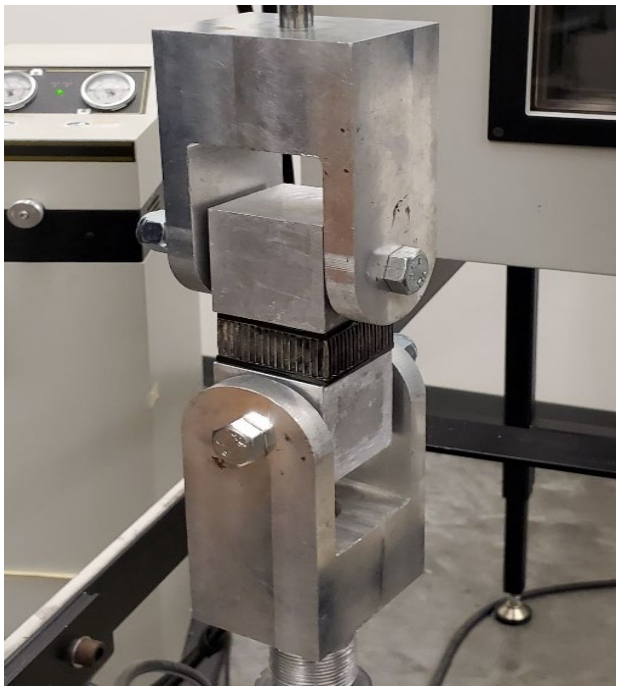

Figure 7. The setup of the flatwise tension test

4.3. FINITE ELEMENT ANALYSIS OF IMPACT

ABAQUS/CAE Software was used to develop a model of the two sandwich core composite structures for this study. Material properties were assigned using literature properties from section 2. The simulation was carried out using dynamic/explicit solver with a step time of 10×10^{-3} seconds. For the adhesive layers between the facesheet and the honeycomb core, a cohesive material behavior was created with a mixed-mode damage evolution. The impactor was modeled as a discrete rigid body with a diameter of 12.7 mm and a mass of 6.435 kg. Four plies were modeled to represent a single facesheet, with each ply having a thickness of 0.3175 mm. The facesheets were modeled using a continuum shell. The laminate stacking sequence of $[45^o/0^o/\text{-}45^o/90^o]_S$ was created for the composite layup orientation. A general contact (explicit) was selected to represent the interaction between the sandwich structure and the impactor. A tangential behavior with penalty friction formulation and friction coefficient of 0.3 was created as an interaction between the CFRP laminates. The impact panel was pinned from four sides ($U_1=U_2=U_3=0$) and ENCASTRE of the edges of the bottom face ($U_1=U_2=U_3=UR_1=UR_2=UR_3=0$), as shown in Figure 8. Where U_1, U_2, U_3, UR_1, UR_2, and UR_3 are the displacement in the x-direction, displacement in the y-direction, displacement in the z-direction, rotation along the x-axis, rotation along the y-axis, and rotation along the z-axis, respectively.

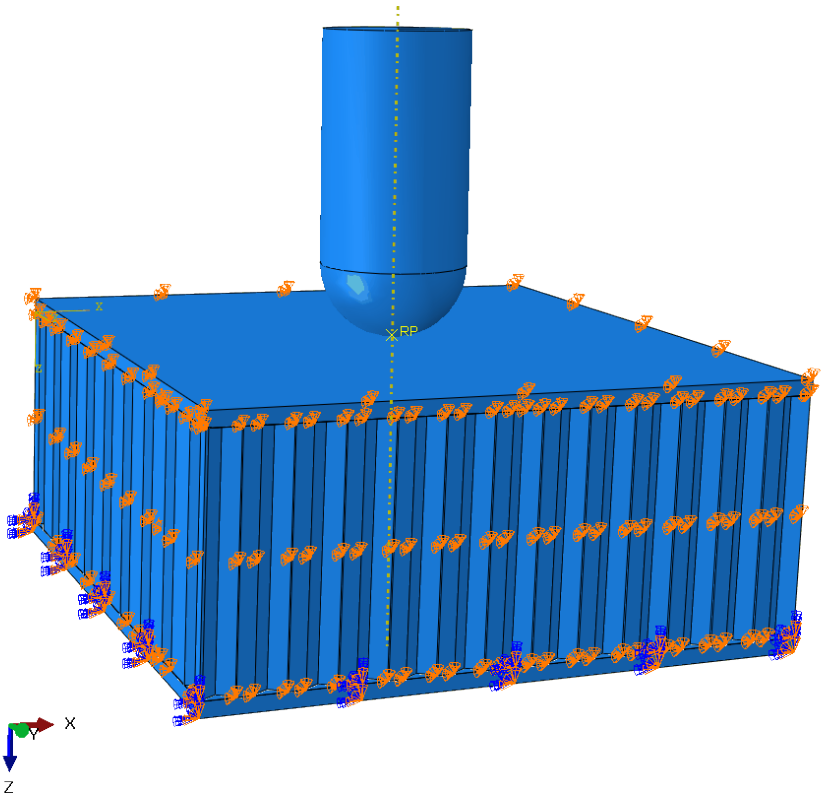

Figure 8. The boundary conditions of the modeled sandwich structure

A reference point was created at the tip of the impactor, and it was given a velocity of 1.37 m/sec. All components were meshed individually using ABAQUS/CAE meshing tool, and the technique selected during the meshing process was sweep with a quad-dominated element shape. Figure 9 shows the meshed assembly. The mesh size was verified using the built-in mesh verification tool in ABAQUS/CAE, and the worst aspect ratio was 1. This step was very important as it guaranteed that there would be no excessive element distortion during the simulation.

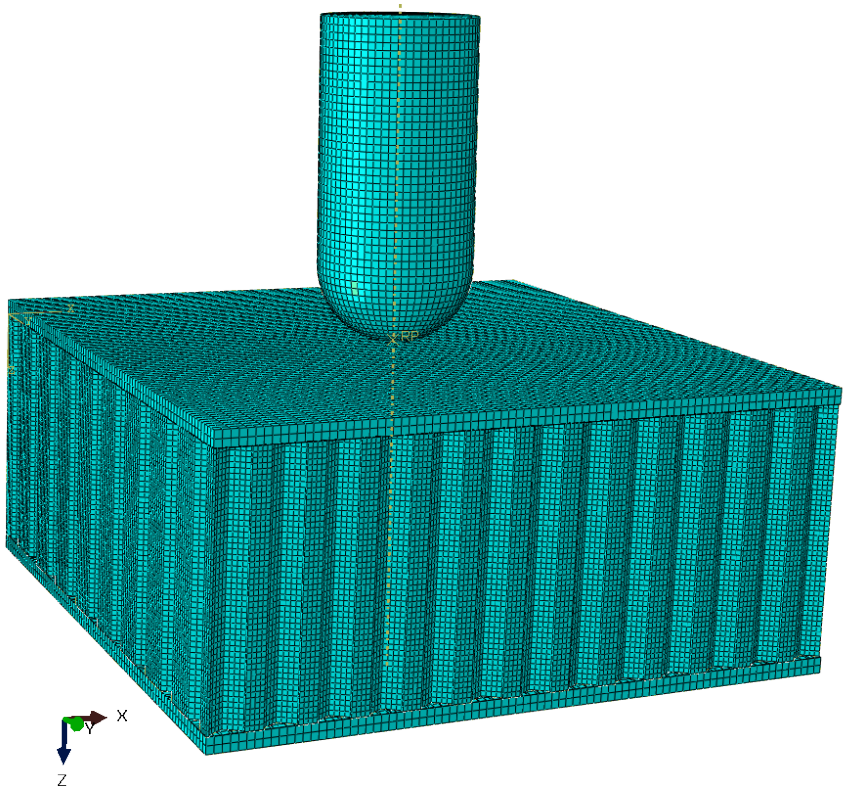

Figure 9. The meshed components using ABAQUS/CAE meshing tool

5. RESULTS AND DISCUSSION

5.1. IMPACT RESULTS

Impact testing of the honeycomb sandwich panels showed an improvement in the damage resistance when using the modified core structure. Both samples withstood a 6 J impact and suffered some surface denting. Analysis of the data shows that the modified structure absorbed an average of 4.22 J of energy, and the regular structure absorbed 4.73 J. The modified core average resting energy was 1.798 J, while the regular honeycomb core average resting energy was 1.277J. This is an improvement of 38% over the traditional honeycomb. The modified structure was also able to withstand more force before the

damage. The modified sandwich core generated average peak loads of 10.23 kN versus the regular core's 8.47 kN, an improvement of 20%. The modified samples also generated less deviation for the test. Tables 4 and 5 show the results obtained from the impact tests for the modified and the regular sandwich structures, respectively.

Table 4: Modified sandwich impact results

Sample	Max Force (kN)	Peak Energy (J)	Absorbed Energy (J)	Resting Energy (J)
1	10.115	5.999	4.179	1.820
2	10.311	6.049	4.292	1.756
3	10.276	6.022	4.204	1.818
Average	10.234	6.023	4.225	1.798
Standard Deviation	0.104	0.024	0.059	0.036

Table 5: Regular sandwich impact results

Sample	Max Force (kN)	Peak Energy (J)	Absorbed Energy (J)	Resting Energy (J)
1	8.989	6.012	4.579	1.433
2	8.298	6.019	4.816	1.203
3	8.135	5.985	4.789	1.196
Average	8.474	6.005	4.728	1.277
Standard Deviation	0.453	0.017	0.129	0.134

The plots of force versus time show more deviation in loading for the regular honeycomb core. This deviation during loading can be attributed to the destruction of the composite facesheet.

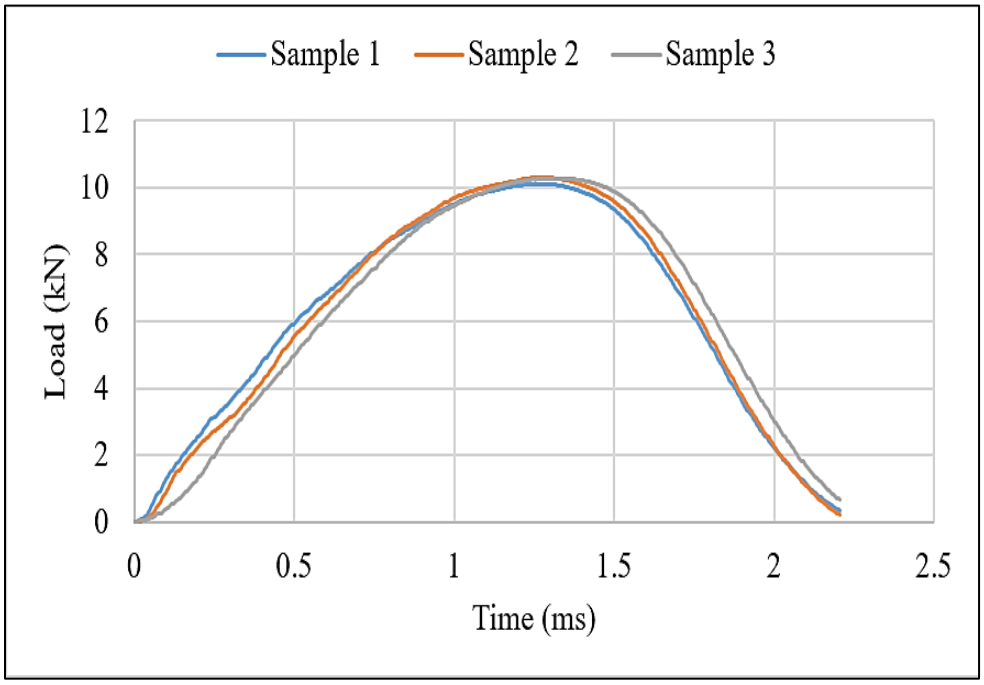

Figure 10. Impact load of modified honeycomb cores

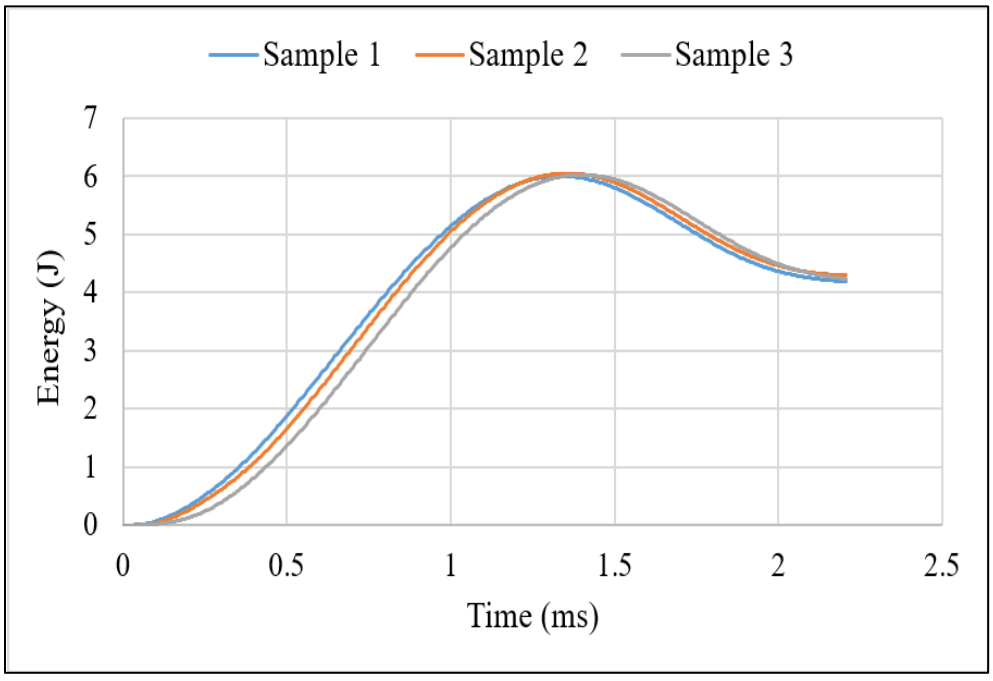

Figure 11. Impact energy of modified honeycomb cores

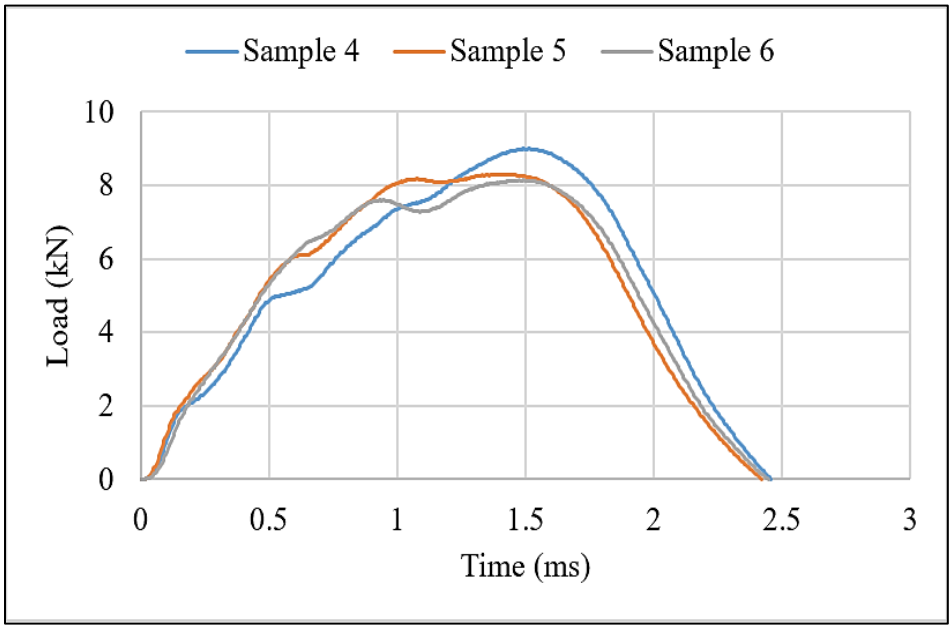

Figure 12. Impact load of regular honeycomb cores

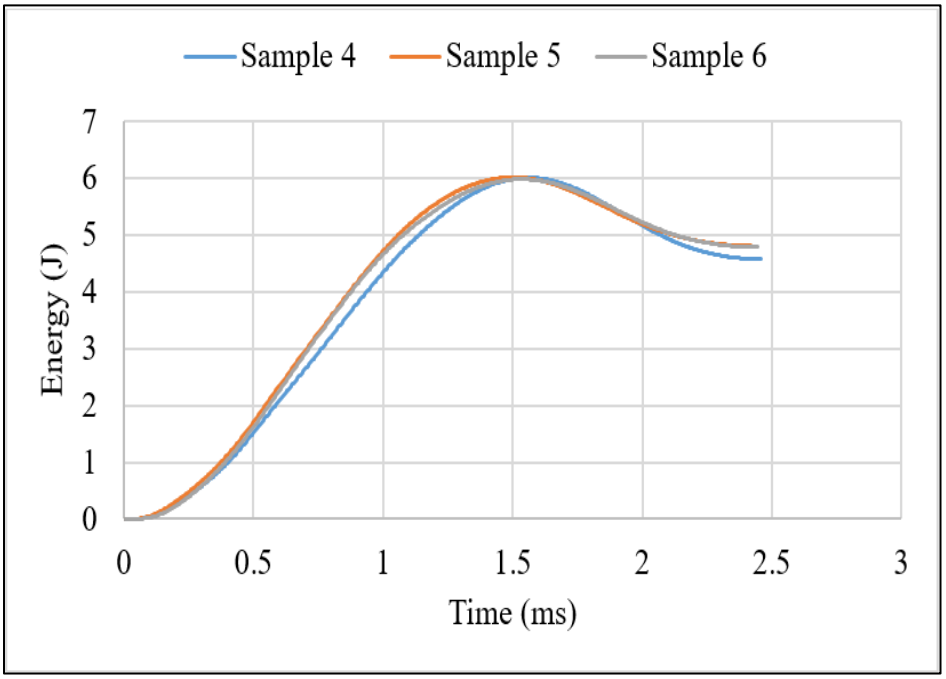

Figure 13. Impact energy of modified honeycomb cores

5.2. FLATWISE TENSION RESULTS

Flatwise tension testing showed an increase in the face bonding strength with the increase in the contact area between the core and the face sheets. The tested samples all exhibited adhesive failure of the core-facing adhesive. For the conducted tests, the strength of the adhesive was the critical failure in the composite design. The ability to increase the bonding area through the use of a modified core leads to a 70% increase in tensile strength for the sandwich structures.

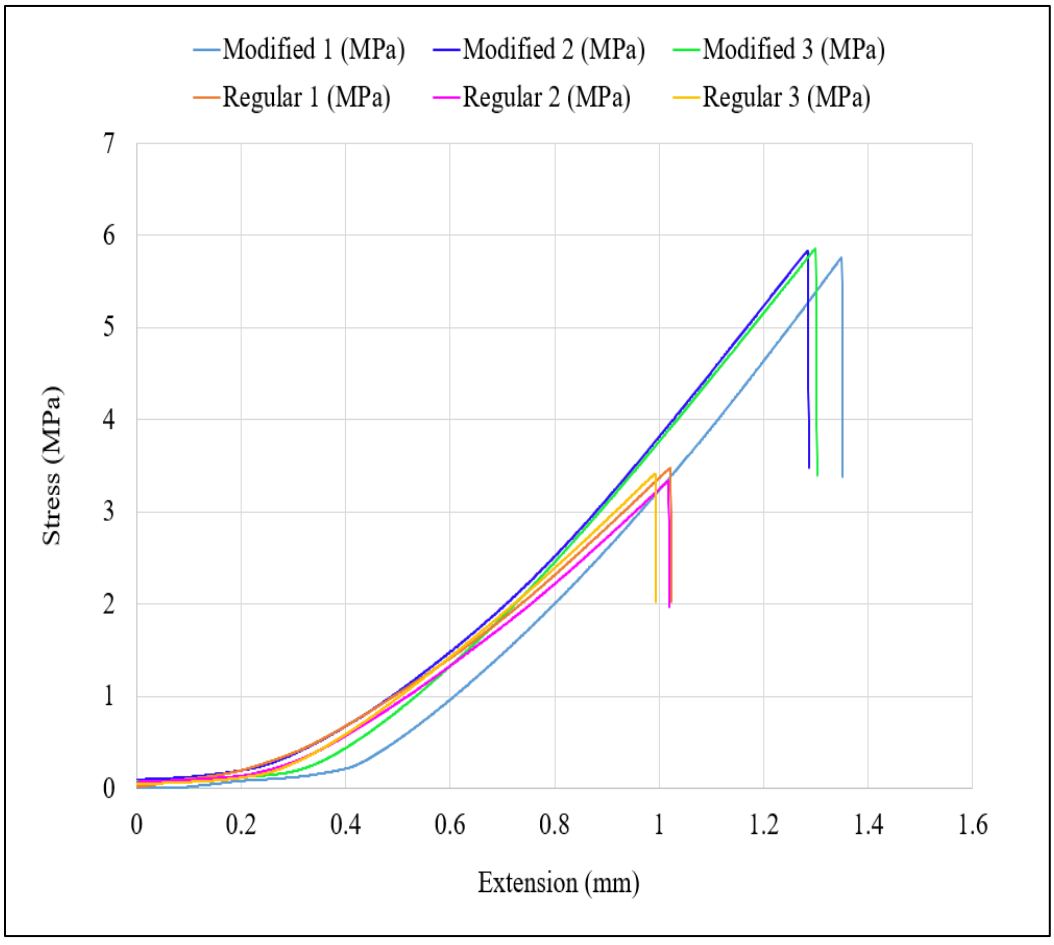

Figure 14. The flatwise tensile strength of all samples

Table 6: Flatwise tension maximum load

Sample	Regular (kN)	Modified (kN)
1	11.02	15.20
2	9.90	15.35
3	11.25	14.01
Average	10.72	14.85
Standard Deviation	0.72	0.73

Table 7: Ultimate flatwise tension strength

Sample	Regular (MPa)	Modified (MPa)
1	3.476	5.863
2	3.333	5.832
3	3.413	5.760
Average	3.407	5.818
Standard Deviation	0.072	0.053

5.3. FINITE ELEMENT ANALYSIS RESULTS

The results obtained from the finite element model showed a higher damage resistance in the modified honeycomb core sandwich structure compared with the regular one. The maximum force for the modified core was 10.43 kN, as shown in Figure 15. Whereas the maximum force for the regular honeycomb core was 7.38 kN, as illustrated in Figure 16. Thus, the modified core has increased the impact resistance for the whole structure by 41.3%.

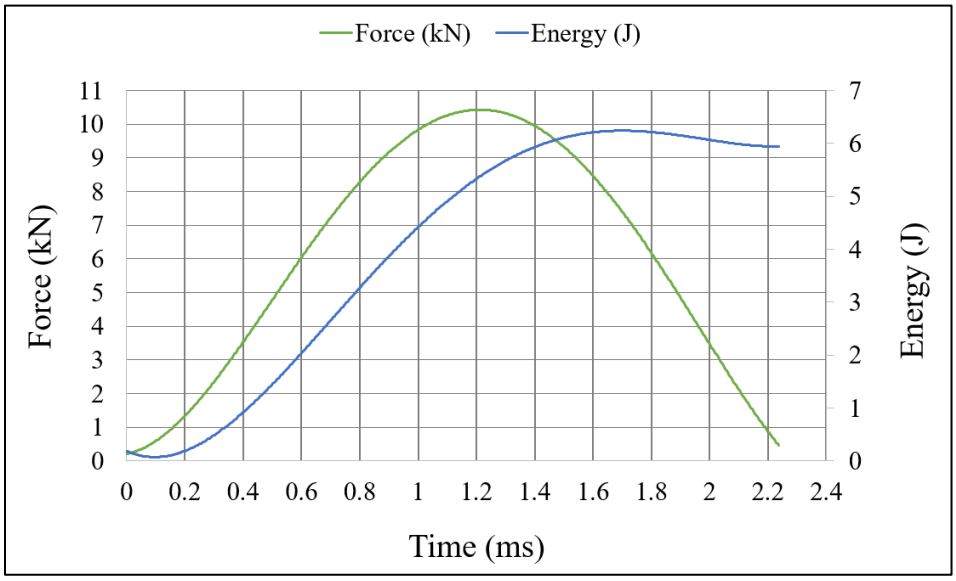

Figure 15. The load and energy of the impacted modified honeycomb core

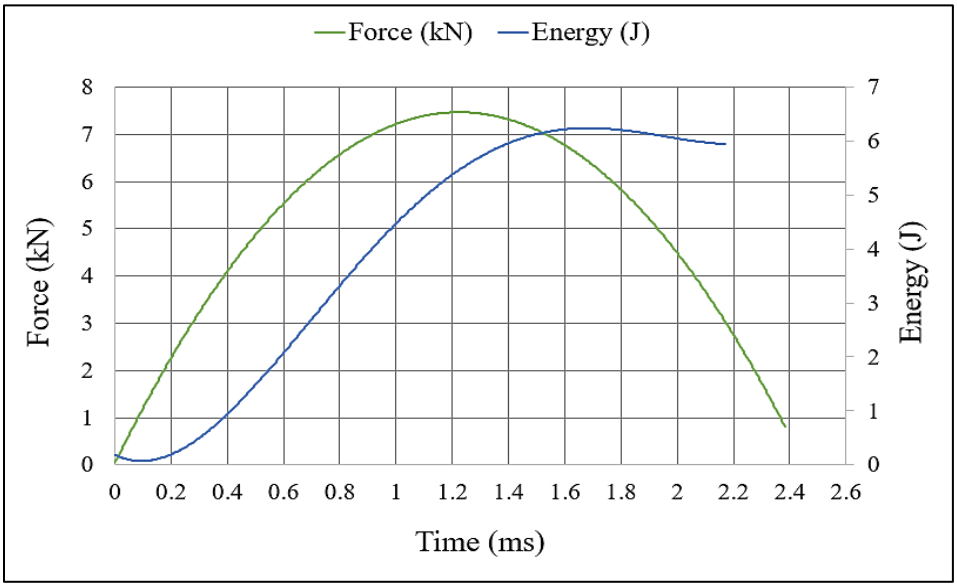

Figure 16. The load and energy of the impacted modified honeycomb core

Figure 17 shows a comparison between the experimental results and numerical results. The results obtained from the finite element model showed a good agreement with

the experimental results. The modified core showed superior performance in comparison with the regular core.

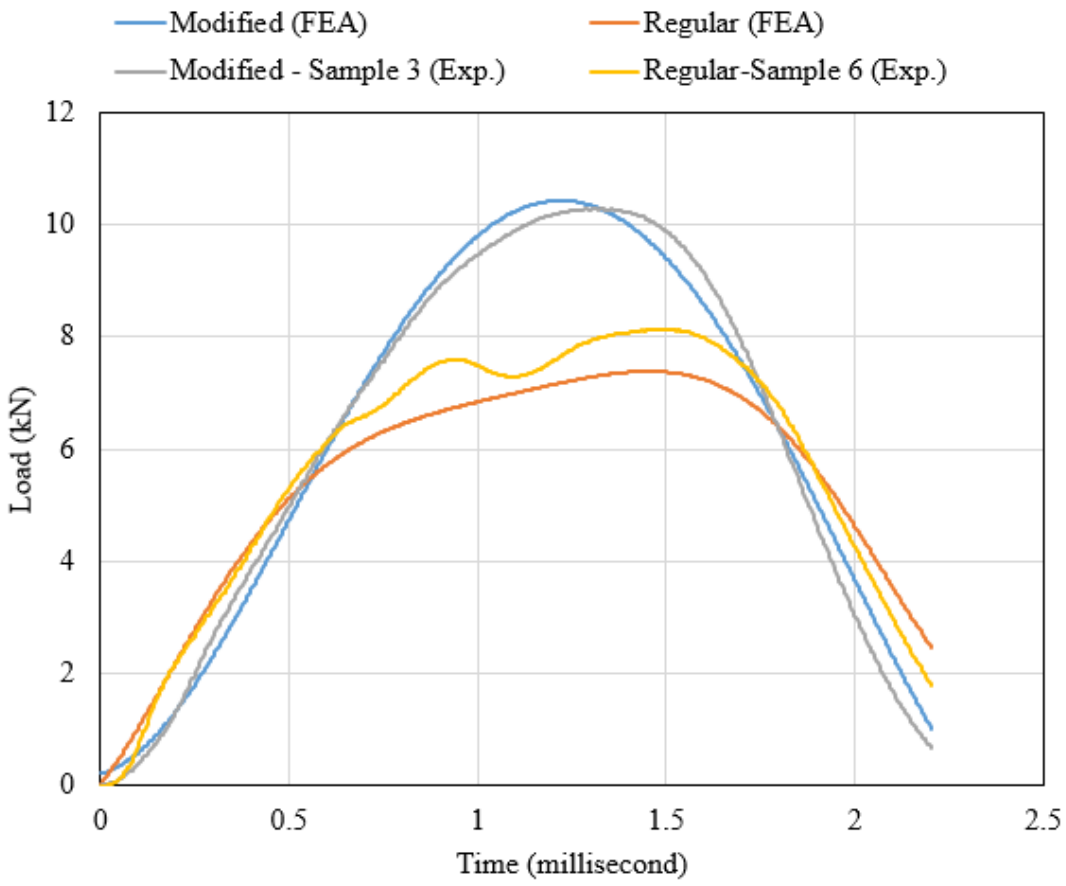

Figure 17. The maximum load obtained from the finite element model vs. experiments for both configurations

The impactor traveled a larger distance while impacting the regular samples compared with distance traveled while impacting the modified samples. Figure 18 and Figure 19 show the impacted zone for regular and modified honeycomb core, respectively.

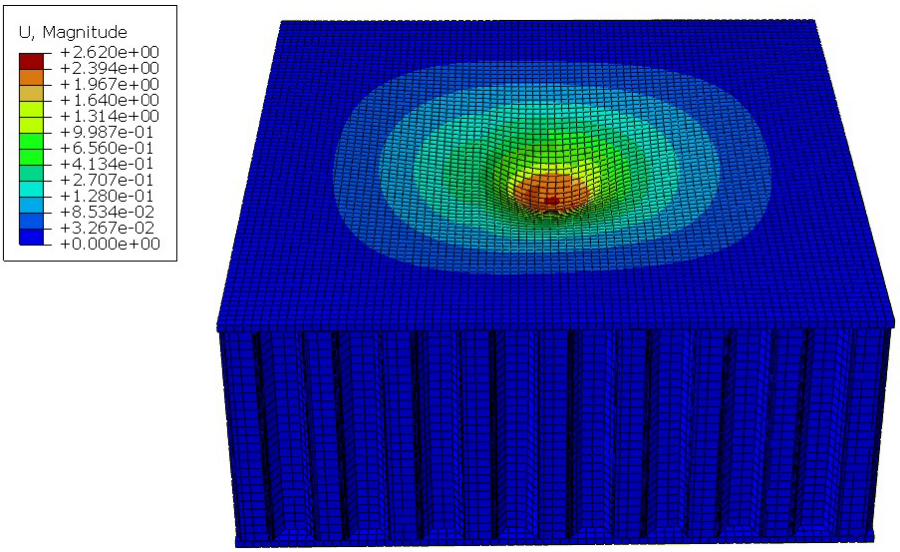

Figure 18. The magnitude of the displacement in the Z-direction for the regular core

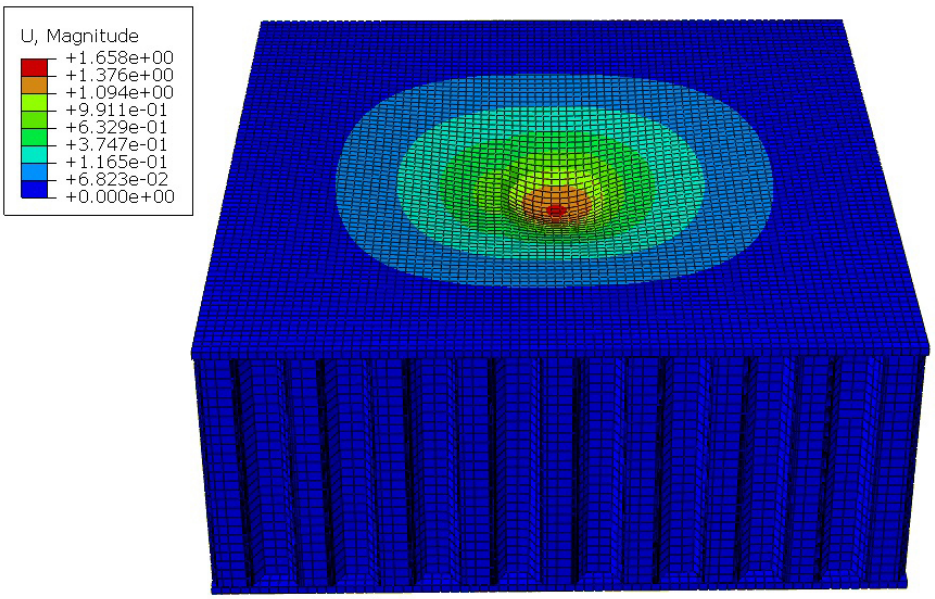

Figure 19. The magnitude of the displacement in the Z-direction for the modified core

6. CONCLUSION

Two honeycomb cores, regular and modified, configurations were designed and additively manufactured using 304L stainless steel. The modified honeycomb core had a 238% larger contact area when compared to the regular honeycomb core. Sandwich composite panels were manufactured using these two cores and a carbon prepeg facesheet. These sandwich panels were evaluated for their bond strength and impact resistance using the flatwise tension test and impact test respectively. The configuration with a larger contact area showed a better performance compared with the regular honeycomb core. Results showed that the flatwise tensile strength increased greatly due to the additional bonding area. A finite element model was developed to study the damage due to impact. The model was validated using the results obtained from the experiments. The modified honeycomb core showed an impact resistance with a 41.3% higher than the regular core. In addition, the increased contact area acted as an additional supporter to the sandwich structure and prevented the impactor nose from further penetrating the core. Therefore, from this study it can be concluded that increasing the surface bonding area in sandwich composites will lead to higher impact resistance and stronger bonding between the core and the facesheet.

REFERENCES

[1] X. Li, L. G. Tabil, and S. Panigrahi, "Chemical treatments of natural fiber for use in natural fiber-reinforced composites: a review," *Journal of Polymers and the Environment,* vol. 15, no. 1, pp. 25-33, 2007.

[2] H. Akil, M. Omar, A. Mazuki, S. Safiee, Z. M. Ishak, and A. A. Bakar, "Kenaf fiber reinforced composites: A review," *Materials & Design,* vol. 32, no. 8-9, pp. 4107-4121, 2011.

[3] T. Anderson and E. Madenci, "Experimental investigation of low-velocity impact characteristics of sandwich composites," *Composite structures,* vol. 50, no. 3, pp. 239-247, 2000.

[4] H. Hu, S. Belouettar, and M. Potier-Ferry, "Review and assessment of various theories for modeling sandwich composites," *Composite Structures,* vol. 84, no. 3, pp. 282-292, 2008.

[5] P. M. Schubel, J.-J. Luo, and I. M. Daniel, "Impact and post impact behavior of composite sandwich panels," *Composites Part A: applied science and manufacturing,* vol. 38, no. 3, pp. 1051-1057, 2007.

[6] D. Horrigan, R. Aitken, and G. Moltschaniwskyj, "Modelling of crushing due to impact in honeycomb sandwiches," *Journal of Sandwich Structures & Materials,* vol. 2, no. 2, pp. 131-151, 2000.

[7] J. K. Paik, A. K. Thayamballi, and G. S. Kim, "The strength characteristics of aluminum honeycomb sandwich panels," *Thin-walled structures,* vol. 35, no. 3, pp. 205-231, 1999.

[8] A. Mouritz, "Compression properties of z-pinned sandwich composites," *Journal of materials science,* vol. 41, no. 17, pp. 5771-5774, 2006.

[9] S. Abrate, "Modeling of impacts on composite structures," *Composite structures,* vol. 51, no. 2, pp. 129-138, 2001.

[10] J. Leijten, H. E. Bersee, O. K. Bergsma, and A. Beukers, "Experimental study of the low-velocity impact behaviour of primary sandwich structures in aircraft," *Composites Part A: Applied Science and Manufacturing,* vol. 40, no. 2, pp. 164-175, 2009.

[11] D. Zenkert, A. Shipsha, P. Bull, and B. Hayman, "Damage tolerance assessment of composite sandwich panels with localised damage," *Composites Science and Technology,* vol. 65, no. 15-16, pp. 2597-2611, 2005.

[12] P. H. Bull and F. Edgren, "Compressive strength after impact of CFRP-foam core sandwich panels in marine applications," *Composites Part B: Engineering,* vol. 35, no. 6-8, pp. 535-541, 2004.

[13] S. Anandan, G. Dhaliwal, Z. Huo, K. Chandrashekhara, N. Apetre, and N. Iyyer, "Curing of thick thermoset composite laminates: multiphysics modeling and experiments," *Applied Composite Materials,* vol. 25, no. 5, pp. 1155-1168, 2018.

[14] H. Koerber and P. P. Camanho, "Simulation of progressive damage in bolted composite joints," presented at the 13th European conference on composite materials, Stockholm, Sweden, 2008.

[15] A. Demir, H. Ozturk, K. Edip, M. Stojmanovska, and A. Bogdanovic, "Effect of Viscosity Paramter on The Numerical Simulation of Reinforced Concrete Deep Beam Behavior," *The Online Journal of Science and Technology,* vol. 8, no. 3, pp. 50-56, 2018.

[16] A. Demir, H. Ozturk, and G. Dok, "3D numerical modeling of RC deep beam behavior by nonlinear finite element analysis," *Disaster Science and Engineering,* vol. 2, no. 1, pp. 13-18, 2016.

[17] O. Fashanu *et al.*, "Effect of SLM Build Parameters on the Compressive Properties of 304L Stainless Steel," *Journal of Manufacturing and Materials Processing,* vol. 3, no. 2, p. 43, 2019.

[18] A. ASTM, "D7766/D7766M-11 standard practice for damage resistance testing of sandwich constructions," in *American Society for Testing and Materials*, 2011.

[19] A. C297, "Standard test method for flat-wise tensile strength of sandwich constructions," 2004: American Society for Testing and Materials West Conshohocken, PA.

SECTION

3. CONCLUSION

The first paper involved the investigation of the structural integrity of CFRP water turbine blades with different laminate stacking sequences. A finite element model was developed to determine the location of the failure initiation. A modified blade element momentum theory was used to determine the hydrodynamic forces along the span of the blade while operating under optimum characteristics. The blades were tested till failure, and then results were compared with the FEM for validation. The effect of the bending load and the hydrodynamic load on the water turbine blades with unidirectional laminates and cross-ply laminates were investigated. The unidirectional blades showed a higher resistance towards both loads. However, as angles were induced while applying the load, the unidirectional blades showed a deterioration in the performance while the cross-ply blades had a steady performance. Both laminate stacking sequences showed the failure initiation near the root of the blade. This study concluded that the hydrodynamic loads are not strong enough to initiate any failure on the blades. However, it is important to note that the periodic application of the small load/traction may induce failure due to fatigue, which was beyond the scope of the current work. The maximum stress due to the hydrodynamic forces was around 0.060 GPa, which was located at the root of the blade.

The second paper involved an investigation of the delamination growth based on the laminate stacking sequence of CFRP water turbine blades. Samples were manufactured from IM7/Cycom 5320-1 prepreg system using OOA process. Three different layup orientations were tested ([0º/90º/90º/0º], [0º/0º/0º/0º], and [+45º/-45º/-45º/+45º]). An

interlaminar separation was created between the plies in two different locations (middle and bottom) and from both sides (back and front) of the blade. Thermography analysis approach was utilized to visualize the internal separation growth. Thermal images were taken of the interlaminar debonding locations before the blades start the operation in the water tunnel and after every 1 million revolutions. The experiment was stopped after 3 million revolutions because the behavior of the delamination of all blades had a very small fluctuation. A one-way fluid-structure interaction model was developed to visualize the stresses along the blade. The unidirectional blade showed the highest resistance to delamination. Whereas, the cross-ply laminate blades showed the highest delamination growth.

In the third paper, the effect of increasing the contact area between a facesheet and a core in a sandwich structure was studied. The core was additively manufactured using 304L stainless steel powder. Two honeycomb core configurations were manufactured. First, a regular honeycomb core with no modifications in the top and bottom faces. The second configuration has been modified to have 238% more surface area on both faces. The weight of both configurations was maintained equally by reducing the wall thickness of the modified core. The facesheets were manufactured using IM7/Cycom 5320-1 prepreg system, and they were bonded to the cores using a commercial adhesive system. A finite element analysis (FEA) model was developed to investigate the resistance of the localized damage due to the impact of both configurations. Experiments were carried out to validate the FEA model. The modified honeycomb core showed a 41.3% higher resistance to the impact damage. A flatwise tensile strength test was conducted to evaluate the increase of the contact area on the strength of the bond between the core and the facesheet. The

modified sandwich structures showed an improvement in the bonding strength compared to the regular core. The maximum tensile strength of the modified samples was 15.35 kN, while the maximum tensile strength of the regular honeycomb core was 11.25 kN. The finite element model showed a good agreement with the experiments. This study concluded that increasing the contact area between the facesheet and the core can lead to an increase in the damage resistance due to impact and a higher tensile strength.

BIBLIOGRAPHY

[1] I. M. Daniel, O. Ishai, I. M. Daniel, and I. Daniel, *Engineering mechanics of composite materials*. Oxford university press New York, 1994.

[2] M. Mrazova, "Advanced composite materials of the future in aerospace industry," *Incas bulletin,* vol. 5, no. 3, p. 139, 2013.

[3] P. Jerome, "Composite materials in the airbus A380-from history to future," in *Beijing: Proceedings 13th International Conference on Composite Materials (ICCM-13)*, 2001.

[4] A. Bahaj and L. Myers, "Fundamentals applicable to the utilisation of marine current turbines for energy production," *Renewable Energy,* vol. 28, no. 14, pp. 2205-2211, 2003.

VITA

Mokhtar Fal was born in Medina, Saudi Arabia. In January 2004, he joined Yanbu Industrial College (YIC). In February 2009, he received the prize of the best senior project at YIC, Yanbu, Saudi Arabia, based on his electrochemical machining (ECM) design project. He received his B.S. degree with Honors in Mechanical Engineering in March 2009 from YIC, Yanbu, Saudi Arabia. During his five years in YIC, he received nine honor certificates. In January 2009, he was awarded the best mechanical engineering student of the year.

In April 2009, he joined Shebh Aljazira Company and worked as a project manager and was responsible for the construction of the main water and sewage stations in Medina, Saudi Arabia. In January 2010, Mokhtar joined the King Abdulaziz City for Science and Technology (KACST), Riyadh, Saudi Arabia. He worked as an academic researcher. During his first year in KACST, he helped developing computational fluid dynamic (CFD) models for multiple unmanned aerial vehicles (UAVs).

Mokhtar joined Missouri University of Science and Technology, Rolla, Missouri, USA, in July 2012. He received his Master's Degree in mechanical engineering in May 2015. Since August 2015, Mokhtar Fal has been enrolled in the Ph.D. program at Missouri University of Science and Technology. In May 2020, he received his Ph.D. degree in mechanical engineering from Missouri University of Science and Technology.